Aus der Klinik für Neurologie mit experimenteller Neurologie
der Medizinischen Fakultät Charité – Universitätsmedizin Berlin

DISSERTATION

Adaptations- und Rekonstruktionsmechanismen im hypoperfundierten Gehirn

Mechanisms of adaptation and reconstruction in the hypoperfused brain

zur Erlangung des akademischen Grades
Doctor of Philosophy (PhD)

vorgelegt der Medizinischen Fakultät
Charité – Universitätsmedizin Berlin

von

Melanie Tamara Carolin Kuffner

aus Erding

Datum der Promotion: 30.11.2023

Table of contents

List of figures

List of abbreviations

ANOVA	analysis of variance
BBB	blood-brain barrier
CCAo	occlusion of common carotid artery
DALY	Disability-adjusted life year
DAPI	4′,6-diamidino-2-phenylindole
EGFP	enhanced green fluorescent protein
ELISA	enzyme-linked immunosorbent assay
FLEX	flip-excision
GABA	γ-aminobutyric acid
GFAP	glial fibrillary acidic protein
GAPDH	glyceraldehyde 3-phosphate dehydrogenase
IGFBP3	insulin-like growth factor-binding protein 3
IFNγ	interferon gamma
IL	interleukin
LCM	laser capture microdissection
LTP	long-term potentiation
MAPK/ERK	mitogen-activated protein kinase
MCAo	occlusion of the middle cerebral artery
mRNA	messenger ribonucleic acid
PFA	paraformaldehyde
PMA	phorbol 12-myristate 13-acetate
PBS	phosphate-buffered saline
RT-qPCR	reverse transcription polymerase chain reaction
SorCS2	sortilin-related Vps10p domain containing receptor 2
SIRS	systemic inflammatory response syndrome
TGF-β1	transforming growth factor beta 1
VECdh	vascular endothelial cadherin
VEGF	vascular endothelial growth factor

Abstract

Ischemic damage to the brain poses a long-term disability or even death. Endogenous recovery cannot fully restore functionality by itself, leading to deficits in cognition and motor function. This thesis investigates microenvironmental changes mediated by the molecules interleukin 6 (IL-6) and SorCS2 in murine models of ischemia.

Our first study focuses on the effect of the inflammatory cytokine IL-6 in carotid stenosis, evaluating changes in the brain parenchyma and other associated factors. IL-6 plays an ambivalent role in the hypoperfused brain: it is associated with poor outcome such as deterioration in motor function, but it is also essential for recovery processes. In this study, mice underwent unilateral carotid artery occlusion, and IL-6 overexpression in astrocytes was induced on day 2 after surgery. Motor skills and health status were monitored for 21 days using behavioral tests, and changes in cerebral connectivity and brain remodeling were examined using diffusion tensor imaging. Data analysis showed that IL-6 overexpression has no adverse effect on the overall condition and fosters connectivity changes in the brain. In total, 10 out of 14 tracts were increased, mainly in interhemispheric networks. Proteome analysis of the ipsilesional striatal fiber tracts and the contralesional motor cortex showed alterations in expression levels of plasticity-associated proteins. Caprin-1 was more abundantly expressed on the ipsilesional side, and the GABA-transporter Gat1 was downregulated on the contralesional side, reducing inhibitory GABA signaling. Both are targets for further studies and potential drug targets for translatory research.

The second part of the thesis investigates the effects of a SorCS2 knockout in stroke models. This Vps10p sorting receptor is a regulator of vesicular trafficking and secretion, possibly involved in endogenous IL-6 regulation. The study showed that contrary to prior knowledge, not only neurons but also astrocytes express SorCS2 after stroke, and TGF-β likely mediates induction. IL-6 was not confirmed to be regulated in *in vivo* assays. Ablation of SorCS2 correlated with endostatin expression, mediating effects on regenerative processes such as angiogenesis.

Our third study focuses on improving animal research. Data from standardized behavioral tests were collected in one curated database. This allows meta-analysis of data and can reduce animal suffering and the number of experimental animals due to higher experimental standards and prediction of human endpoints. It also generated a new starting point for innovative research concepts based on existing animal data.

In summary, the thesis contributes insights into post-ischemic recovery processes and found several potential targets for further research on therapeutic interventions for brain ischemia. It also contributes to the 3R approach of reducing animal suffering in experimental research.

Zusammenfassung

Eine ischämische Schädigung des Gehirns kann zu einer langfristigen Behinderung bis hin zum Tod führen. Die körpereigene Regeneration kann verlorene Funktionalität nicht vollständig wiederherstellen, was zu kognitiven und motorischen Defiziten führt. Diese Arbeit erforscht die durch die Moleküle IL-6 und SorCS2 in Ischämiemodellen bei Mäusen vermittelten, lokalen Veränderungen des Mikromileus.

Die erste Studie untersucht die Wirkung des inflammatorischen Zytokins Interleukin 6 (IL-6) bei einer Karotisstenose auf Veränderungen des Hirnparenchyms. IL-6 spielt im hypoperfundierten Gehirn eine ambivalente Rolle, da es einerseits mit einem schlechteren Verlauf korreliert, andererseits aber auch für den Erholungsprozess wichtig ist. In dieser Studie wurde bei Mäusen ein einseitiger Verschluss der Arteria carotis communis vorgenommen und zwei Tage später eine Überexpression von IL-6 in Astrozyten induziert. Die motorischen Fähigkeiten und der Gesundheitszustand wurden 21 Tage lang mittels Verhaltensversuchen beobachtet und Veränderungen in der zerebralen Konnektivität sowie der Umbau des Gehirns untersucht. Die Überexpression von IL-6 hatte keine nachteiligen Auswirkungen auf den Gesundheitszustand und begünstigte eine Zunahme der Konnektivität im Gehirn bei 10 von 14 veränderten Verbindungen, vor allem zwischen den Hemisphären. Die Proteomanalyse der ipsilesionalen striatalen Faserbahnen und des kontraläsionalen motorischen Kortex zeigte Veränderungen in den Expressionsniveaus von Plastizitäts-assoziierten Proteinen wie Caprin-1 und dem GABA-Transporter Gat1. Beide Moleküle sind Kandidaten für weitere Untersuchungen und potenzielle Zielstrukturen für translationale Forschung.

Im zweiten Teil der Arbeit wird die Auswirkungen eines SorCS2-Knockouts in Schlaganfallmodellen untersucht. Die Hypothese war, dass SorCS2 an der endogenen IL-6-Regulation beteiligt ist. Die Studie zeigte, dass im Gegensatz zu bisherigen Erkenntnissen nach einem Schlaganfall nicht nur Neuronen, sondern auch Astrozyten TGF-β-vermittelt SorCS2 exprimieren. Es wurde nicht bestätigt, dass IL-6 durch SorCS2 reguliert wird. Ein SorCS2-Knockout korrelierte hingegen mit der Endostatin-Expression. Diese hat Auswirkungen auf regenerative Prozesse wie Angiogenese.

Drittens konnte durch Agglomeration von Verhaltensdaten eine kuratierte Datenbank erstellt werden, um eine Meta-Analyse der Daten zu ermöglichen. Somit kann die Zahl der

Versuchstiere aufgrund höherer experimenteller Standards und das Tierleid durch Vorhersage humaner Endpunkte reduziert werden.

Zusammenfassend gewährt diese Arbeit Einblicke in postischämische Erholungsprozesse und zeigt potenzielle Zielstrukturen für die weitere Erforschung therapeutischer Interventionen bei Ischämien auf, während sie gleichzeitig einen Beitrag zum 3R-Ansatz zur Verringerung des Tierleidens in der experimentellen Forschung leistet.

1. Introduction

1.1 Current state of research

1.1.1 Burden of disease

The industrialized world is characterized by increasingly aging societies and the rise of age-related diseases, most prominently dementia, heart attacks, and stroke. Cardiovascular diseases attribute to over a third of all deaths in Germany, and cerebrovascular diseases alone are the fifth leading cause of death in the United States.[1,2] Considering the combined cause of death and disability, stroke ranks third globally.[3] Carotid artery occlusion is highly linked to stroke and is attributable to patients' cognitive impairment.[4,5] The burden of disease is tremendous, and additionally to implementing preventive measures, new therapy options and medication are needed to improve patients' lives and unburden health care systems.

In stroke, therapy focuses on revascularization – only applicable for a small subset of patients – and physical rehabilitation therapy.[6] Major impairments, especially of general motor function, still affect stroke patients massively in their everyday lives with a high count of disability-adjusted life years (DALYs).[7,8] Carotid stenosis treatment usually consists of carotid endarterectomy, stenting, or medical therapy focusing on halting disease progression and preventing stroke. Despite the high prevalence of ischemic events, there are no or very few efficient pharmacological treatment options that concentrate on the recovery from ischemic stroke and the consequences of chronic hypoperfusion due to stenosis. This is attributable to the only partly understood and very complex interplay of processes in the ischemic brain.

1.1.2 Pathophysiology in ischemic settings

Stroke and carotid artery occlusion both lead to pathophysiological mechanisms and brain damage, such as white matter lesions and, in stroke, brain atrophy. Long-term or severe short-term hypoperfusion of the brain leads to a lack of oxygen and glucose, especially in the watershed regions of the brain. In stroke, this leads to a profound change in the cerebral microenvironment by activating the so-called ischemic cascade, a complex process involving excitotoxicity, oxidative stress, blood-brain barrier (BBB) dysfunction, activation of the immune system, and cell death.[9] In carotid artery occlusion and accompanying chronic cerebral hypoperfusion, the stress on the brain cells is less pronounced,

leading to slower pathophysiology. The main hallmarks found in hypoperfusion models are white matter damage, blood-brain barrier disruption, and mild astrogliosis, ultimately speculated to lead to vascular dementia.[10–13]

Ameliorating brain recovery is an attractive target for the treatment of ischemic diseases. The brain can re-establish parts of functionality lost due to insufficient perfusion. Intact areas of the brain can compensate missing function. This is called plasticity. New neuronal connections form between previously unconnected regions and enable the re-establishment of function.[14] The underlying mechanisms are only partially known. Among the contributors fostering plasticity, besides neurogenesis, are angiogenesis, extracellular matrix remodeling, and inflammatory cues.[15–18] There has been a strong focus on investigating brain composition changes after and during ischemia to better understand beneficial and detrimental processes. The critical processes for recovery, angiogenesis and inflammation, are both ambivalent and can influence one another via signaling molecules such as vascular endothelial growth factor (VEGF) for angiogenesis and cytokines such as interleukin (IL)-1β and IL-6.[15,19–22]

1.1.3 IL-6 in the ischemic brain

Inflammation after stroke and ischemia is a complex process initiated by several inflammatory cues and can lead to beneficial and detrimental effects. The glial response to inflammatory cytokines – especially astrogliosis – is necessary in stroke response but can worsen the cognitive function when present excessively.[23,24] Astrogliosis is initiated by circulating cytokines, mainly of the IL-6 family. They activate astrocytes that, in response, express the marker glial fibrillary acidic protein (GFAP) and form the glial scar demarcating the lesioned area.[25–27]

Considering the crucial role of inflammation in ischemic diseases, this thesis primarily focuses on the inflammatory cytokine IL-6. In a non-ischemic setting, IL-6 levels in the bloodstream correlate to sickness severity in mice and humans.[28,29] Constitutive expression of astrocytic IL-6 in non-ischemic mice causes microglial activation and motor deficits.[30] Systemic overexpression of IL-6 in the entire bloodstream is possible with the mouse model presented in this thesis when cross-bred with animals carrying the recombinase Cre-ERT2 under control of the endothelial promoter VECdh (Vascular endothelial cadherin). After induction of systemic IL-6, mice rapidly developed symptoms that resemble a cytokine storm and systemic inflammatory response syndrome (SIRS) in humans.

These mice showed sickness behavior, leukocytosis, reduced body temperature, splenomegaly, and died.

Local and chronically increased cerebral IL-6 lead to motor deficits in non-ischemic mice.[31] Conversely, IL-6 in the brain has been associated with neuroplasticity.[32,33] In stroke patients, high systemic and cerebrospinal fluid IL-6 levels correlate with poor outcome and higher sickness scores.[34,35] Similarly, in carotid artery stenosis, high serum IL-6 are linked to unfavorable outcome and a higher likelihood of plaque rupture.[36,37] Complete removal of IL-6 in the ischemic mouse brain led to a decrease in angiogenesis, and an overall worsened outcome.[38] These conflicting data hint at an ambivalent role of IL-6 in the ischemic brain. Recovery and plasticity mechanisms possibly depend on exclusively local, paracrine-acting, and moderate levels of IL-6 in the brain, while systemic, high levels might be detrimental to recovery.

1.1.4 SorCS2 and astrocytes

In addition to understanding the effects of IL-6 in ischemic recovery, this thesis addresses the endogenous regulation of signaling molecules after stroke by a specific sorting receptor. Sortilin-related Vps10p domain containing receptor 2 (SorCS2) is a protein found primarily in neurons in the brain and is part of the Vps10p domain receptors gene family.[39] These receptors play a role in neurotrophin sorting and shuttling, integral for mediating neuronal survival.[40,41] SorCS2 is relevant in psychiatric diseases and was shown to be critical in memory formation and synaptic plasticity.[42,43] Its protective role in oxidative stress models for epilepsy also made it an exciting target for studies in ischemic stroke settings. Similar effects might be observed that favor beneficial outcome.[44] There is limited research on which proteins are interacting and regulated by SorCS2 and are therefore responsible for these beneficial effects. IL-6 is a potential target protein regulated by SorCS2, as others have shown that another member of Vps10p receptors, SorLA, binds IL-6 and mediates its cellular uptake.[45]

1.2 Objective

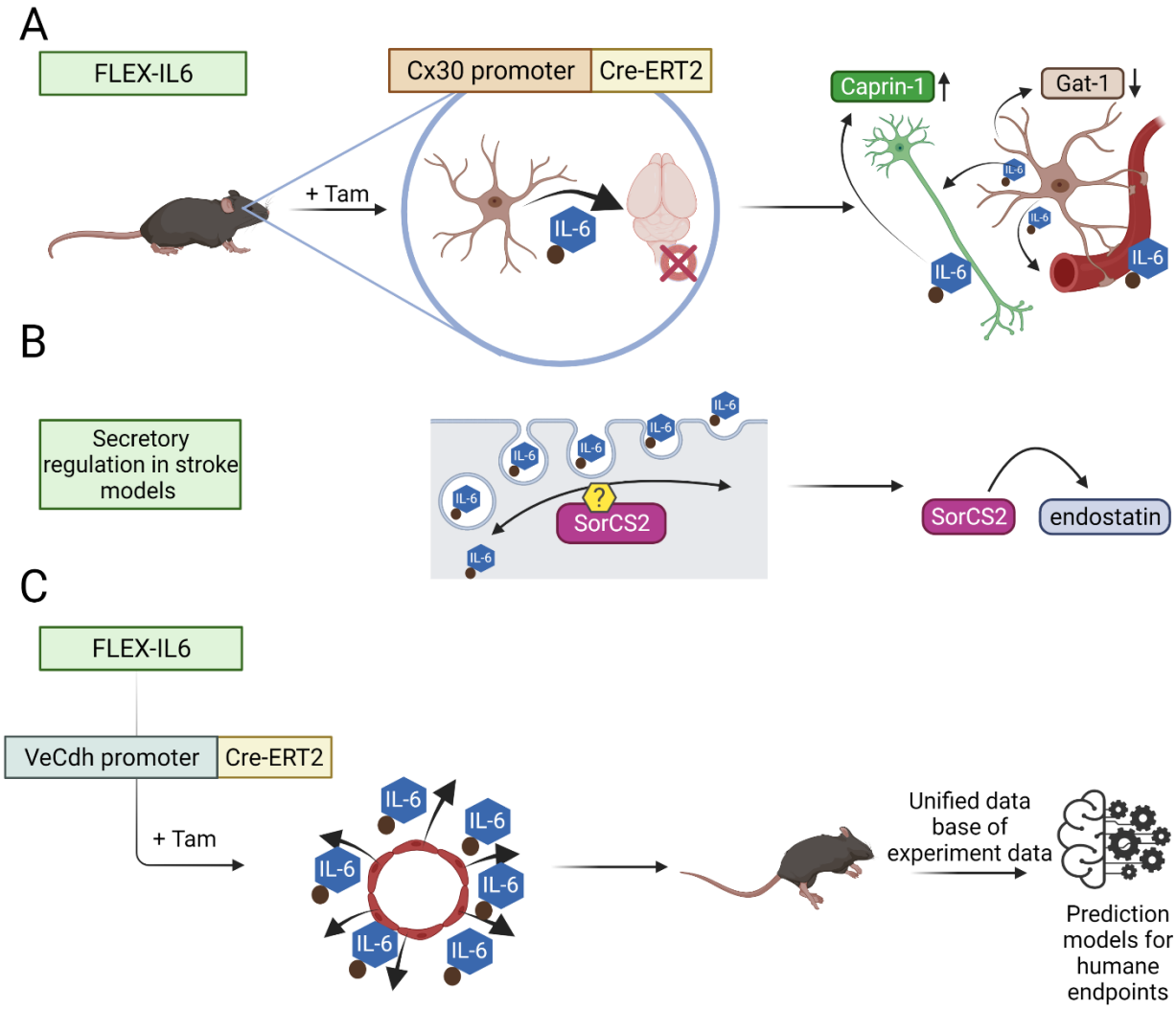

Figure 1 Visual summary of the thesis. (own representation) **A.** Cx30-Cre-ERT2 FLEX-IL6 mouse model with inducible IL-6 expression by tamoxifen administration was used to study the effects of IL-6 in unilateral carotid artery occlusion. Caprin-1 upregulation and Gat1 downregulation were observed in the microenvironmental proteome analysis and can be potential targets for further studies. Additionally, MRI studies showed enhanced connectivity in IL-6 overexpressing animals. **B.** The effects of SorCS2 ablation in astrocytes are a potential endogenous regulation mechanism of IL-6. The study showed that mainly endostatin is regulated and at least partially responsible for the recovery effects of SorCS2 after stroke. **C.** Mice of the VeCdh-Cre-ERT2 FLEX-IL6 line inducibly express IL-6 in all endothelial cells. The resulting high IL-6 levels lead to severe deterioration and death. The study endpoint for sick mice was challenging to determine, as classical endpoints were not well suited for this scenario. We aimed to find humane endpoints by a data-driven approach to prevent unnecessary animal suffering. We gathered animal data into one large database to re-use data and reduce the number of animals. A novel machine learning based meta-analysis algorithm trained on that data can predict humane endpoints for early termination of the behavioral experiment and reduces animal suffering.

The primary goals of this study were to investigate beneficial and detrimental factors in the recovery process of stroke and carotid artery occlusion and shed light on crucial recovery mechanisms and active molecules in an exploratory approach. Special attention was given to the use of standardized behavioral protocols and the conceptualization of a

unified database for animal data to foster reproducibility of research and open the possibility to re-use data for advanced animal meta-studies.

To this end, the following approaches were taken.
Firstly, the study focused on IL-6 mediated effects on the brain parenchyma in the short-term outcome after carotid artery occlusion. A new mouse model with inducible brain exclusive IL-6 secretion was established and validated. Behavioral, molecular, and connectivity alterations were studied to understand molecular mechanisms and investigate potential new treatment targets for carotid artery occlusion.
Secondly, the role of SorCS2, a sorting receptor, in stroke recovery was studied. We examined expression patterns and means of induction, and functional implications of endogenous SorCS2 upregulation.
Lastly, data-gathering and storage were unified for behavioral studies in ischemic mouse models. Tests, time points, and parameter collection were standardized, and existing data were processed into one single database to allow the re-use of animal data. On this data set, algorithms were trained using machine learning to predict humane endpoints in behavioral mouse stroke studies. This contributes to the efforts of Charité's 3R to improve animal research.

2. Methods

All methods used in this study are described in the publications in detail. This section gives a summary of study designs and critical methods. Details on materials and methods can be found in the respective section of the individual publications (see Kuffner et al.[46], Malik et al.[44] and Mei et al. [47]).

2.1 Animals and mouse models

Local authorities (Landesamt für Gesundheit und Soziales, (LaGeSo), Berlin (Reg G0119/16, G0157/17)) approved all experimental animal procedures that were conducted in line with German animal protection law and animal welfare guidelines. Mice were kept in groups on a 12 h light/dark cycle and allowed *ad libitum* access to water and food. Animals in behavioral studies had limited food access for 3 h per day with an additional 1.1 g chow overnight to prevent excessive weight loss.

A custom strain of mice was generated for the experiments in publication 1, Cx30-Cre-ERT2; FLEX-IL6 (*Figure 1*). A DNA sequence consisting of murine IL-6, linked by a spacer to a myc-tag, followed by a T2A self-cleavage site, and the fluorescent protein mKate2 was designed. This sequence was embedded in a flip-excision (FLEX) cassette integrated into the R26 locus of mice. The FLEX-IL6 mice were then crossbred with mice carrying an astrocyte-specific Cre-ERT2 recombinase (Cx30-Cre-ERT2). All mice were bred on a C57BL/6J background and used after backcrossing for more than 10 generations. Hemizygous Cx30-Cre-ERT2; FLEX-IL6 mice, or FLEX-IL6 mice at the age of 10 – 12 weeks at the time of surgery were used for the experiments.

In study 2, the mouse line with SorCS2 deletion has been previously described by Glerup et al.[42] and male animals at the age of 8 – 14 weeks at the time of temporary occlusion of the middle cerebral artery (MCAo) have been used for the experiments.

2.2 In vivo design

In publication 1, mice were set on a food-restricted diet with limited food access for 3 h per day four weeks before surgery. Three weeks before surgery, mice started pre-training for the staircase skilled pellet reaching test. Unilateral occlusion of common carotid artery (CCA) was performed by permanently ligating the left CCA (CCAo). One day after surgery, mice were scanned using T2-weighted MRI for visible signs of a stroke or immediate

lesions and, in this case, excluded following the preset exclusion criteria. On day two after surgery, animals received i.p. injections of 1 mg tamoxifen (Sigma, 10 mg/ml in 1:10 ethanol/corn oil (all purchased from Sigma)) for one to three consecutive days. Behavioral testing continued two days after surgery. Sickness was evaluated using a modified deSimoni's Neuroscore on days 2, 7, 14, and 21 after surgery. Rotarod testing was done on days 2, 7, and 14 after CCAo in three runs per trial. Staircase pellet reaching was continued daily until 21 days after surgery. On day 21, diffusion tensor imaging (DTI) and T2-weighted MRI were performed. All mice were perfused transcardially on day 21.
In publication 2, animals were subjected to a 45-minute MCAo) as described and observed for short-term (1 and 3 days) or long-term (21 days) studies.[48]

2.3 Western blotting and ELISA

In study 1, serum IL-6 was analyzed using enzyme-linked immunosorbent assay (ELISA) (Mouse IL-6 Quantikine, R&D Systems). Samples were taken from blood sampled on day 5 after surgery and day 3 after induction with tamoxifen.
Brain IL-6 was determined semi-quantitatively by western blotting of homogenized brain tissue. Briefly, deep-frozen brain tissue was homogenized in a rotor-stator homogenizer, centrifuged, and the supernatant treated with detergents to break the cell structure. Samples were treated with ultrasound, and protein content was quantified using Pierce Reagent (Thermo Fisher). The samples were then denatured in reducing sample buffer and separated on 4-12 % SDS-polyacrylamide gels (15-wells, Life Technologies) and subsequently blotted onto a nitrocellulose membrane. After formaldehyde-fixation and washing, proteins were detected using the ReadyTector® system (CANDOR Bioscience; Anti-Mouse-HRP and Anti-Rabbit-HRP) and anti-IL-6 (1:1000, ab6672, Abcam) and anti-GAPDH (1:1000, MAB374, Merck/Millipore) antibodies. Bands were imaged using WesternBright ECL HRP substrate (Advansta) and imager (Vilber Lourmat).
In study 2, brain homogenates were analyzed using the following assays: TGF-β1 (Abcam, ab119557), GFAP (Millipore, NS830), endostatin (Boster, EK1376), U-Plex Biomarker Group 1 assay (Meso Scale Diagnostics, K15083K).
For western blotting, tissue and cell homogenates were studied using the following antibodies: anti-SorCS2 (R&D Systems, AF4237, 1:1,000), anti-p-ERK (Cell Signaling, 4370, 1:2,000), anti-actin (Abcam, ab8227, 1:2,000), anti-GFAP (Millipore, MAB360, 1:1,000). Imaging was performed with the digital LI-COR imaging system.

2.4 Cell culture and transfection

HEK293T cells (Biocat GmbH) were cultured in Dulbecco's Modified Eagle's Medium (DMEM; Gibco) supplemented with 10 % fetal calf serum, 1 % penicillin/streptomycin (Merck), 1 % sodium pyruvate (Gibco), 1 % MEM non-essential amino acids (Gibco) and 1 % GlutaMAX (Gibco). Brain microvascular endothelial cells (bEnd.3, ATCC CRL-2299) were cultured in DMEM (ATCC) supplemented with 1 % L-glutamine (Gibco) and 1 % penicillin/streptomycin (Merck).
For IL-6 production, HEK cells were transfected with plasmids that encode the FLEX-IL6 construct and Cre-EGFP or exclusively the Cre-EGFP plasmid as control using Xtreme-Gene (Roche). After 24 h, the supernatant was harvested and spun down to clear away cellular debris. Murine bEnd.3 cells were incubated with this supernatant from HEK cells transfected with both plasmids or only the control plasmid for 1 h.

2.5 RT-qPCR

Quantitative reverse transcription polymerase chain reaction (RT-qPCR) was performed on bEnd.3 cells after mRNA extraction using random primers and oligo-dT primers (Eurofins) for reverse transcription. Quantitative PCR reaction was done with exon-spanning primers for tyrosine 3-monooxygenase/tryptophan 5-monooxygenase activation protein (Ywhaz) and intron-spanning primers for Il6 using SYBR Green (Qiagen) (Il6 primer sequences: forward GGAAATTGGGGTAGGAAGGAC, reverse ACTTCACAAGTCGGAGGCTT) in study 1 and human samples in study 2. Alterations in mRNA expression levels were calculated using the ddCT method. SorCS2 transcript levels are calculated relative to EF1α. In study 2, murine samples were analyzed with Taqman Gene Expression Assays: Actb (actin, Mm02619580), Col18a1 (collagen XVIII, Mm00487131), GAPDH (Mm99999915), and SorCS2 (Mm00473050). Col18a1 and SorCS2 transcript levels are relative to beta-actin or glyceraldehyde 3-phosphate dehydrogenase (GAPDH).

2.6 Laser capture microdissection

Fiber tracts of the left hemisphere ipsilateral to the occluded artery were isolated using laser capture microdissection (LCM) five days after CCAo and three days after a single tamoxifen dose from fresh frozen tissue fixed in -20 °C acetone/methanol (1:1). Samples were dissolved in 5 M guanidinium-HCl (Serva) and their proteome was analyzed.

2.7 Immunohistochemistry

For histological, biochemical, and proteome analysis, mice were sacrificed by transcardial perfusion in deep anesthesia (100 µl Ketamine/Xylazine (0.7 % Ketamine (10 %, cb pharma), 0.8 % Xylazine (20 mg/ml Xylavet, cb pharma)) per 10 g body weight, i.p.). Blood was sampled from the vena cava, analyzed (scil Vet abc animal blood counter, scil animal care company, Viernheim, Germany; mouse program), left to clot for 30 min, and spun down for 30 min at 4 °C at 290 xg to generate serum. Mice were perfused using 0.9 % saline water. For proteome analysis, protease inhibitor was added to the perfusion medium (cOmplete™, Roche). Subsequently, mouse brains were taken out, deep-frozen in -45 °C cold 2-methyl butane, and stored at -80 °C until further processing.
For LCM and immunohistochemistry, tissue was cut into 20 µm thick slices with a cryostat (Leica) and fixed in -20 °C acetone/methanol (1:1). Sections were stained overnight and counterstained using 4′,6-diamidino-2-phenylindole (DAPI). To reduce background fluorescence, sudan black treatment was applied before mounting. Imaging was carried out on a Leica SP8 confocal microscope using LAS X software on a 20x objective (HC PL APO CS2).
In study 2, mice were perfused transcardially with a solution of DyLight488-labeled lectin (#DL-1174 Vectorlab; 1 mg/ml; 4 µl/g bodyweight) for 180 s followed by 4 % paraformaldehyde (PFA) in phosphate-buffered saline (PBS). This was followed by 24 h post-fixation in 4 % PFA and 36 h in 30 % sucrose/PBS for cryoprotection and snap-frozen in isopentane before sectioning.

The following primary antibodies were used for staining:
Anti-Caprin-1(ab244360, Abcam, 1:200), anti-GAT-1(NBP1-59878, Novus Biologicals, 1:200), anti-GFAP (C9205, Sigma, 1:1,000, coupled to Cy3, for mouse tissue and cells), anti-GFAP (monoclonal mouse, Sigma, 1:4,000, for human tissue), anti-Myc-Tag (9B11)(2233, Cell Signaling, 1:100, coupled to Alexa647), anti-NeuN (MAB377B, Merck/Millipore, 1:100 and 1:200, for murine tissue), anti-NeuN (MAB377 (clone A60), Millipore, 1:2,000, for human tissue), anti-SorCS2 (R&D Systems, AF4237, 1:100, for mouse tissue and cells; anti-SorCS2, Lifespan Biosciences, LS-C501334, 1:450, for human tissue).

2.8 Image analysis

In study 2, the lesion size of stroked animals was determined in images of NeuN, GFAP, and DAPI stained tissue sections using ImageJ software. The respective area was selected manually and measured. The blood vessel area was analyzed using Cell Profiler software. The length of blood vessels was determined manually using the NeuronJ plugin of ImageJ.

2.9 Statistical analyses

GraphPad Prism version 8.2.0 was used for statistical analysis and graphs. Data are shown as scatter dot plots with the mean ± standard deviation with P-values of <0.05 set as significant. Details for the tests used can be found in the respective publication's figure legends. Where normality could be assumed, t-tests, one- and two-way analyses of variance (ANOVA) with Sidak's posthoc comparisons were applied. Outlier analysis was performed using Grubb's and ROUT tests, and outliers were excluded subsequently.

2.10 Methods to prevent bias

All experimenters were blinded to the genotype during the experiments and analysis to prevent bias. Surgery was performed in a random order within a group of mice.

3. Results

3.1 IL-6 mediates brain remodeling after unilateral CCAo

In the first study, the main results comprise the analysis of brain-exclusive IL-6 increase and the effects on CCAo recovery using a newly generated mouse model.[46]

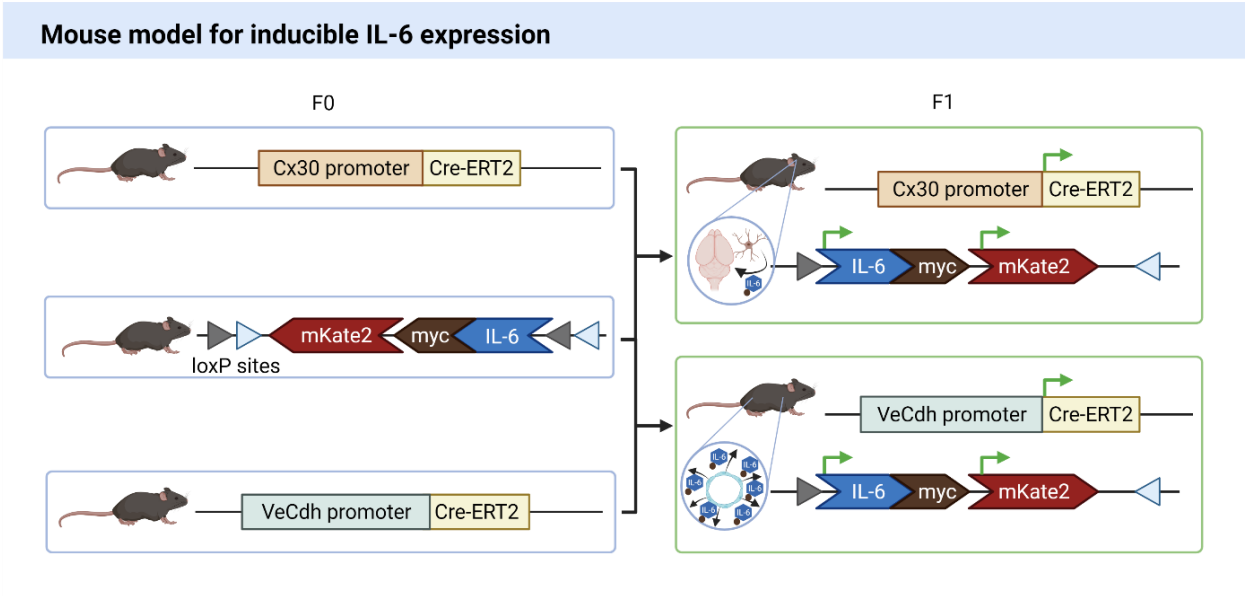

Figure 2 Mouse models used in study 1 (own representation). The mouse model for inducible secretion of IL-6 uses an inverted FLEX cassette flanked by two different loxP sites inserted into the R26 locus. The FLEX cassette encodes IL-6 linked to a myc-tag and after a self-cleavage site mKate2. Upon recombination by Cre recombinase, the cassette is inverted irreversibly due to the excision of the second loxP site. This model uses the tamoxifen-inducible recombinase Cre-ERT2 for induction at any chosen time point. To achieve tissue specificity, FLEX-Il6 mice are cross-bred with mice that express Cre-ERT2 under the control of either the promotor Cx30 for brain-specific IL-6 secretion by astrocytes or VeCdh for systemic IL-6 secretion in all endothelial cells.

The new mouse model allows time-specific, brain-exclusive expression of IL-6 as a paracrine-acting cytokine. It had an inverted FLEX-cassette coding for IL-6 linked to a myc-tag followed by a T2A self-cleavage sequence and the fluorescent protein mKate2 (*Figure 2; Publication 1, Figure 1A*). Crossbreeding with Cx30-Cre-ERT2 mice resulted in the desired mouse line in which there is a brain-exclusive increase in IL-6 following tamoxifen administration. This was shown by assessing IL-6 expression in brain homogenate by western-blotting and in blood by ELISA (*Publication 1, Figure 1B-D*), with IL-6 increasing significantly in the brain after a single dose compared to controls, but not in serum samples. This mouse line was then used to analyze the effects of IL-6 secreted by astrocytes and acting locally on other cells and structures in a carotid artery occlusion model.

To analyze the potentially detrimental effects of paracrine IL-6, it was verified that the mice did not show ischemic or white matter lesions in MRI scans within three weeks after the occlusion. Several tests were performed during the pre- and post-occlusion periods to investigate the recovery of the mice in behavioral studies. In the IL-6 overexpressing mice, there was no alteration in sickness score (modified de Simoni's neuroscore, $p=0.15$) or fine and gross-motor skills assessed by staircase pellet reaching (right paw: $p=0.64$, left paw: $p=0.74$) and RotaRod ($p=0.34$) up to 21 days after surgery (all tests 2-way ANOVA with Sidak's multiple comparison test, *Publication 1, Figure 2*). This confirmed that moderate increases of IL-6 do not exhibit negative effects in a CCA occlusion setting. Looking at connectivity within different brain regions, significant changes were detected in 17 out of 23562 connections when the threshold was $p<0.001$. Out of these, 14 were verified as existing connections by cross-checking in tracing databases. Overall, more connections increased (10) than reduced (4) in connectivity. While intra- and inter-hemispheric connectivity increased mainly in the basal ganglia and the axis from the contralateral motor cortex to the ipsilateral pallidum, reduced connectivity remained intra-hemispheric (*Publication 1, Figure 3*). This qualitative analysis of network remodeling indicates a possible gain of function on the contralateral side to compensate for minor losses on the ipsilateral side.

The next step was to analyze the molecular changes caused by paracrine IL-6 to pinpoint potential mediators of the observed remodeling or other possibly beneficial factors in CCA occlusion. To this end, tissue was sampled from ipsilateral striatal fiber tracts and the contralateral motor cortex by laser capture microdissection. Both experiments showed differentially expressed proteins when a cut-off of $p<0.05$ and a false discovery rate (FDR) of 1 % were set. Several possibly harmful molecules such as synuclein-gamma and pro-enkephalin, both associated with degenerative processes, [49,50] as well as proteins that may exert neuroplastic abilities, such as caprin-1 and protein phosphatase 1 regulatory subunit 1A, where detected with high abundance in the striatal samples.[51,52] In total, 16 out of 2075 detected proteins had altered expression. The cortical samples showed 13 out of 2578 differentially expressed proteins. Most of them were membrane- or transport-associated, suggesting a role in fine-tuning neuronal vesicle transport. One example is the downregulation of Slc6a1, also known as Gat1, a γ-aminobutyric acid (GABA) transporter in the synaptic cleft. Caprin-1 and Gat1 regulation – among the most strongly altered hits for the striatum or cortex, respectively – were verified by immunohistochemical staining.

3.2 SorCS2 is secreted by astrocytes and regulates endostatin after stroke

In the second study, the main results comprise the discovery of SorCS2 upregulation in astrocytes after stroke and the analysis of its role in the physiological and post-stroke situation in mice.[53]

SorCS2 expression, until now only shown in neurons, is induced in astrocytes in an ischemic stroke mouse model and stroke patients (*Publication 2, Figure1*). This is especially the case for the glial scar region, the peri-infarct area, and parts of the contralateral cortex.

Transforming growth factor beta 1 (TGF-β1) is a cytokine associated with stroke recovery processes, most notably angiogenesis.[54,55] Its expression is upregulated after stroke in patients and mice.[56,57] TGF-β1 was also upregulated in the ischemic hemisphere in this study. This led to an upregulation of SorCS2 mRNA in primary murine and human astrocyte cultures and increased SorCS2 protein in the murine cells (*Publication 2, Figure 2*). This effect of TGF-β1 was not seen in primary neurons.

SorCS2 knock-out mice had comparable lesion sizes and astrocytic activation seen by GFAP-measured astrogliosis (*Publication 2, Figure 3*) on day three after MCAo. A measured cytokine panel of 24 cytokines showed no differential expression between SorCS2 deficient mice and controls or hemispheres for 11 proteins, mainly interleukins and interferon gamma (IFNγ) (*Publication 2, Figure S5)*. Remarkably, this was also true for IL-6, which we hypothesized to be regulated by SorCS2. Other cytokines were regulated between hemispheres but not between experimental groups.

A protein array of brain tissue samples was used to identify specific proteins regulated by SorCS2 by comparing wild-type and knock-out mice. Two target proteins, insulin-like growth factor-binding protein 3 (IGFBP3) and endostatin, were not induced to the same degree as in control mice (*Publication 2, Figure 4a - c*). The focus was on endostatin as it exhibits anti-angiogenic effects and is a protein of interest in other post-stroke studies acting via modulation of the mitogen activated protein kinase (MAPK/ERK) signaling pathway.[16,58,59] Endostatin levels correlated to the size of the ischemic lesion and remained brain exclusive in wild-type mice. The lack of endostatin upregulation and increased ERK phosphorylation on the ipsilateral hemisphere was confirmed in SorCS2-deficient mice. (*Publication 2, Figure 4d – g and Figure S7*).

To support the *in vivo* results, experiments with primary astrocytic cells in culture with stimulated cytokine production using phorbol 12-myristate 13-acetate (PMA) and ionomycin. In line with previous findings, SorCS2 knock-out mice had a reduced expression and cell levels of endostatin while secreting other cytokines normally (*Publication 2, Figure 5*). Transcript levels of the endostatin precursor collagen XVIII were identical to controls, suggesting regulation of proteolysis of collagen XVIII or other post-translational mechanisms. This further proved that astrocytes secrete endostatin in a SorCS2-dependent manner.

Looking at the effects of SorCS2, modulation of angiogenesis seems likely. Investigation of vessels 21 days after MCAo with DyLight488-labeled lectin showed an increase in vessel area and length in the ipsilateral brain half in wild-type mice, especially in the glial scar region and the peri-infarct area, , while the contralateral side remained unchanged. There was no increase in SorCS2-deficient mice, independent of the hemisphere (*Publication 2, Figure 6 and S9*).

In summary, the study shows for the first time that SorCS2 is upregulated in astrocytes after ischemic stroke, exhibiting effects on the expression of endostatin and angiogenesis.

3.3 A data driven approach using machine learning provides humane endpoints in murine stroke models

The third study reviews current methods for the determination of humane endpoints and provides novel models for endpoint prediction in murine sepsis and stroke models.[47] My contribution focused on the stroke model and the data evaluation, so I will exclusively highlight the results of this part.

Initially, we wanted to assess the effects of local and systemic IL-6 in the brain. Similar to the astrocytic mouse model, we could induce IL-6 systemically with low tamoxifen doses in the endothelial FLEX-IL6 mouse model. Amounts of 40 mg/kg body weight on one to three consecutive days led to a positive feedback loop of IL-6, resulting in a cytokine storm and ultimately to a SIRS-like state of the mice with severe sickness behavior. Mice had to be euthanized at a specific sickness state or even died before a humane endpoint could be set, so that behavioral studies were not possible. This led to the question whether we could predict if an animal will die in an experiment based on body measurements and behavioral data. Subsequently, we standardized the selection of behavioral

tests and time points and compiled the existing data into one coherent data set that allows for secondary use of the data.

The data for training the models were selected and compiled from a multitude of behavioral experiments in which MCAo was studied for 21 days. Sham-operated animals served as controls. Parameters monitored include daily weight and core body temperature and a modified DeSimoni's neuroscore as a sickness indicator on day -5 before and day 1, 2, 7, 14, and 21 after ischemia. The score ranges from 0, indicating no impairment, to 42, maximum impairment.

When comparing data, there was a drop in body temperature in MCAo mice during the first 5 days after surgery compared to baseline values. For non-surviving animals, this decrease is 3.5 °C higher than for surviving animals. The weight decreased in all groups, again most prominently in the non-survivor group, where the average weight loss was 5.9 g compared to 4 g in survivors and 2.4 g in controls. Neuroscores on days 1 and 2 after MCAo compared to baseline were again lowest in sham animals (4), prominent in MCAo survivors (8.77), and highest in non-survivors (15) (*Publication 3, Table 3A*). Generally, the highest scores were observed on day 1 after surgery.

All data were gathered, and two sets of parameters used for training: the values of the measurements and the change per time-point of the values with subtraction of the baseline value. Parameters considered for analysis were time points before the average time of death after MCAo (3.9 days). As the weight differed significantly between genders ($p < 0.001$, Mann-Whitney U test), both genders were analyzed separately.

Prediction models based on Gaussian Naïve Bayes set boundaries using a single parameter were able to correctly predict death with an accuracy of 90.7 % for male mice and 86.3 % in female mice, when using only the weight change on day 3 or 2 in females, respectively. Accuracy, sensitivity, and precision were further improved when other parameters were added. For males, a combination of weight change on days 1 and 3 and the core body temperature as parameters for the model yielded an accuracy of 93.2 %. Using this prediction model, 13 out of 23 animals could have been euthanized one day earlier on day 3, while the average time to death was 4.08 days after surgery. In female mice, the best parameter combination was neuroscore, weight change, and core temperature change on day 2. With this model, 4 out of 10 animals could have been euthanized earlier on day 2, while the average time to death was 4.25 days after surgery. 3 out of 77 animals (3.95 %) were wrongly predicted to die by the algorithm and survived in the experiment (*Publication 3, Figure 2A, B and Table 4A*).

In summary, the newly developed machine learning based prediction model has the potential to improve animal research by determining a humane endpoint to reduce suffering.

4. Discussion

This thesis unravels the molecular and structural impact of two signaling molecules on the ischemic brain periphery during recovery. Consequently, it presents novel targets for new therapeutic options in carotid artery occlusion and ischemic stroke. This thesis
(1) analyzed the effects of brain exclusive IL-6 increase in unilateral carotid occlusion in mice and found an increase in brain connectivity for 10 out of 14 altered connections and presented Caprin-1 and Gat1 as potential therapeutic targets out of 39 differentially expressed proteins in the local proteome.
(2) investigated the role of SorCS2 in post-stroke angiogenesis and recovery, showed novel expression of SorCS2 by reactive astrocytes, and found a link between SorCS2 and endostatin expression.
(3) contributed to the re-use of data and reduction of animal suffering in experimental research by aggregating data into one cohesive dataset and training an algorithm to find humane endpoints in animal models.

4.1 Summary, interpretation and embedding into the state of the art research

The first study shows that IL-6 does not lead to detrimental effects in a moderate recovery period but instead fosters the formation of intra- and inter-hemispheric connections. Additionally, it leads to the differential expression of several proteins relevant to brain regeneration and cognitive function retention. We demonstrate that brain-exclusive paracrine-acting IL-6 alone does not cause obvious behavioral deficits in the assessment of fine and gross motor skills and the overall health status. In carotid stenosis patients, IL-6 levels are usually measured only in the blood and not in the brain. High blood IL-6 levels are a poor prognostic marker and are a characteristic of unstable plaques and thus affecting patients' health.[36,37]. Elevated systemic IL-6 levels might influence the health status in CCAo mice but are not studied in this thesis due to the dosage difficulties in the VECdh-Cre-ERT2; FLEX-IL6 mouse model.
Using connectome analysis, we found that connectivity increase outweighs decreases in this paracrine IL-6 model. This is especially true between the hemispheres and in the hindbrain, particularly in the periaqueductal grey. This region serves as a relay between the brainstem and the forebrain, suggesting a stronger motor signaling towards the spinal cord.[60]

In the subsequent proteome analysis, we identified differentially regulated candidates that present attractive targets for modulating regeneration and preventing the loss of cerebral function. Possible detrimental and beneficial effects through up- or downregulation of specific proteins were found in both analyzed regions. We selected the most interesting targets for a potential intervention based on the strongest regulation and the effects reported in previous studies and confirmed them in using immunohistology: Caprin-1 and Gat1. Caprin-1 upregulation is associated with the formation of stress granules.[61] It plays a role in establishing long-term potentiation (LTP) and might be necessary for regenerative plasticity.[51] The widely downregulated protein Gat1 is an axonal transporter, removing GABA from the synaptic cleft and negatively regulating GABA-signaling.[62] This regulation is exciting, as specifically the GABAergic axis from the ipsilateral dorsal thalamic nuclei to the ipsilateral pallidum and contralateral motor area was increased in DTI analysis. This indicates an even more pronounced strengthening of GABA signaling between the thalamus and motor cortex. Higher GABA levels in this circuit were associated with less severe symptoms in Parkinson's patients.[63] In contrast, GABAergic signaling is critical for the long-term inhibition of synaptic transmission.[64] Full removal of Gat1 was shown to cause learning deficits, while Gat1 reduction led to improved learning, indicating the need for specific dosing to achieve beneficial effects.[65,66] Tiagabine, a Gat1 inhibitor drug, is used to treat epilepsy patients without impairing cognitive function.[67] In the acutely ischemic brain, tiagabine treatment showed neuroprotective effects.[68,69] Further analysis of the impact of Gat1-inhibition by tiagabine in carotid occlusion will yield attractive options in an alternative ischemic setting. The same is true for following up on other hits like the lower expression protein Vamp3, shown to limit microglial activity after surgical trauma, or high expression Atpif1, able to rescue cells in hypoxia.[70,71] Studying these molecules is more challenging with regard to the subsequent translation into the clinic, as no established treatment option is readily available.

In the second study, we unraveled that reactive astrocytes express SorCS2 after stroke. Until now, expression was only confirmed by neuronal cells.[42] The activation of expression is likely mediated by TGF-β1, validated by astrocyte culture experiments. Effects of abolishing SorCS2 were no induction of endostatin expression. Control mice had a notable endostatin increase after MCAo. SorCS2 depletion did not affect lesion size or cytokine expression, indicating a particular role in post-stroke modulation. This was surprising as it disproved that IL-6 secretion is mediated by SorCS2 receptor sorting and of the

VPS10p receptors, only SorLA is responsible for IL-6 shuttling.[45] Most likely, SorCS2 modulates the post-ischemic micromilieu by affecting angiogenesis via endostatin levels, regulating the conversion from its precursor collagen XVIII. Endostatin inhibits angiogenesis in tumor models and can reverse pro-angiogenetic effects of physical activity after MCAo in mice.[16] 21 days post-stroke, we found that SorCS2 knock-out mice had reduced vessel counts in the ischemic hemisphere, which seems to contradict the accompanying lowered endostatin levels. Angiogenesis, especially after stroke, is an orchestrated and timed process triggered by a balance of pro- and anti-angiogenic molecules activated by hypoxia.[72,73] A general boost of new vessel formation by VEGF has, for example, improved and complicated post-stroke regeneration due to the leaky nature of the newly formed vessels, which are prone to edema-formation. At the same time, angiopoietin co-release helps mitigate the leakiness.[74] This highlights the complex role of post-stroke angiogenesis, where SorCS2 is a decisive factor, as shown by this study

The third study provides a systematic overview of current approaches to reduce animal suffering by determining humane endpoints in various disease models and provides machine-learning based tools to reliably identify animals that can be spared additional suffering in stroke and sepsis models. In preparation for the study, all research protocols for behavioral experiments in stroke models were standardized, data collection unified, and one extensive database generated. This allowed the development of the machine learning algorithm on a large set of experimental data with extremely high sample sizes and thus a high statistical power. Humane endpoints in murine stroke models were not assessed previously to this study. There are several other studies on humane endpoints in animal research in different disease models as explicitly listed in this publication.[47] Due to the high specificity of the mouse models, the algorithms cannot be transferred to other mouse models. Another benefit of the presented prediction model is the use of common measurements such as core body temperature, weight changes, and neuroscore. These cause no additional handling stress for the animals. Assessing whether an animal has reached the humane endpoint can be easily integrated into the ongoing research based on measurements recorded daily. The standardization of research protocols will allow a growing pool of research data and potentially expand meta-research approaches.

4.2 Strengths and weaknesses

The first study investigates the effects of paracrine-acting IL-6 in a unilateral carotid occlusion model to explore global changes in connectivity and therapeutic targets with a more distinct mechanism of action than IL-6. This investigative approach leaves room for more in-depth studies. It does not provide a complete insight into the mechanisms of IL-6 signaling in the model used, which is also reflected in the sample size. Besides, similar unilateral CCAo rodent models have caused spatial memory and object recognition impairments, accompanied by elevated IL-6 levels.[75,76] The study shows connectivity changes involving motor fibers but with no apparent effects on motor behavior. This could be attributable to the low sensitivity of the behavioral tests and the relatively subtle effects of altered brain connections. Long-term follow-up and further behavioral studies, including memory testing, can help unravel the potential of IL-6 in CCAo even more.
Using LCM to isolate fiber tracts is a promising technique. Previously, proteome analysis of fiber tracts was only successful in the developing mouse or using advanced methods due to high-fat content of the tissue.[77,78]
The model for astrocytic IL-6 activation does lead to a permanent secretion of IL-6, even though levels remain moderate and confined to the brain. IL-6 is a cytokine with various effects, and thus, we cannot exclude that this might cause more detrimental effects in the long term. Therefore, we focused on finding proteins serving as potential targets rather than trying to unravel detailed dose- and time-dependent short- and long-term consequences.

The SorCS2 study stresses the importance of anti-angiogenic proteins in post-stroke recovery and provides novel insights about SorCS2 after stroke, especially its secretion by astrocytes. This study used a constitutive knock-out model, and it cannot be excluded that the effects of neuronal SorCS2 outweigh and even compensate for the lack of astrocytic SorCS2. Further studies with a conditional knock-out at the time of injury or shortly after can address this and provide a better insight into the specific post-stroke effects of the sortilin receptor. As mentioned above, angiogenesis is a complex process, and we focused on SorCS2 alone. More detailed insights will be possible with further studies analyzing the interplay between relevant mediators of angiogenesis such as VEGF and SorCS2.

The presented algorithms provide a simple tool to prevent unnecessary suffering in commonly used animal models in behavioral research. However, 24 – 36 h is a relatively short period of time to reduce suffering. As the data set is comparatively small for a machine learning approach, especially in the non-survivor group, further optimization can be achieved by continuously updating the model or using more data, for example, continuous measurement of body temperature. The novel database is a valuable resource for new approaches in animal research using meta-research. Larger sample sizes allow better-powered analyses without further inflicting damage to animals and are a starting point to generate and test hypotheses without the need for new behavioral studies.

5. Conclusions

This thesis investigates the astrocyte-mediated molecular adaptations after focal ischemia and carotid occlusion by evaluating the effects of IL-6 and SorCS2. Both mediated beneficial effects in our study settings. Due to the complex interplay both molecules have the potential to negatively affect outcomes in different disease models or in the long term. Contrary to the initial hypothesis, we did not find a direct link between both molecules.
The unified data gathered from murine stroke models allowed to build a large database with physiological and behavioral data. This was the prerequisite to developing an algorithm that predicts humane endpoints and can prevent animal suffering in future behavioral tests with murine MCAo models. It also gives the opportunity to answer future research question using existing data and reduces the need for animals in research. This thesis conducts preclinical research and provides the target molecules Caprin-1, Gat1, SorCS2 and endostatin. After verification in preclinical and clinical studies, these molecules and are exciting options for the treatment of stroke and carotid stenosis.

Reference list

1. Statistisches Bundesamt (Destatis). Causes of death by chapters of the ICD-10 and gender. https://www.destatis.de/EN/Themes/Society-Environment/Health/Causes-Death/Tables/number-of-death.html (2021).
2. Heron, M. Deaths: leading causes for 2019. *National Vital Statistics Reports* **70**, 1–113 (2021).
3. Johnson, C. O., Roth, G. A., Bisignano, C., Abady, G. G., Abbasifard, M., Abbasi-Kangevari, M., Abd-Allah, F., Abedi, V., Abualhasan, A., Abu-Rmeileh, N. M., Abushouk, A. I., Adebayo, O. M., Agarwal, G., Agasthi, P., Ahinkorah, B. O., Ahmad, S., Ahmadi, S., Salih, Y. A., Aji, B., Akbarpour, S., Akinyemi, R. O., Hamad, H. al, Alahdab, F., Alif, S. M., Alipour, V., Aljunid, S. M., Almustanyir, S., Al-Raddadi, R. M., Salman, R. A.-S., Alvis-Guzman, N., Ancuceanu, R., Anderlini, D., Anderson, J. A., Ansar, A., Antonazzo, I. C., Arabloo, J., Ärnlöv, J., Artanti, K. D., Aryan, Z., Asgari, S., Ashraf, T., Athar, M., Atreya, A., Ausloos, M., Baig, A. A., Baltatu, O. C., Banach, M., Barboza, M. A., Barker-Collo, S. L., Bärnighausen, T. W., Barone, M. T. U., Basu, S., Bazmandegan, G., Beghi, E., Beheshti, M., Béjot, Y., Bell, A. W., Bennett, D. A., Bensenor, I. M., Bezabhe, W. M., Bezabih, Y. M., Bhagavathula, A. S., Bhardwaj, P., Bhattacharyya, K., Bijani, A., Bikbov, B., Birhanu, M. M., Boloor, A., Bonny, A., Brauer, M., Brenner, H., Bryazka, D., Butt, Z. A., Santos, F. L. C. dos, Campos-Nonato, I. R., Cantu-Brito, C., Carrero, J. J., Castañeda-Orjuela, C. A., Catapano, A. L., Chakraborty, P. A., Charan, J., Choudhari, S. G., Chowdhury, E. K., Chu, D.-T., Chung, S.-C., Colozza, D., Costa, V. M., Costanzo, S., Criqui, M. H., Dadras, O., Dagnew, B., Dai, X., Dalal, K., Damasceno, A. A. M., D'Amico, E., Dandona, L., Dandona, R., Gela, J. D., Davletov, K., Cruz-Góngora, V. D. la, Desai, R., Dhamnetiya, D., Dharmaratne, S. D., Dhimal, M. L., Dhimal, M., Diaz, D., Dichgans, M., Dokova, K., Doshi, R., Douiri, A., Duncan, B. B., Eftekharzadeh, S., Ekholuenetale, M., Nahas, N. el, Elgendy, I. Y., Elhadi, M., El-Jaafary, S. I., Endres, M., Endries, A. Y., Erku, D. A., Faraon, E. J. A., Farooque, U., Farzadfar, F., Feroze, A. H., Filip, I., Fischer, F., Flood, D., Gad, M. M., Gaidhane, S., Gheshlagh, R. G., Ghashghaee, A., Ghith, N., Ghozali, G., Ghozy, S., Gialluisi, A., Giampaoli, S., Gilani, S. A., Gill, P. S., Gnedovskaya, E. v, Golechha, M., Goulart, A. C., Guo, Y., Gupta, R., Gupta, V. B., Gupta, V. K., Gyanwali, P., Hafezi-Nejad, N., Hamidi, S., Hanif, A., Hankey, G. J., Hargono, A., Hashi, A., Hassan, T. S., Hassen, H. Y.,

Havmoeller, R. J., Hay, S. I., Hayat, K., Hegazy, M. I., Herteliu, C., Holla, R., Hostiuc, S., Househ, M., Huang, J., Humayun, A., Hwang, B.-F., Iacoviello, L., Iavicoli, I., Ibitoye, S. E., Ilesanmi, O. S., Ilic, I. M., Ilic, M. D., Iqbal, U., Irvani, S. S. N., Islam, S. M. S., Ismail, N. E., Iso, H., Isola, G., Iwagami, M., Jacob, L., Jain, V., Jang, S.-I., Jayapal, S. K., Jayaram, S., Jayawardena, R., Jeemon, P., Jha, R. P., Johnson, W. D., Jonas, J. B., Joseph, N., Jozwiak, J. J., Jürisson, M., Kalani, R., Kalhor, R., Kalkonde, Y., Kamath, A., Kamiab, Z., Kanchan, T., Kandel, H., Karch, A., Katoto, P. D., Kayode, G. A., Keshavarz, P., Khader, Y. S., Khan, E. A., Khan, I. A., Khan, M., Khan, M. A., Khatib, M. N., Khubchandani, J., Kim, G. R., Kim, M. S., Kim, Y. J., Kisa, A., Kisa, S., Kivimäki, M., Kolte, D., Koolivand, A., Laxminarayana, S. L. K., Koyanagi, A., Krishan, K., Krishnamoorthy, V., Krishnamurthi, R. v, Kumar, G. A., Kusuma, D., Vecchia, C. la, Lacey, B., Lak, H. M., Lallukka, T., Lasrado, S., Lavados, P. M., Leonardi, M., Li, B., Li, S., Lin, H., Lin, R.-T., Liu, X., Lo, W. D., Lorkowski, S., Lucchetti, G., Saute, R. L., Razek, H. M. A. el, Magnani, F. G., Mahajan, P. B., Majeed, A., Makki, A., Malekzadeh, R., Malik, A. A., Manafi, N., Mansournia, M. A., Mantovani, L. G., Martini, S., Mazzaglia, G., Mehndiratta, M. M., Menezes, R. G., Meretoja, A., Mersha, A. G., Jonasson, J. M., Miazgowski, B., Miazgowski, T., Michalek, I. M., Mirrakhimov, E. M., Mohammad, Y., Mohammadian-Hafshejani, A., Mohammed, S., Mokdad, A. H., Mokhayeri, Y., Molokhia, M., Moni, M. A., Montasir, A. al, Moradzadeh, R., Morawska, L., Morze, J., Muruet, W., Musa, K. I., Nagarajan, A. J., Naghavi, M., Swamy, S. N., Nascimento, B. R., Negoi, R. I., Kandel, S. N., Nguyen, T. H., Norrving, B., Noubiap, J. J., Nwatah, V. E., Oancea, B., Odukoya, O. O., Olagunju, A. T., Orru, H., Owolabi, M. O., Padubidri, J. R., Pana, A., Parekh, T., Park, E.-C., Kan, F. P., Pathak, M., Peres, M. F. P., Perianayagam, A., Pham, T.-M., Piradov, M. A., Podder, V., Polinder, S., Postma, M. J., Pourshams, A., Radfar, A., Rafiei, A., Raggi, A., Rahim, F., Rahimi-Movaghar, V., Rahman, M., Rahman, M. A., Rahmani, A. M., Rajai, N., Ranasinghe, P., Rao, C. R., Rao, S. J., Rathi, P., Rawaf, D. L., Rawaf, S., Reitsma, M. B., Renjith, V., Renzaho, A. M. N., Rezapour, A., Rodriguez, J. A. B., Roever, L., Romoli, M., Rynkiewicz, A., Sacco, S., Sadeghi, M., Moghaddam, S. S., Sahebkar, A., Saif-Ur-Rahman, K., Salah, R., Samaei, M., Samy, A. M., Santos, I. S., Santric-Milicevic, M. M., Sarrafzadegan, N., Sathian, B., Sattin, D., Schiavolin, S., Schlaich, M. P., Schmidt, M. I., Schutte, A. E., Sepanlou, S. G., Seylani, A., Sha, F., Shahabi, S., Shaikh, M. A., Shannawaz, M., Shawon, M. S. R., Sheikh, A., Sheikhbahaei, S.,

Shibuya, K., Siabani, S., Silva, D. A. S., Singh, J. A., Singh, J. K., Skryabin, V. Y., Skryabina, A. A., Sobaih, B. H., Stortecky, S., Stranges, S., Tadesse, E. G., Tarigan, I. U., Temsah, M.-H., Teuschl, Y., Thrift, A. G., Tonelli, M., Tovani-Palone, M. R., Tran, B. X., Tripathi, M., Tsegaye, G. W., Ullah, A., Unim, B., Unnikrishnan, B., Vakilian, A., Tahbaz, S. V., Vasankari, T. J., Venketasubramanian, N., Vervoort, D., Vo, B., Volovici, V., Vosoughi, K., Vu, G. T., Vu, L. G., Wafa, H. A., Waheed, Y., Wang, Y., Wijeratne, T., Winkler, A. S., Wolfe, C. D. A., Woodward, M., Wu, J. H., Hanson, S. W., Xu, X., Yadav, L., Yadollahpour, A., Jabbari, S. H. Y., Yamagishi, K., Yatsuya, H., Yonemoto, N., Yu, C., Yunusa, I., Zaman, M. S., Zaman, S. bin, Zamanian, M., Zand, R., Zandifar, A., Zastrozhin, M. S., Zastrozhina, A., Zhang, Y., Zhang, Z.-J., Zhong, C., Zuniga, Y. M. H. & Murray, C. J. L. Global, regional, and national burden of stroke and its risk factors, 1990-2019: a systematic analysis for the Global Burden of Disease Study 2019. *The Lancet Neurology* **20**, 795–820 (2021).

4. Fieschi, C., Argentino, C., Lenzi, G. L., Sacchetti, M. L., Toni, D. & Bozzao, L. Clinical and instrumental evaluation of patients with ischemic stroke within the first six hours. *J Neurol Sci* **91**, 311–321 (1989).
5. Lal, B. K., Dux, M. C., Sikdar, S., Goldstein, C., Khan, A. A., Yokemick, J. & Zhao, L. Asymptomatic carotid stenosis is associated with cognitive impairment. *Journal of Vascular Surgery* **66**, 1083–1092 (2017).
6. de Los Ríos la Rosa, F., Khoury, J., Kissela, B. M., Flaherty, M. L., Alwell, K., Moomaw, C. J., Khatri, P., Adeoye, O., Woo, D., Ferioli, S. & Kleindorfer, D. O. Eligibility for Intravenous Recombinant Tissue-Type Plasminogen Activator Within a Population The Effect of the European Cooperative Acute Stroke Study (ECASS) III Trial. *Stroke* **43**, 1591–1595 (2012).
7. Yang, P., Zhang, Y., Zhang, L., Zhang, Y., Treurniet, K. M., Chen, W., Peng, Y., Han, H., Wang, J., Wang, S., Yin, C., Liu, S., Wang, P., Fang, Q., Shi, H., Yang, J., Wen, C., Li, C., Jiang, C., Sun, J., Yue, X., Lou, M., Zhang, M., Shu, H., Sun, D., Liang, H., Li, T., Guo, F., Ke, K., Yuan, H., Wang, G., Yang, W., Shi, H., Li, T., Li, Z., Xing, P., Zhang, P., Zhou, Y., Wang, H., Xu, Y., Huang, Q., Wu, T., Zhao, R., Li, Q., Fang, Y., Wang, L., Lu, J., Li, Y., Fu, J., Zhong, X., Wang, Y., Wang, L., Goyal, M., Dippel, D. W. J., Hong, B., Deng, B., Roos, Y. B. W. E. M., Majoie, C. B. L. M. & Liu, J. Endovascular Thrombectomy with or without Intravenous Alteplase in Acute Stroke. *New England Journal of Medicine* **382**, 1981–1993 (2020).

8. Casetta, I., Fainardi, E., Saia, V., Pracucci, G., Padroni, M., Renieri, L., Nencini, P., Inzitari, D., Morosetti, D., Sallustio, F., Vallone, S., Bigliardi, G., Zini, A., Longo, M., Francalanza, I., Bracco, S., Vallone, I. M., Tassi, R., Bergui, M., Naldi, A., Saletti, A., de Vito, A., Gasparotti, R., Magoni, M., Castellan, L., Castellan, L., Serrati, C., Menozzi, R., Scoditti, U., Causin, F., Pieroni, A., Puglielli, E., Casalena, A., Sanna, A., Ruggiero, M., Cordici, F., di Maggio, L., Duc, E., Cosottini, M., Giannini, N., Sanfilippo, G., Zappoli, F., Toni, D., Cavasin, N., Critelli, A., Ciceri, E., Plebani, M., Cappellari, M., Chiumarulo, L., Petruzzellis, M., Terrana, A., Cariddi, L. P., Burdi, N., Tinelli, A., Auteri, W., Silvagni, U., Biraschi, F., Nicolini, E., Padolecchia, R., Tassinari, T., Filauri, P., Sacco, S., Pavia, M., Invernizzi, P., Nuzzi, N. P., Marcheselli, S., Amistà, P., Russo, M., Gallesio, I., Gallesio, I., Craparo, G., Mannino, M. & Mangiafico, S. Endovascular Thrombectomy for Acute Ischemic Stroke Beyond 6 Hours From Onset: A Real-World Experience. *Stroke* **51**, 2051–2057 (2020).
9. Brouns, R. & De Deyn, P. P. The complexity of neurobiological processes in acute ischemic stroke. *Clinical Neurology and Neurosurgery* **111**, 483–495 (2009).
10. Wakita, H., Tomimoto, H., Akiguchi, I. & Kimura, J. Glial activation and white matter changes in the rat brain induced by chronic cerebral hypoperfusion: an immunohistochemical study. *Acta Neuropathologica* **87**, 484–492 (1994).
11. Ueno, M., Nakamura, Y., Li, J., Goulding, M., Baccei, M. L., Ueno, M., Nakamura, Y., Li, J., Gu, Z., Niehaus, J., Maezawa, M. & Crone, S. A. Corticospinal Circuits from the Sensory and Motor Cortices Differentially Regulate Skilled Movements through Distinct Spinal Interneurons Article Corticospinal Circuits from the Sensory and Motor Cortices Differentially Regulate Skilled Movements through Distinct Spinal Interneurons. *CellReports* **23**, 1286-1300.e7 (2018).
12. Holland, P. R., Searcy, J. L., Salvadores, N., Scullion, G., Chen, G., Lawson, G., Scott, F., Bastin, M. E., Ihara, M., Kalaria, R., Wood, E. R., Smith, C., Wardlaw, J. M. & Horsburgh, K. Gliovascular disruption and cognitive deficits in a mouse model with features of small vessel disease. *J Cereb Blood Flow Metab* **35**, 1005–1014 (2015).
13. Duncombe, J., Kitamura, A., Hase, Y., Ihara, M., Kalaria, R. N. & Horsburgh, K. Chronic cerebral hypoperfusion: A key mechanism leading to vascular cognitive impairment and dementia. Closing the translational gap between rodent models and human vascular cognitive impairment and dementia. *Clinical Science* **131**, 2451–2468 (2017).

14. Bachmann, L. C., Lindau, N. T., Felder, P. & Schwab, M. E. Sprouting of brainstem-spinal tracts in response to unilateral motor cortex stroke in mice. *J Neurosci* **34**, 3378–3389 (2014).
15. Hoffmann, C. J., Harms, U., Rex, A., Szulzewsky, F., Wolf, S. A., Grittner, U., Lättig-Tünnemann, G., Sendtner, M., Kettenmann, H., Dirnagl, U., Endres, M. & Harms, C. Vascular signal transducer and activator of transcription-3 promotes angiogenesis and neuroplasticity long-term after stroke. *Circulation* **131**, 1772–1782 (2015).
16. Gertz, K., Priller, J., Kronenberg, G., Fink, K. B., Winter, B., Schröck, H., Ji, S., Milosevic, M., Harms, C., Böhm, M., Dirnagl, U., Laufs, U. & Endres, M. Physical activity improves long-term stroke outcome via endothelial nitric oxide synthase-dependent augmentation of neovascularization and cerebral blood flow. *Circulation Research* **99**, 1132–1140 (2006).
17. Hermann, D. M. & Zechariah, A. Implications of vascular endothelial growth factor for postischemic neurovascular remodeling. *J Cereb Blood Flow Metab* **29**, 1620–1643 (2009).
18. Snapyan, M., Lemasson, M., Brill, M. S., Blais, M., Massouh, M., Ninkovic, J., Gravel, C., Berthod, F., Götz, M., Barker, P. A., Parent, A. & Saghatelyan, A. Vasculature guides migrating neuronal precursors in the adult mammalian forebrain via brain-derived neurotrophic factor signaling. *J Neurosci* **29**, 4172–4188 (2009).
19. Anrather, J. & Iadecola, C. Inflammation and Stroke: An Overview. *Neurotherapeutics* **13**, 661–670 (2016).
20. Beck, H. & Plate, K. H. Angiogenesis after cerebral ischemia. *Acta Neuropathologica* **117**, 481–496 (2009).
21. Nishihiro, S., Hishikawa, T., Hiramatsu, M., Kidani, N., Takahashi, Y., Murai, S., Sugiu, K., Higaki, Y., Yasuhara, T., Borlongan, C. V. & Date, I. High-Mobility Group Box-1-Induced Angiogenesis After Indirect Bypass Surgery in a Chronic Cerebral Hypoperfusion Model. *NeuroMolecular Medicine* **21**, 391–400 (2019).
22. Zhang, W., Petrovic, J. M., Callaghan, D., Jones, A., Cui, H., Howlett, C. & Stanimirovic, D. Evidence that hypoxia-inducible factor-1 (HIF-1) mediates transcriptional activation of interleukin-1beta (IL-1beta) in astrocyte cultures. *J Neuroimmunol* **174**, 63–73 (2006).
23. Liu, Q., Bhuiyan, M. I. H., Liu, R., Song, S., Begum, G., Young, C. B., Foley, L. M., Chen, F., Hitchens, T. K., Cao, G., Chattopadhyay, A., He, L. & Sun, D. Attenuating

vascular stenosis-induced astrogliosis preserves white matter integrity and cognitive function. *Journal of Neuroinflammation* **18**, 187 (2021).

24. Ito, M., Komai, K., Mise-Omata, S., Iizuka-Koga, M., Noguchi, Y., Kondo, T., Sakai, R., Matsuo, K., Nakayama, T., Yoshie, O., Nakatsukasa, H., Chikuma, S., Shichita, T. & Yoshimura, A. Brain regulatory T cells suppress astrogliosis and potentiate neurological recovery. *Nature* **565**, 246–250 (2019).
25. Klein, M. A., Möller, J. C., Jones, L. L., Bluethmann, H., Kreutzberg, G. W. & Raivich, G. Impaired Neuroglial Activation in Interleukin-6 Deficient Mice. *GLIA* **19**, 227–233 (1997).
26. Balasingam, V., Tejada-Berges, T., Wright, E., Bouckova, R. & Yong, V. W. Reactive astrogliosis in the neonatal mouse brain and its modulation by cytokines. *J Neurosci* **14**, 846–856 (1994).
27. Pekny, M., Pekna, M., Messing, A., Steinhäuser, C., Lee, J. M., Parpura, V., Hol, E. M., Sofroniew, M. v. & Verkhratsky, A. Astrocytes: a central element in neurological diseases. *Acta Neuropathol* **131**, 323–345 (2016).
28. Tanaka, T., Narazaki, M. & Kishimoto, T. IL-6 in inflammation, immunity, and disease. *Cold Spring Harb Perspect Biol* **6**, a016295 (2014).
29. Bluthé, R.-M., Michaud, B., Poli, V. & Dantzer, R. Role of IL-6 in cytokine-induced sickness behavior: a study with IL-6 deficient mice. *Physiology & Behavior* **70**, 367–373 (2000).
30. Asgarov, R., Sen, K. M., Meena, M., Karl, T., Gyengesi, E., Mahns, D. A., Malladi, C. S. & Münch, G. W. Characterisation of the Mouse Cerebellar Proteome in the GFAP-IL6 Model of Chronic Neuroinflammation. *The Cerebellum* **21**, 404–424 (2021).
31. Gyengesi, E., Rangel, A., Ullah, F., Liang, H., Niedermayer, G., Asgarov, R., Venigalla, M., Gunawardena, D., Karl, T. & Münch, G. Chronic Microglial Activation in the GFAP-IL6 Mouse Contributes to Age-Dependent Cerebellar Volume Loss and Impairment in Motor Function. *Frontiers in Neuroscience* **13**, 303 (2019).
32. Yang, P., Wen, H., Ou, S., Cui, J. & Fan, D. IL-6 promotes regeneration and functional recovery after cortical spinal tract injury by reactivating intrinsic growth program of neurons and enhancing synapse formation. *Experimental Neurology* **236**, 19–27 (2012).
33. Bowen, K., Dempsey, R. & Vemuganti, R. Adult interleukin-6 knockout mice show compromised neurogenesis. *Neuroreport* **22**, 126–130 (2011).

34. Ormstad, H., Aass, H. C. D., Lund-Sørensen, N., Amthor, K. F. & Sandvik, L. Serum levels of cytokines and C-reactive protein in acute ischemic stroke patients, and their relationship to stroke lateralization, type, and infarct volume. *Journal of Neurology* **258**, 677–685 (2011).
35. Bustamante, A., Sobrino, T., Giralt, D., García-Berrocoso, T., Llombart, V., Ugarriza, I., Espadaler, M., Rodríguez, N., Sudlow, C., Castellanos, M., Smith, C. J., Rodríguez-Yánez, M., Waje-Andreassen, U., Tanne, D., Oto, J., Barber, M., Worthmann, H., Wartenberg, K. E., Becker, K. J., Chakraborty, B., Oh, S. H., Whiteley, W. N., Castillo, J. & Montaner, J. Prognostic value of blood interleukin-6 in the prediction of functional outcome after stroke: A systematic review and meta-analysis. *Journal of Neuroimmunology* **274**, 215–224 (2014).
36. Puz, P. & Lasek–Bal, A. Repeated measurements of serum concentrations of TNF-alpha, interleukin-6 and interleukin-10 in the evaluation of internal carotid artery stenosis progression. *Atherosclerosis* **263**, 97–103 (2017).
37. Yamagami, H., Kitagawa, K., Nagai, Y., Hougaku, H., Sakaguchi, M., Kuwabara, K., Kondo, K., Masuyama, T., Matsumoto, M. & Hori, M. Higher Levels of Interlieukin-6 Are Associated with Lower Echogenicity of Carotid Artery Plaques. *Stroke* **35**, 677–681 (2004).
38. Gertz, K., Kronenberg, G., Kälin, R. E., Baldinger, T., Werner, C., Balkaya, M., Eom, G. D., Hellmann-Regen, J., Kröber, J., Miller, K. R., Lindauer, U., Laufs, U., Dirnagl, U., Heppner, F. L. & Endres, M. Essential role of interleukin-6 in post-stroke angiogenesis. *Brain* **135**, 1964–1680 (2012).
39. Willnow, T. E., Petersen, C. M. & Nykjaer, A. VPS10P-domain receptors — regulators of neuronal viability and function. *Nature Reviews Neuroscience* **9**, 899–909 (2008).
40. Vaegter, C. B., Jansen, P., Fjorback, A. W., Glerup, S., Skeldal, S., Kjolby, M., Richner, M., Erdmann, B., Nyengaard, J. R., Tessarollo, L., Lewin, G. R., Willnow, T. E., Chao, M. v & Nykjaer, A. Sortilin associates with Trk receptors to enhance anterograde transport and neurotrophin signaling. *Nature Neuroscience* **14**, 54–61 (2011).
41. Chen, Z. Y., Ieraci, A., Teng, H., Dall, H., Meng, C. X., Herrera, D. G., Nykjaer, A., Hempstead, B. L. & Lee, F. S. Sortilin Controls Intracellular Sorting of Brain-Derived Neurotrophic Factor to the Regulated Secretory Pathway. *Journal of Neuroscience* **25**, 6156–6166 (2005).

42. Glerup, S., Olsen, D., Vaegter, C. B., Gustafsen, C., Sjoegaard, S. S., Hermey, G., Kjolby, M., Molgaard, S., Ulrichsen, M., Boggild, S., Skeldal, S., Fjorback, A. N., Nyengaard, J. R., Jacobsen, J., Bender, D., Bjarkam, C. R., Sørensen, E. S., Füchtbauer, E. M., Eichele, G., Madsen, P., Willnow, T. E., Petersen, C. M. & Nykjaer, A. SorCS2 Regulates Dopaminergic Wiring and Is Processed into an Apoptotic Two-Chain Receptor in Peripheral Glia. *Neuron* **82**, 1074–1087 (2014).
43. Yang, J., Ma, Q., Dincheva, I., Giza, J., Jing, D., Marinic, T., Milner, T. A., Rajadhyaksha, A., Lee, F. S. & Hempstead, B. L. SorCS2 is required for social memory and trafficking of the NMDA receptor. *Molecular Psychiatry* **26**, 927–940 (2021).
44. Malik, A. R., Szydlowska, K., Nizinska, K., Asaro, A., van Vliet, E. A., Popp, O., Dittmar, G., Fritsche-Guenther, R., Kirwan, J. A., Nykjaer, A., Lukasiuk, K., Aronica, E. & Willnow, T. E. SorCS2 Controls Functional Expression of Amino Acid Transporter EAAT3 and Protects Neurons from Oxidative Stress and Epilepsy-Induced Pathology. *Cell Reports* **26**, 2792-2804.e6 (2019).
45. Larsen, J. V. & Petersen, C. M. SorLA in Interleukin-6 Signaling and Turnover. *Molecular and Cellular Biology* **37**, e00641-16 (2017).
46. Kuffner, M., Koch, S. P., Kirchner, M., Mueller, S., Lips, J., An, J., Mertins, P., Dirnagl, U., Endres, M., Boehm-Sturm, P., Harms, C. & Hoffmann, C. J. Paracrine Interleukin 6 Induces Cerebral Remodeling at Early Stages After Unilateral Common Carotid Artery Occlusion in Mice. *Front Cardiovasc Med* **8**, (2022).
47. Mei, J., Banneke, S., Lips, J., Kuffner, M. T. C., Hoffmann, C. J., Dirnagl, U., Endres, M., Harms, C. & Emmrich, J. V. Refining humane endpoints in mouse models of disease by systematic review and machine learning-based endpoint definition. *Altex* **36**, (2019).
48. Dirnagl, U. & Group, M. of the M.-S. Standard operating procedures (SOP) in experimental stroke research: SOP for middle cerebral artery occlusion in the mouse. *Nature Precedings* (2010) doi:10.1038/npre.2010.3492.2.
49. Holm, H., Nägga, K., Nilsson, E. D., Ricci, F., Melander, O., Hansson, O., Bachus, E., Fedorowski, A. & Magnusson, M. High circulating levels of midregional proenkephalin A predict vascular dementia: a population-based prospective study. *Sci Rep* **10**, 8027 (2020).
50. Brás, I. C., Dominguez-Meijide, A., Gerhardt, E., Koss, D., Lázaro, D. F., Santos, P. I., Vasili, E., Xylaki, M. & Outeiro, T. F. Synucleinopathies: Where we are and where we need to go. *J Neurochem* **153**, 433–454 (2020).

51. Nakayama, K., Ohashi, R., Shinoda, Y., Yamazaki, M., Abe, M., Fujikawa, A., Shigenobu, S., Futatsugi, A., Noda, M., Mikoshiba, K., Furuichi, T., Sakimura, K. & Shiina, N. RNG105/caprin1, an RNA granule protein for dendritic mRNA localization, is essential for long-term memory formation. *Elife* **6**, e29677 (2017).
52. Munton, R. P., Vizi, S. & Mansuy, I. M. The role of protein phosphatase-1 in the modulation of synaptic and structural plasticity. *FEBS Lett* **567**, 121–128 (2004).
53. Malik, A. R., Lips, J., Gorniak-Walas, M., Broekaart, D. W. M., Asaro, A., Kuffner, M. T. C., Hoffmann, C. J., Kikhia, M., Dopatka, M., Boehm-Sturm, P., Mueller, S., Dirnagl, U., Aronica, E., Harms, C. & Willnow, T. E. SorCS2 facilitates release of endostatin from astrocytes and controls post-stroke angiogenesis. *GLIA* **68**, (2020).
54. Pardali, E., Goumans, M. J. & ten Dijke, P. Signaling by members of the TGF-β family in vascular morphogenesis and disease. *Trends in Cell Biology* **20**, 556–567 (2010).
55. Meng, H., Song, Y., Zhu, J., Liu, Q., Lu, P., Ye, N., Zhang, Z., Pang, Y., Qi, J. & Wu, H. LRG1 promotes angiogenesis through upregulating the TGF-β1 pathway in ischemic rat brain. *Molecular Medicine Reports* **14**, 5535–5543 (2016).
56. Yan, J., Greer, J. M. & McCombe, P. A. Prolonged elevation of cytokine levels after human acute ischaemic stroke with evidence of individual variability. *Journal of Neuroimmunology* **246**, 78–84 (2012).
57. Zhang, C., Zhu, Y., Wang, S., Wei, Z. Z., Jiang, M. Q., Zhang, Y., Pan, Y., Tao, S., Li, J. & Wei, L. Temporal gene expression profiles after focal cerebral ischemia in mice. *Aging and Disease* **9**, 249–261 (2018).
58. Chen, N., Gao, R. F., Yuan, F. L. & Zhao, M. D. Recombinant human endostatin suppresses mouse osteoclast formation by inhibiting the NF-κB and MAPKs signaling pathways. *Frontiers in Pharmacology* **7**, 145 (2016).
59. Sudhakar, A., Sugimoto, H., Yang, C., Lively, J., Zeisberg, M. & Kalluri, R. Human tumstatin and human endostatin exhibit distinct antiangiogenic activities mediated by αvβ3 and α5β1 integrins. *Proceedings of the National Academy of Sciences* **100**, 4766–4771 (2003).
60. Benarroch, E. E. Periaqueductal gray: an interface for behavioral control. *Neurology* **78**, 210–217 (2012).
61. Solomon, S., Xu, Y., Wang, B., David, M. D., Schubert, P., Kennedy, D. & Schrader, J. W. Distinct Structural Features of Caprin-1 Mediate Its Interaction with G3BP-1 and Its Induction of Phosphorylation of Eukaryotic Translation Initiation Factor 2α,

Entry to Cytoplasmic Stress Granules, and Selective Interaction with a Subset of mRNAs. *Molecular and Cellular Biology* **27**, 2324–2342 (2007).

62. Borden, L. A. & Caplan, M. J. GABA transporter heterogeneity: Pharmacology and cellular localization. *Neurochemistry International* **29**, 335–356 (1996).
63. van Nuland, A. J. M., den Ouden, H. E. M., Zach, H., Dirkx, M. F. M., van Asten, J. J. A., Scheenen, T. W. J., Toni, I., Cools, R. & Helmich, R. C. GABAergic changes in the thalamocortical circuit in Parkinson's disease. *Human Brain Mapping* **41**, 1017 (2020).
64. Watanabe, M., Maemura, K., Kanbara, K., Tamayama, T. & Hayasaki, H. GABA and GABA receptors in the central nervous system and other organs. *Int Rev Cytol* **213**, 1–47 (2002).
65. Shi, J., Cai, Y., Liu, G., Gong, N., Liu, Z., Xu, T., Wang, Z. & Fei, J. Enhanced learning and memory in GAT1 heterozygous mice. *Acta Biochim Biophys Sin (Shanghai)* **44**, 359–366 (2012).
66. Yang, P., Cai, G., Cai, Y., Fei, J. & Liu, G. Gamma aminobutyric acid transporter subtype 1 gene knockout mice: a new model for attention deficit/hyperactivity disorder. *Acta Biochim Biophys Sin (Shanghai)* **45**, 578–585 (2013).
67. Äikiä, M., Jutila, L., Salmenperä, T., Mervaala, E. & Kälviäinen, R. Comparison of the cognitive effects of tiagabine and carbamazepine as monotherapy in newly diagnosed adult patients with partial epilepsy: pooled analysis of two long-term, randomized, follow-up studies. *Epilepsia* **47**, 1121–1127 (2006).
68. Lie, M. E. K., Gowing, E. K., Clausen, R. P., Wellendorph, P. & Clarkson, A. N. Inhibition of GABA transporters fails to afford significant protection following focal cerebral ischemia. *J Cereb Blood Flow Metab* **38**, 166–173 (2018).
69. Yang, Y., Li, Q., Wang, C. X., Jeerakathil, T. & Shuaib, A. Dose-dependent neuroprotection with tiagabine in a focal cerebral ischemia model in rat. *Neuroreport* **11**, 2307–2311 (2000).
70. García-Bermúdez, J. & Cuezva, J. M. The ATPase Inhibitory Factor 1 (IF1): A master regulator of energy metabolism and of cell survival. *Biochim Biophys Acta* **1857**, 1167–1182 (2016).
71. Chen, Y., Sun, J. X., Chen, W. K., Wu, G. C., Wang, Y. Q., Zhu, K. Y. & Wang, J. miR-124/VAMP3 is a novel therapeutic target for mitigation of surgical trauma-induced microglial activation. *Signal Transduct Target Ther* **4**, 27 (2019).

72. Yang, Y. & Torbey, M. T. Angiogenesis and Blood-Brain Barrier Permeability in Vascular Remodeling after Stroke. *Current Neuropharmacology* **18**, 1250 (2020).
73. Hayashi, T., Noshita, N., Sugawara, T. & Chan, P. H. Temporal profile of angiogenesis and expression of related genes in the brain after ischemia. *J Cereb Blood Flow Metab* **23**, 166–180 (2003).
74. Zhang, Z. G., Zhang, L., Jiang, Q., Zhang, R., Davies, K., Powers, C., Van Bruggen, N. & Chopp, M. VEGF enhances angiogenesis and promotes blood-brain barrier leakage in the ischemic brain. *Journal of Clinical Investigation* **106**, 829 (2000).
75. Yoshizaki, K., Adachi, K., Kataoka, S., Watanabe, A., Tabira, T., Takahashi, K. & Wakita, H. Chronic cerebral hypoperfusion induced by right unilateral common carotid artery occlusion causes delayed white matter lesions and cognitive impairment in adult mice. *Experimental Neurology* **210**, 585–591 (2008).
76. Mansour, A., Niizuma, K., Rashad, S., Sumiyoshi, A., Ryoke, R., Endo, H., Endo, T., Sato, K., Kawashima, R. & Tominaga, T. A refined model of chronic cerebral hypoperfusion resulting in cognitive impairment and a low mortality rate in rats. *Journal of Neurosurgery* **131**, 892–902 (2019).
77. Fuller, H. R., Slade, R., Jovanov-Milošević, N., Babić, M., Sedmak, G., Šimić, G., Fuszard, M. A., Shirran, S. L., Botting, C. H. & Gates, M. A. Stathmin is enriched in the developing corticospinal tract. *Molecular and Cellular Neuroscience* **69**, 12–21 (2015).
78. Zhu, Y., Dou, M., Piehowski, P. D., Liang, Y., Wang, F., Chu, R. K., Chrisler, W. B., Smith, J. N., Schwarz, K. C., Shen, Y., Shukla, A. K., Moore, R. J., Smith, R. D., Qian, W. J. & Kelly, R. T. Spatially resolved proteome mapping of laser capture microdissected tissue with automated sample transfer to nanodroplets. *Molecular and Cellular Proteomics* **17**, 1864–1874 (2018).

Statutory Declaration

“I, Melanie Tamara Carolin Kuffner, by personally signing this document in lieu of an oath, hereby affirm that I prepared the submitted dissertation on the topic “Adaptations- und Rekonstruktionsmechanismen im hypoperfundierten Gehirn - Mechanisms of adaptation and reconstruction in the hypoperfused brain”, independently and without the support of third parties, and that I used no other sources and aids than those stated.
All parts which are based on the publications or presentations of other authors, either in letter or in spirit, are specified as such in accordance with the citing guidelines. The sections on methodology (in particular regarding practical work, laboratory regulations, statistical processing) and results (in particular regarding figures, charts and tables) are exclusively my responsibility.

Furthermore, I declare that I have correctly marked all of the data, the analyses, and the conclusions generated from data obtained in collaboration with other persons, and that I have correctly marked my own contribution and the contributions of other persons (cf. declaration of contribution). I have correctly marked all texts or parts of texts that were generated in collaboration with other persons.

My contributions to any publications to this dissertation correspond to those stated in the below joint declaration made together with the supervisor. All publications created within the scope of the dissertation comply with the guidelines of the ICMJE (International Committee of Medical Journal Editors; http://www.icmje.org) on authorship. In addition, I declare that I shall comply with the regulations of Charité – Universitätsmedizin Berlin on ensuring good scientific practice.

I declare that I have not yet submitted this dissertation in identical or similar form to another Faculty.

The significance of this statutory declaration and the consequences of a false statutory declaration under criminal law (Sections 156, 161 of the German Criminal Code) are known to me.”

Date Signature

Declaration of your own contribution to the publications

Melanie Tamara Carolin Kuffner contributed the following to the below listed publications:

Publication 1:
Kuffner MTC, Koch SP, Kirchner M, Mueller S, Lips J, An J, Mertins P, Harms C, Dirnagl U, Endres M, Boehm-Sturm P, Hoffmann CJ, Paracrine Interleukin 6 induces cerebral remodeling at early stages after unilateral common carotid artery occlusion in mice, *Frontiers in Cardiovascular Medicine*, 2022

Contribution:
Partly designed the study; responsible for breeding and partly genotyping the mice in collaboration with Lips J; executed mRNA preparation and IL-6 level determination by molecular assays (Figure 1A-F); partly performed behavioral experiments in collaboration with Lips J, and Foddis M and Dopatka M, who also performed the CCAo surgeries (Fig. 2 C-F); performed MRI measurement on day 2 (Fig 2B). DTI measurements on day 21 were performed by Mueller S and DTI results were analyzed by Koch SP, An J, and Boehm-Sturm P.
Executed and analyzed histological stainings; performed manual and automated cell quantifications (Fig. 3); performed laser capture microdissection for proteome analysis by mass spectrometry (Fig. 4C and 5B). Spectrometry and statistical analysis of proteome data was carried out by Kirchner M with Mertins P.
Wrote the manuscript and lead iterative improvements with contribution of Böhm-Sturm P, Endres M, Dirnagl U, Harms C and Hoffmann CJ. Analyzed the data, and conducted statistical analysis under supervision of Hoffmann CJ and Harms C.

Publication 2:
Malik AR, Lips J, Gorniak-Walas M, Broekaart DWM, Asaro A, **Kuffner MTC**, Hoffmann CJ, Kikhia M, Dopatka M, Boehm-Sturm P, Mueller S, Dirnagl U, Aronica E, Harms C, Willnow TE. SorCS2 facilitates release of endostatin from astrocytes and controls post-stroke angiogenesis. *Glia*. 2020 Jun;68(6):1304-1316. doi: 10.1002/glia.23778.

Contribution:
Partly executed animal work and immunohistochemistry in collaboration with Lips J, Kikhia M, and Dopatka M (Fig. 1A – C, 3A); revised the manuscript.

Publication 3:
Mei J, Banneke S, Lips J, **Kuffner MTC**, Hoffmann CJ, Dirnagl U, Endres M, Harms C, Emmrich JV. Refining humane endpoints in mouse models of disease by systematic review and machine learning-based endpoint definition. *ALTEX*. 2019;36(4):555-571. doi: 10.14573/altex.1812231.

Contribution:
Curated and prepared stroke animal data for analysis, unified data acquisition, and conceptualized a database for secondary analysis (Tab. 3A); reviewed algorithm strategies (Fig. 2B,D) in collaboration with Lips J, Hoffmann CJ, Harms C, and Mei J; revised the manuscript.

_____

Signature, date and stamp of first supervising university professor / lecturer

_____

Signature of doctoral candidate

Excerpts from Journal Summary List

Journal Data Filtered By: **Selected JCR Year: 2020** Selected Editions: SCIE,SSCI Selected Categories: **"CARDIAC and CARDIOVASCULAR SYSTEMS"** Selected Category Scheme: WoS

Gesamtanzahl: 141 Journale

Rank	Full Journal Title	Total Cites	Journal Impact Factor	Eigenfactor Score
1	Nature Reviews Cardiology	11,539	32.419	0.022990
2	EUROPEAN HEART JOURNAL	81,447	29.983	0.141060
3	CIRCULATION	190,210	29.690	0.200030
4	JOURNAL OF THE AMERICAN COLLEGE OF CARDIOLOGY	125,873	24.094	0.177000
5	CIRCULATION RESEARCH	65,425	17.367	0.068900
6	BASIC RESEARCH IN CARDIOLOGY	5,629	17.165	0.005290
7	EUROPEAN JOURNAL OF HEART FAILURE	17,114	15.534	0.027740
8	JACC-Cardiovascular Imaging	14,398	14.805	0.032190
9	JAMA Cardiology	11,453	14.676	0.036150
10	JACC-Heart Failure	6,212	12.035	0.019320
11	JACC-Cardiovascular Interventions	15,448	11.195	0.035240
12	CARDIOVASCULAR RESEARCH	26,765	10.787	0.019070
13	JOURNAL OF HEART AND LUNG TRANSPLANTATION	15,107	10.247	0.021660
14	Cardiovascular Diabetology	8,782	9.951	0.012280
15	Circulation-Heart Failure	9,005	8.790	0.016490
16	JACC-Basic to Translational Science	1,842	8.648	0.005140
17	PROGRESS IN CARDIOVASCULAR DISEASES	5,799	8.194	0.006870
18	European Journal of Preventive Cardiology	8,287	7.804	0.014250
19	Circulation-Cardiovascular Imaging	7,640	7.792	0.015510
20	European Heart Journal-Cardiovascular Imaging	8,423	6.875	0.020790

Rank	Full Journal Title	Total Cites	Journal Impact Factor	Eigenfactor Score
21	TRENDS IN CARDIOVASCULAR MEDICINE	3,542	6.677	0.004230
22	European Heart Journal-Cardiovascular Pharmacotherapy	919	6.617	0.002480
23	Circulation-Arrhythmia and Electrophysiology	8,834	6.568	0.015230
24	Circulation-Cardiovascular Interventions	6,530	6.546	0.014270
25	EuroIntervention	7,160	6.534	0.014970
26	JACC-Clinical Electrophysiology	2,801	6.375	0.009790
27	HEART RHYTHM	16,459	6.343	0.025740
28	JACC: CardioOncology	267	6.250	0.000230
29	Circulation-Genomic and Precision Medicine	858	6.054	0.003910
30	Frontiers in Cardiovascular Medicine	3,172	6.050	0.007630
31	HEART	22,182	5.994	0.028490
32	JOURNAL OF NUCLEAR CARDIOLOGY	5,882	5.952	0.005390
33	Circulation-Cardiovascular Quality and Outcomes	6,318	5.882	0.013260
34	JOURNAL OF CARDIAC FAILURE	6,604	5.712	0.008690
35	Journal of the American Heart Association	26,960	5.501	0.075700
36	Clinical Research in Cardiology	5,218	5.460	0.007940
37	JOURNAL OF CARDIOVASCULAR MAGNETIC RESONANCE	6,935	5.364	0.010460
38	JOURNAL OF THE AMERICAN SOCIETY OF ECHOCARDIOGRAPHY	14,150	5.251	0.018650
39	CANADIAN JOURNAL OF CARDIOLOGY	8,782	5.223	0.015090
40	EUROPACE	12,468	5.214	0.021850

Selected JCR Year: 2020; Selected Categories: "CARDIAC and CARDIOVASCULAR SYSTEMS"

Journal Data Filtered By: **Selected JCR Year: 2018** Selected Editions: SCIE,SSCI
Selected Categories: **"NEUROSCIENCES"** Selected Category Scheme: WoS
Gesamtanzahl: 267 Journale

Rank	Full Journal Title	Total Cites	Journal Impact Factor	Eigenfactor Score
1	NATURE REVIEWS NEUROSCIENCE	43,107	33.162	0.068480
2	NATURE NEUROSCIENCE	63,390	21.126	0.164700
3	ACTA NEUROPATHOLOGICA	20,206	18.174	0.041660
4	BEHAVIORAL AND BRAIN SCIENCES	9,377	17.194	0.010240
5	TRENDS IN COGNITIVE SCIENCES	27,095	16.173	0.040040
6	JOURNAL OF PINEAL RESEARCH	10,695	15.221	0.010560
7	NEURON	95,348	14.403	0.218680
8	TRENDS IN NEUROSCIENCES	20,163	12.314	0.024480
9	Annual Review of Neuroscience	14,042	12.043	0.015020
10	MOLECULAR PSYCHIATRY	20,353	11.973	0.049290
11	BRAIN	52,970	11.814	0.074030
12	BIOLOGICAL PSYCHIATRY	43,122	11.501	0.053320
13	PROGRESS IN NEUROBIOLOGY	12,929	10.658	0.013230
14	Nature Human Behaviour	1,230	10.575	0.006550
15	SLEEP MEDICINE REVIEWS	6,920	10.517	0.010920
16	ANNALS OF NEUROLOGY	37,336	9.496	0.048630
17	Molecular Neurodegeneration	4,248	8.274	0.011350
18	NEUROSCIENCE AND BIOBEHAVIORAL REVIEWS	26,724	8.002	0.051580
19	FRONTIERS IN NEUROENDOCRINOLOGY	4,196	7.852	0.005490
20	Neurology-Neuroimmunology & Neuroinflammation	1,996	7.353	0.008220
21	NEUROPSYCHOPHARMACOLOGY	25,672	7.160	0.039090

Rank	Full Journal Title	Total Cites	Journal Impact Factor	Eigenfactor Score
22	Brain Stimulation	5,457	6.919	0.014470
23	NEUROPATHOLOGY AND APPLIED NEUROBIOLOGY	3,876	6.878	0.006420
24	NEUROENDOCRINOLOGY	5,046	6.804	0.005690
25	NEUROSCIENTIST	4,986	6.791	0.008520
26	BRAIN BEHAVIOR AND IMMUNITY	14,533	6.170	0.025700
27	BRAIN PATHOLOGY	5,263	6.155	0.007880
28	Alzheimers Research & Therapy	3,160	6.142	0.010700
29	JOURNAL OF NEUROSCIENCE	175,046	6.074	0.233460
30	JOURNAL OF CEREBRAL BLOOD FLOW AND METABOLISM	19,766	6.040	0.028050
31	PAIN	38,312	6.029	0.039070
32	CURRENT OPINION IN NEUROBIOLOGY	15,090	6.014	0.033650
33	Acta Neuropathologica Communications	3,063	5.883	0.014190
34	Translational Stroke Research	1,955	5.847	0.004330
35	GLIA	14,003	5.829	0.018760
36	NEUROIMAGE	99,720	5.812	0.132720
37	NEURAL NETWORKS	13,063	5.785	0.016060
38	NEUROPSYCHOLOGY REVIEW	2,971	5.739	0.003940
39	Molecular Autism	2,107	5.712	0.008000
40	Journal of Neuroinflammation	11,767	5.700	0.023240
41	Multiple Sclerosis Journal	11,501	5.649	0.022750
42	Annual Review of Vision Science	458	5.622	0.003300
43	Neurotherapeutics	4,475	5.552	0.009060
44	Translational Neurodegeneration	810	5.534	0.002420

Selected JCR Year: 2018; Selected Categories: "NEUROSCIENCES"

Journal Data Filtered By: **Selected JCR Year: 2018** Selected Editions: SCIE,SSCI
Selected Categories: **"MEDICINE, RESEARCH and EXPERIMENTAL"**
Selected Category Scheme: WoS
Gesamtanzahl: 136 Journale

Rank	Full Journal Title	Total Cites	Journal Impact Factor	Eigenfactor Score
1	NATURE MEDICINE	79,243	30.641	0.162840
2	Science Translational Medicine	30,485	17.161	0.121980
3	JOURNAL OF CLINICAL INVESTIGATION	108,879	12.282	0.139970
4	TRENDS IN MOLECULAR MEDICINE	9,946	11.028	0.018900
5	JOURNAL OF EXPERIMENTAL MEDICINE	63,983	10.892	0.071790
6	EMBO Molecular Medicine	7,507	10.624	0.025980
7	Annual Review of Medicine	6,068	10.091	0.009030
8	MOLECULAR THERAPY	16,991	8.402	0.030050
9	MOLECULAR ASPECTS OF MEDICINE	5,568	8.313	0.009020
10	Theranostics	8,769	8.063	0.020270
11	EBioMedicine	5,401	6.680	0.022310
12	ALTEX-Alternatives to Animal Experimentation	1,361	6.183	0.001920
13	Wiley Interdisciplinary Reviews-Nanomedicine and Nanobiotechnology	2,345	6.140	0.004130
14	JCI Insight	4,351	6.014	0.020440
15	Molecular Therapy-Nucleic Acids	3,189	5.919	0.010410
16	Molecular Therapy-Oncolytics	486	5.710	0.001990
17	Nanomedicine-Nanotechnology Biology and Medicine	10,131	5.570	0.014480
18	Cold Spring Harbor Perspectives in Medicine	6,223	5.564	0.016730
19	CLINICAL SCIENCE	10,951	5.237	0.014190
20	JOURNAL OF BIOMEDICAL SCIENCE	4,083	5.203	0.006300

Printing copies of the publications

frontiers in Cardiovascular Medicine

ORIGINAL RESEARCH
published: 27 January 2022
doi: 10.3389/fcvm.2021.805095

Paracrine Interleukin 6 Induces Cerebral Remodeling at Early Stages After Unilateral Common Carotid Artery Occlusion in Mice

Melanie T. C. Kuffner[1], Stefan P. Koch[1,2,3], Marieluise Kirchner[4], Susanne Mueller[1,2,3], Janet Lips[1], Jeehye An[1,2,3], Philipp Mertins[4], Ulrich Dirnagl[1,2,5,6,7,8,9], Matthias Endres[1,2,5,6,7,8], Philipp Boehm-Sturm[1,2,3], Christoph Harms[1,2,5,8] and Christian J. Hoffmann[1,2]**

[1] Klinik und Hochschulambulanz für Neurologie mit Experimenteller Neurologie, Charité-Universitätsmedizin Berlin, Freie Universität Berlin, Humboldt-Universität zu Berlin, Berlin Institute of Health, Berlin, Germany, [2] Center for Stroke Research Berlin, Charité-Universitätsmedizin Berlin, Berlin, Germany, [3] NeuroCure Cluster of Excellence and Charité Core Facility 7T Experimental MRIs, Charité-Universitätsmedizin Berlin, Berlin, Germany, [4] Core Unit Proteomics, Berlin Institute of Health at Charité- Universitätsmedizin Berlin, Max Delbrück Center for Molecular Medicine, Berlin, Germany, [5] German Center for Cardiovascular Research (DZHK), Partner Site Berlin, Berlin, Germany, [6] NeuroCure Clinical Research Center, Charité-Universitätsmedizin Berlin, Berlin, Germany, [7] German Center for Neurodegenerative Diseases (DZNE), Partner Site Berlin, Berlin, Germany, [8] Einstein Center for Neuroscience, Berlin, Germany, [9] QUEST Quality, Ethics, Open Science, Translation, Center for Transforming Biomedical Research, Berlin Institute of Health, Berlin, Germany

OPEN ACCESS

Edited by:
Yoshihiko Kakinuma, Nippon Medical School, Japan

Reviewed by:
Antonio Colantuoni, University of Naples Federico II, Italy
Bisheng Zhou, University of Illinois at Chicago, United States
Valentina Casieri, Scuola Sant'Anna di Studi Avanzati, Italy

***Correspondence:**
Christian J. Hoffmann
christian.hoffmann@charite.de
Christoph Harms
christoph.harms@charite.de

Specialty section:
This article was submitted to Cardiovascular Biologics and Regenerative Medicine, a section of the journal Frontiers in Cardiovascular Medicine

Received: *29 October 2021*
Accepted: *20 December 2021*
Published: *27 January 2022*

Citation:
Kuffner MTC, Koch SP, Kirchner M, Mueller S, Lips J, An J, Mertins P, Dirnagl U, Endres M, Boehm-Sturm P, Harms C and Hoffmann CJ (2022) Paracrine Interleukin 6 Induces Cerebral Remodeling at Early Stages After Unilateral Common Carotid Artery Occlusion in Mice. Front. Cardiovasc. Med. 8:805095. doi: 10.3389/fcvm.2021.805095

Aims: Carotid artery disease is frequent and can result in chronic modest hypoperfusion of the brain. If no transient ischemic attack or stroke occur, it is classified asymptomatic. In the long-term, though, it can lead to cognitive impairment. Fostering cerebral remodeling after carotid artery occlusion might be a new concept of treatment. Paracrine Interleukin 6 (IL-6) can induce such remodeling processes at early stages. However, it has neurodegenerative long-term effects. With this exploratory study, we investigated the effect of paracrine IL-6 on cerebral remodeling in early stages after asymptomatic carotid artery occlusion to identify new treatment targets.

Methods and Results: To mimic a human asymptomatic carotid artery disease, we used a mouse model of unilateral common carotid artery (CCA) occlusion. We developed a mouse model for inducible paracrine cerebral IL-6 expression (Cx30-Cre-ERT2;FLEX-IL6) and induced IL-6 2 days after CCA occlusion. We studied the effects of paracrine IL-6 after CCA occlusion on neuronal connectivity using diffusion tensor imaging and on local proteome regulations of the hypo-perfused striatum and contralateral motor cortex using mass spectrometry of laser capture micro-dissected tissues. Paracrine IL-6 induced cerebral remodeling leading to increased inter-hemispheric connectivity and changes in motor system connectivity. We identified changes in local protein abundance which might have adverse effects on functional outcome such as upregulation of Synuclein gamma (Sncg) or downregulation of Proline Dehydrogenase 1 (Prodh). However, we also identified changes in local protein abundance having potentially beneficial effects such as upregulation of Caprin1 or downregulation of GABA transporter 1 (Gat1).

Conclusions: Paracrine cerebral IL-6 at early stages induces changes in motor system connectivity and the proteome after asymptomatic CCA occlusion. Our results may help to distinguish unfavorable from beneficial IL-6 dependent protein regulations. Focusing on these targets might generate new treatments to improve long-term outcome in patients with carotid artery disease.

Keywords: vascular disease, basic science research, proteomics, inflammation, carotid artery occlusion

INTRODUCTION

Carotid artery disease is highly prevalent in an aged population (1). It may lead to carotid artery stenosis or occlusion, causing chronic hypoperfusion of the brain and increasing the risk for cerebral infarction (2). In the long-term, carotid artery disease can cause white matter damage. When no transient ischemic attack or stroke occur it is classified asymptomatic. However, about 50% of these patients with asymptomatic carotid stenosis show signs of neuropsychological deficits such as reduced processing speed and learning (3).

Fostering cerebral remodeling after carotid artery occlusion might be a new concept of treatment to improve the long-term outcome. We have shown that the cytokine interleukin 6 (IL-6) is essential for post-ischemic angiogenesis and improves the outcome after stroke (4). Down-stream signaling of IL-6 in endothelial cells is needed to induce changes in the extracellular matrix and the molecular micro-environment fostering neuroplasticity and functional recovery (5). It has been shown that IL-6 improves repair after trauma (6). However, long-term elevated IL-6 is associated with cognitive decline (7). Indeed, the effects of IL-6 are complex and depend on its temporal (acute vs. long-term) and spatial (paracrine vs. systemic) expression.

We hypothesize that—comparable to its effects after stroke—paracrine IL-6 might induce beneficial remodeling processes in the acute phase after modest cerebral hypoperfusion induced by carotid artery disease while it might have detrimental effects in the long-term. Therefore, the aim of this exploratory study was to analyze early-stage cerebral remodeling mechanisms of paracrine brain-specific IL-6 within the first 3 weeks of modest chronic cerebral hypoperfusion. We used the mouse model of unilateral common carotid artery (CCA) occlusion to mimic an asymptomatic carotid artery stenosis in humans. In this mouse model, long-lasting modest hypoperfusion of the brain has been verified without the development of strokes or motor function deficits (8, 9). Comparable to humans, unilateral CCA stenosis induced neuropsychological deficits in mice primarily affecting learning. A prolonged increase of cerebral astrocytic IL-6 has been shown to cause neuroinflammation and neurodegeneration within a period of 3–24 month using a constitutive GFAP-IL6 mouse model and this effect depended on the heights of IL-6 expression (10–12). We developed a genetically modified mouse model for inducible brain-specific paracrine secretion of IL-6 to avoid this biasing effect before CCA occlusion. Using this mouse model, we studied the effects of a slight paracrine IL-6 increase on connectivity changes and local proteome changes.

With this study, we show that paracrine IL-6 induces adaptations in the motor system connectivity. In the proteome, we could differentiate proteins that might improve functional and cognitive outcome from proteins with unfavorable effects. By this, our results might help to identify molecular targets for new treatments of asymptomatic CCA occlusion.

METHODS

Animals

All experimental procedures were approved by the local authorities (Landesamt für Gesundheit und Soziales, LaGeSo), Berlin (Reg G0119/16) and were conducted following the German animal protection law and local animal welfare guidelines. Mice were group-housed with *ad libitum* access to water. Food was restricted as a motivator for functional testing. Housing conditions and details are described in **Supplementary Material**.

We genetically engineered a mouse model by inducing a flip and excision (FLEX) cassette into the ROSA26 locus using recombinase-mediated cassette exchange containing an inverted IL-6 followed by a T2A self-cleavage sequence and mKate2. IL-6 was fused to a C-terminal myc-tag (EQKLISEEDL) via a spacer (GGSGGTGGS). Mice were crossbred with astrocyte-specific Cx30-Cre-ERT2 mice. The mice are bred locally on a C57BL/6J background and were backcrossed for 10 generations. We used mice for experiments that were hemizygous for Cx30-Cre-ERT2 and hemizygous for FLEX-IL-6. Mice that were hemizygous for FLEX-IL-6 served as control animals. The mice were at an age of 10–12 weeks. In total, 66 mice were used for the experiments. Of these mice, 64 mice were analyzed according to the preset exclusion criteria (see methods to prevent bias and exclusion criteria), and further 2 mice were excluded for technical reasons as specified in the section Results. Mouse groups were age- and sex-matched for experimental and control groups.

For surgery, mice were anesthetized with 1.5–3.5% Isoflurane and maintained in 1.0–2.5% Isoflurane with ~75/25 N_2O/O_2 and for pain relief, bupivacain gel (1%) was topically applied to the wound. For MRI, anesthesia was induced with 2.5% and maintained with 2.0–1.5% isoflurane (Forene, Abbot, Wiesbaden, Germany) delivered in a O_2/N_2O mixture (0.3/0.7 l/min) via a facemask under constant ventilation monitoring (Small Animal Monitoring & Gating System, SA Instruments, Stony Brook, New York, USA). Mice were euthanized in deep anesthesia with 100 µl Ketamine/Xylazine [0.7% Ketamine (10%, cb pharma), 0.8% Xylazine (20 mg/ml Xylavet, cb pharma)] per 10 g body

weight given i.p. and cardially perfused with 0.9% physiological NaCl solution.

Western Blot and Enzyme-Linked Immunosorbent Assay

IL-6 was semi-quantitatively analyzed by ELISA in serum samples and deep-frozen mouse brain sections as described in the **Supplementary Material**.

Cell Culture, Transfection, and Real-Time RT-PCR

HEK 293T cells were transfected with plasmids coding for FLEX-IL-6, Cre-GFP fusion or both. Brain microvascular endothelial cells were treated with conditioned medium of these cultures for 1 h prior quantification of IL-6 mRNA and a reference transcript as described in detail in **Supplementary Material**.

Mouse Surgery and Tamoxifen Injection

Mice were subjected to unilateral ligation of the left common carotid artery. Following the 3R principle of animal experiment reduction, mice with unilateral CCA occlusion served additionally as sham control for a transient occlusion of the middle cerebral artery (MCAO). In brief, surgery was performed analogously to the sham operation as established in our lab and described in detail in **Supplementary Material**, and tamoxifen was injected intraperitoneal on day two after surgery as a single dose or on three consecutive days (1 mg tamoxifen; Sigma, 10 mg/ml in 1:10 ethanol/corn oil).

Behavioral Tests

Sickness behavior was assessed by modified DeSimoni's neuroscore at days 2, 7, 14, and 21 following unilateral CCA occlusion. The maximum score is 43 points, where a higher score indicates more deficits. Rotarod test was performed with three runs per trial with a recovery time of 30 min between trials. Shown is the average performance. Tests were performed on days 2, 7, and 14 after unilateral CCAo. Staircase skilled pellet reaching test was performed daily for 21 days of training before and up to 21 days after ligation of the CCA for conditioning as described previously (13). Outcome was measured as relative performance compared to the individual performance before surgery for each forepaw.

Magnetic Resonance Imaging

Mice were examined 24 h after the onset of CCA using T2-weighted imaging. After 21 days, T2-weighted and diffusion tensor imaging (DTI) were performed as outlined in detail in **Supplementary Material**. Briefly, a custom brain atlas with 308 anatomical regions (154 right/154 left hemisphere) derived from the Allen mouse brain atlas was registered to the T2-weighted and diffusion MR images using ANTx2 (https://github.com/ChariteExpMri/antx2). DTI can measure the directionality of water diffusion in tissue, which is a proxy of the orientation of nerve fiber tracts in the respective voxel. Using computational models that take into account the orientation of water diffusion in all voxels in gray and white matter, long range fiber connections from one atlas region to another region can therefore be reconstructed. The number of reconstructed tracts is a measure of connectivity strength. From the DTI scan, a matrix of all possible combinations of those connections and their strength (termed DTI connectome) for each animal was calculated in mrtrix (https://www.mrtrix.org, shell scripts available at https://github.com/ChariteExpMri/rodentDtiConnectomics). Between group comparisons were carried out on the number of reconstructed streamlines between pairs of regions.

Proteomic Analysis of Laser Capture Microscopy Samples by Mass Spectrometry

Briefly, left hemispheric ipsilateral fiber tracts in the striatum or the contralateral motor cortex were laser-captured 5 days after CCA occlusion and 3 days after i.p. injection of tamoxifen from frozen tissue sections and subjected to mass spectrometry and analysis as described in Jochner et al. (14) and in detail in **Supplementary Material**.

Histology and Imaging Analysis

Briefly, mice were euthanized in deep anesthesia, blood was collected from the Vena cava after abdominal incision, and mice were cardially perfused with 0.9% physiological NaCl solution. For LCM/proteomics, protease inhibitor was added (1 tablet/50 ml saline solution) (cOmplete^{TM}, Roche). Brains were removed and snap-frozen in 2-methyl butane at −45°C using dry ice. Histological staining, imaging analysis, and antibodies used are described in **Supplementary Material**.

Methods to Prevent Bias and Exclusion Criteria

Reporting conforms to the ARRIVE guidelines. Mice were excluded determined by a priori criteria if they had a visible stroke in MRI imaging 24 h after surgery (2 mice, 1 per genotype, respectively). Experimenters were blinded during the behavioral assessment, tissue processing, and data analysis. We observed no mortality. All other mice were included. Two samples after microdissection did not result in enough protein for analysis and were not further processed.

Statistical Analyses

All data are presented as scatter dot plots with the mean ± standard deviation. Data were analyzed with GraphPad Prism version 8.2.0. A detailed description of the corresponding statistical analysis is provided in the figure legends or the respective proteomics and connectivity analysis methods.

RESULTS

Development of the Cx30-Cre-ERT2;FLEX-IL6 Mouse Model for Paracrine Cerebral IL-6 Expression

To evaluate the effects of paracrine cerebral IL-6 on cerebral remodeling mechanisms after unilateral CCA occlusion, we created a custom-made mouse model for brain-specific IL-6 secretion at a deliberately chosen time-point. In this model,

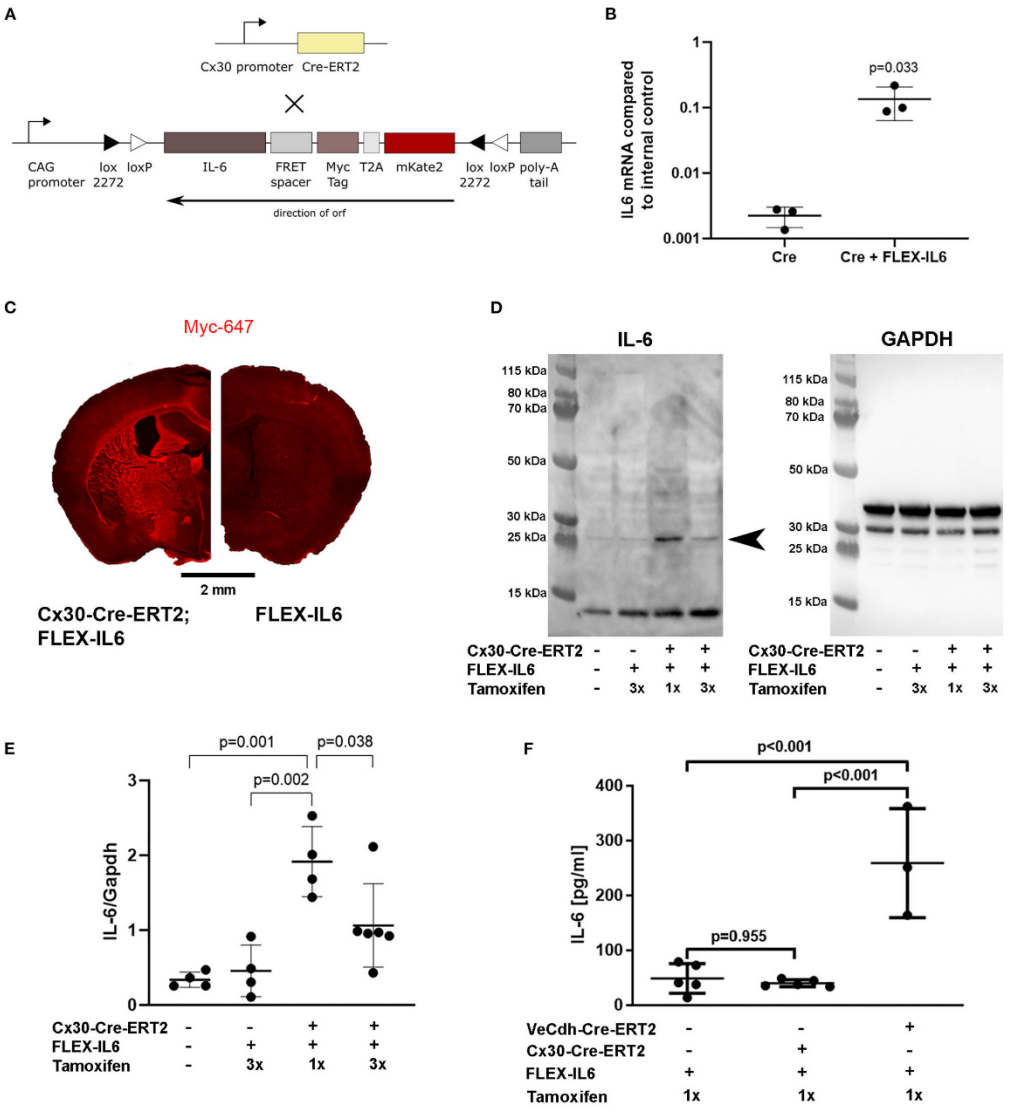

FIGURE 1 | Development of the Cx30-Cre-ERT2;FLEX-IL6 mouse model for brain-specific IL-6 expression. **(A)** Design of the custom-made mouse line for inducible and traceable secretion of IL-6 (FLEX-IL6). The murine *Il6* sequence is linked to a myc-tag followed by the self-cleavage site T2A and mKate2. This construct is inverted and embedded in a flip and excision (FLEX) cassette in the silent R26 locus. To enable paracrine cerebral IL-6 secretion, we crossbred FLEX-IL6 mice with the astrocyte-specific inducible Cre-driver mouse line Cx30-Cre-ERT2. Upon tamoxifen administration, active Cre flips and excises one recombination site and thus permanently induces *Il6* expression in astrocytes. **(B)** Endothelial bEnd.3 were incubated for 1 h with conditioned cell culture supernatants of HEK cells transfected with Cre and the FLEX-IL6 construct or Cre only as negative control and *Il6* mRNA was determined by real-time RT-PCR. Ectopic IL-6 increases bEnd.3 IL-6 expression by almost 100x. $n = 3$ independent experiments. **(C)** Representative Myc-tag staining after tamoxifen administration. Upon induction with tamoxifen, myc-IL-6 is widely expressed in Cx30-CRE-ERT2;FLEX-IL6 mice, while there is no induction in FLEX-IL6 control mice. **(D,E)** Cerebral IL-6 protein levels were determined by immunoblot analysis of brain homogenates of Cx30-Cre-ERT2;FLEX-IL6 mice receiving one mg tamoxifen for 1 or 3 days from $n = 4$–6 mice per group as displayed in the scatter

(Continued)

FIGURE 1 | dot plots. FLEX-IL6 ($n = 4$) mice receiving 1 mg tamoxifen for 3 days and wild-type C57BL/6N ($n = 4$) served as negative controls. Immunoblot IL-6 intensities were normalized to GAPDH intensity (~37 kD). There is a moderate increase of IL-6 in Cx30-Cre-ERT2;FLEX-IL6 mice ($n = 4$) receiving a single tamoxifen dose compared to the control group (~25 kD, arrowhead closed). Mice that received three doses of tamoxifen ($n = 6$) showed increased but significantly lower brain IL-6 than after a single dose. **(F)** IL-6 serum levels were determined using ELISA measurement of mice with astrocytic IL-6 expression (Cx30-Cre-ERT2;FLEX-IL6, $n = 5$), mice with endothelial IL-6 expression (VeCdh-Cre-ERT2; FLEX-IL6, $n = 37$), and Cre-negative controls ($n = 5$). There was a marked increase in serum IL-6 upon endothelial expression. At the same time, IL-6 remained at baseline level comparable to Cre-negative controls upon astrocytic expression. Graphs show scatter dot plots of data from independent samples ± standard deviations. **(B)** Two-tailed unpaired Student's *t*-test. **(E,F)** One-way ANOVA with Tukey's multiple comparison test.

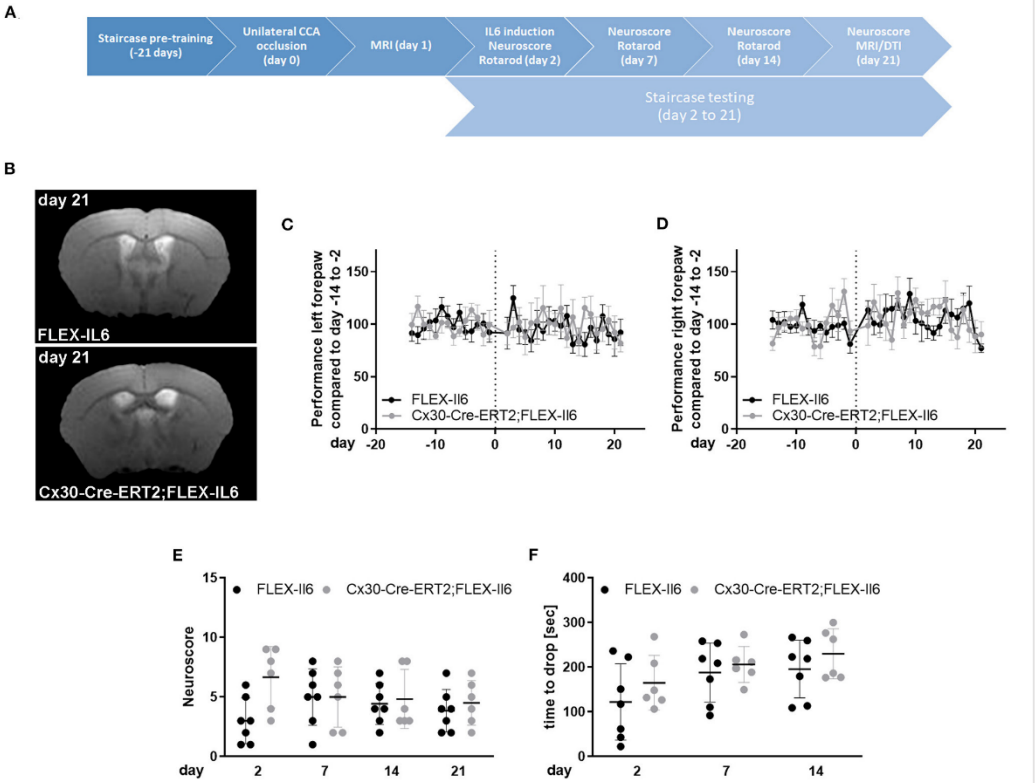

FIGURE 2 | Paracrine IL-6 does not worsen functional outcome or induce strokes after unilateral asymptomatic CCA occlusion. **(A)** Time-scale: 8 Cx30-Cre-ERT2;FLEX-IL6 and 7 FLEX-IL6 mice were pre-trained in the staircase test for 21 days. On day 0, mice received a left-sided unilateral CCA occlusion and an MRI on day 1 after surgery. One Cx30-Cre-ERT2;FLEX-IL6 and one FLEX-IL6 was excluded due to developing a stroke immediately after surgery. On day 2 after surgery, paracrine IL6 was induced by a single tamoxifen administration. Motor function was evaluated on day 2, day 7, and 14 with the Rotarod test and day 21 with the DeSimoni Neuroscore. Forepaw function was evaluated daily with the staircase test from day 2 to day 21. **(B)** T2-weighted MRI scans showed no ischemic lesion or white matter damage 21 days after unilateral carotid occlusion in both genotypes. **(C,D)** Staircase test for the left **(C)** and right **(D)** forepaw. The performance was normalized to the individual performance before surgery. No change in performance was observed compared to the performance before surgery and between genotypes. **(E)** Overall sickness and neurological status were determined by DeSimoni Neuroscore. Cx30-Cre-ERT2;FLEX-IL6 mice ($n = 6$) showed a transient increase in sickness behavior immediately after IL6 induction, which reached no significance compared to FLEX-IL6 control mice ($n = 7$). **(F)** Gross motor performance was evaluated using the RotaRod test. After the intervention, the average time to drop on the moving Rotarod increases over time in the experimental and the control group. There is no significant difference between groups. Graphs show scatter dot plots of data from individual mice ± standard deviations. **(C–F)** Two-way ANOVA with Sidak's multiple comparison test.

a FLEX cassette is integrated into the R26-locus. The FLEX cassette contains murine IL-6 connected to a myc-tag via a linker and mKate2 via a T2A self-cleavage site (**Figure 1A**). This myc-tagged IL-6 was bioactive, which can be seen by the induction of IL-6 in endothelial cells *in vitro* (**Figure 1B**). We have previously shown that IL-6 induces the production of IL-6 in

endothelial cells by a positive feedback loop (4). Crossbreeding of FLEX-IL6 mice with Cx30-Cre-ERT2 mice resulted in the Cx30-Cre-ERT2;FLEX-IL6 mouse model for tamoxifen dependent inducible activation of IL-6 secretion restricted to astrocytes and by this restricted to the brain. Upon tamoxifen administration, we observed a widespread IL-6 expression in the Cx30-Cre-ERT2;FLEX-IL6 mice using immunofluorescence staining for the myc-tag, which is fused to the ectopic IL-6. This expression was not present in the FLEX-IL6 control mice (**Figure 1C**). IL-6 immunoblots of brain homogenate showed a tamoxifen-dependent increase of IL-6 locally in the brain 5 days after a single administration of tamoxifen (**Figures 1D,E**). However, after higher tamoxifen dosing with administration on three consecutive days, we observed decreased IL-6 compared to 1-day administration. In FLEX-IL6 mice without Cx30-Cre-ERT2 we observed no induction of IL-6 compared to wild-type mice. Therefore, we used a single dose of tamoxifen for IL-6 induction in the following experiments. FLEX-IL6 mice without Cre but with tamoxifen treatment served as negative controls. To control for brain specificity of IL-6 induction in the setting of a CCA occlusion, we determined the serum IL-6 levels after tamoxifen administration after surgery (**Figure 1F**). We identified no increase of systemic serum IL-6 levels in Cx30-Cre-ERT2;FLEX-IL6 mice while there was a substantial increase of serum IL6-levels when using an endothelial Cre-driver mouse model (VeCdh-Cre-ERT2;FLEX-IL6). Therefore, using the Cx30-Cre-ERT2;FLEX-IL6 mouse model we can induce paracrine cerebral IL-6 without affecting systemic IL-6 levels.

Paracrine IL-6 Production Does Not Induce Ischemic Tissue Damage or Worsen Functional Outcome After Unilateral CCA Occlusion

We used the mouse model of unilateral CCA occlusion for studying the effects of modest cerebral hypoperfusion to mimic human asymptomatic carotid artery disease. In this mouse model, no deficits in sensorimotor functions occur. We excluded

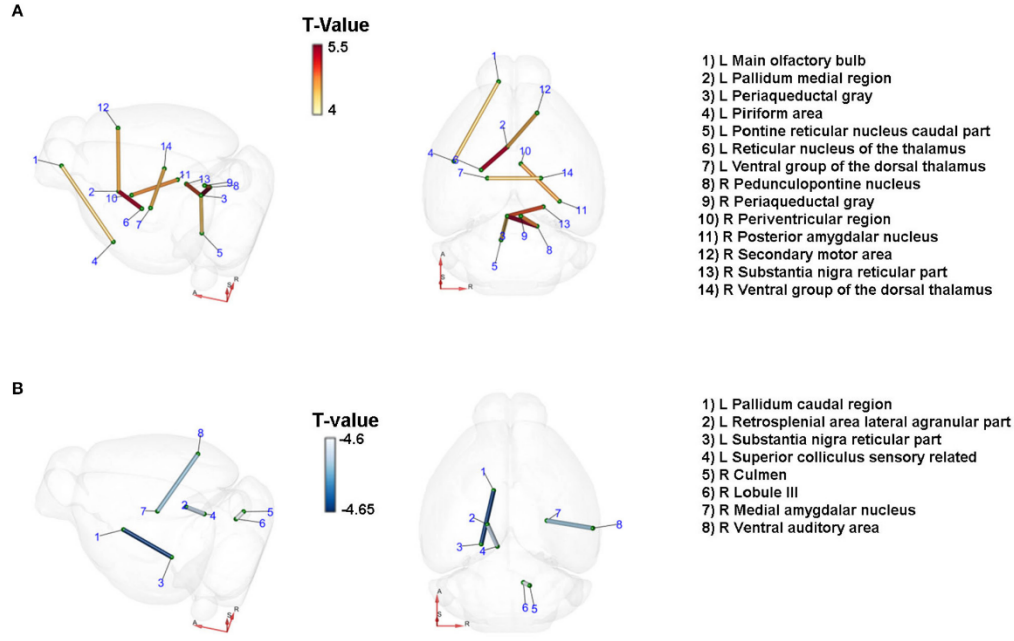

FIGURE 3 | Paracrine IL-6 is a driver of network remodeling after unilateral CCA occlusion. Connections with changes in diffusivity comparing the astrocytic IL-6 (n =6) to control animals (n = 7) at d21 after left CCA occlusion. Coordinates: A = anterior, R = right, S = superior. T-statistics were applied, and all values with $p < 0.001$ were chosen as relevant. Connections were verified by cross-checking to the Janelia Neuron Browser or Allen Brain Mouse Connectivity Explorer. **(A)** Nine connections showed an increase in connectivity. Of those, four were inter-hemispheric connections. Especially connections to the ipsilateral periaqueductal gray increased along with the axis from the contralateral secondary motor cortex to the ipsilateral pallidum and subsequently the thalamus. **(B)** Four connections showed decreased connectivity. On the ipsilateral side, the caudal pallidum and the reticular part of the substantia nigra as well as the connection between the retrosplenial area and the superior colliculus were reduced in strength. On the contralateral side, the connections between the culmen and lobule III and between the medial amygdalar nucleus and the ventral auditory area were decreased.

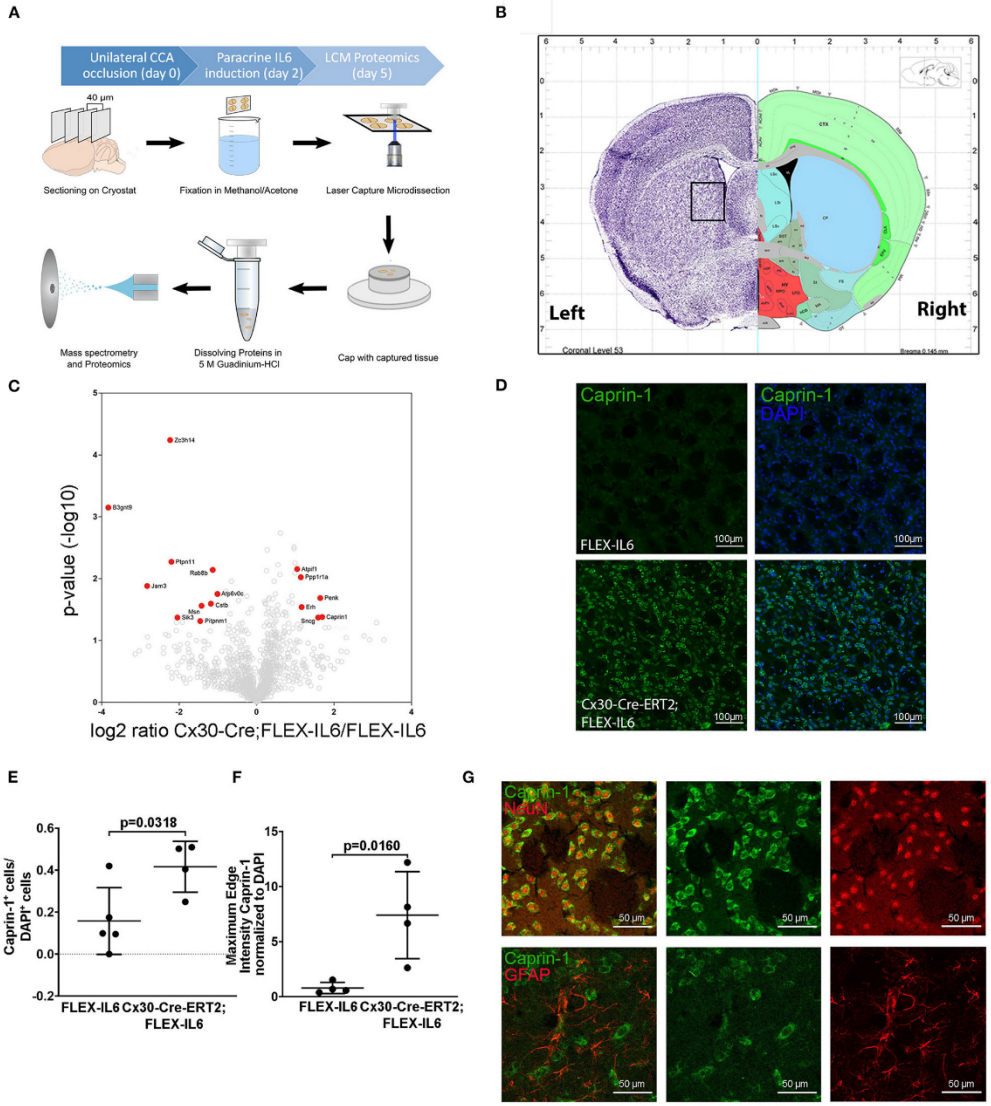

FIGURE 4 | Paracrine IL−6 induces changes of the proteome in the striatum. **(A)** Schematic illustration of the laser capture microscopy (LCM) workflow. Five FLEX-IL6 and four Cx30-Cre-ERT2;FLEX-IL6 mice were used. Paracrine IL-6 secretion was induced 2 days after left-sided unilateral CCA occlusion. Brain tissue is sectioned into 40 µm thick coronal slices and mounted on PEN membrane slides. After methanol/acetone fixation, the tissue is processed with the laser capture microscope. Striatal fiber bundles on the hypoperfused side were isolated. The addition of 5 M guanidinium chloride dissolves the tissue and denatures the proteins. The sample was analyzed using mass spectrometry for proteome analysis. **(B)** Illustration (Allen mouse Brain Atlas) of the anatomical region used for LCM. **(C)** The volcano plot shows log ratio and *p*-value distribution of all quantified proteins. Proteins with significantly ($p < 0.05$, fold change $>/<2$) altered expression are labeled in red. We identified 16 differentially regulated proteins listed in **Table 1**. **(D)** Comparison of caprin-1 staining in FLEX-IL6 and Cx30-Cre-ERT2;FLEX-IL6 mice confirms elevated caprin-1 expression in mice with increased paracrine IL-6. **(E,F)** Automated quantification of nuclei and co-detection of Caprin-1 intensity resulted in a significant increase of the edge nuclei intensity in the caprin−1 channel normalized to DAPI intensity. **(G)** Co-staining of caprin-1 and NeuN and GFAP showed that caprin-1 is localized exclusively in neurons and not detected in astrocytes. Graphs show scatter dot plots of data from individual mice ± standard deviations. **(E,F)** Two-tailed unpaired Student's *t*-test.

mice (one Cx30-Cre-ERT2;FLEX-IL6 and one FLEX-IL6) that developed a stroke peri-interventional. **Figure 2A** shows the time-scale of the experimental setup. We verified that mice did not develop an ischemic lesion in the long term using MR-imaging on day 21 after surgery (**Figure 2B**). Additionally, we assessed sickness behavior and motor skills using behavioral testing in the 21-day follow-up period after CCA occlusion. Skilled pellet retrieval off a staircase gives a readout for front paw fine motor skills. We observed no effect on fine motor functions of the forepaw in the wild-type and experimental group (**Figures 2C,D**). In both groups and for both front paws, the performance was consistently similar to the average baseline performance before unilateral CCA occlusion. The overall sickness and neurological performance (DeSimoni neuroscore) did not differ significantly between groups and over time (**Figure 2E**). Gross motor skill assessed by RotaRod showed no impairment of motor function (**Figure 2F**). The average time to drop did not differ significantly for individual days in-between groups. Therefore, elevated paracrine cerebral IL-6 had no detectable adverse effect on motor functional outcome or general sickness in a model of asymptomatic CCA occlusion.

Paracrine IL-6 Is a Driver of Neuronal Network Remodeling After Unilateral CCA Occlusion

We studied the changes in the brain's connectome by DTI 21 days after unilateral CCA occlusion in an unbiased exploratory approach using an atlas with 154 anatomical regions per hemisphere, resulting in 23,562 [(154*154) – 154] possible

TABLE 1 | IL-6 dependent protein regulations in the striatal fiber tracts*.

UNIPROT ID	Protein names	Gene symbol	Difference LFQ log2 ratio IL-6/ controls	*p*-value (–log 10)	Biological process relevant to cerebral functions (AmiGO 2 or Reference)
Upregulated proteins					
Q60865	Caprin-1	*Caprin1*	1,689	1,380	Positive regulation of dendritic spine morphogenesis
P22005, B1AZQ0	Proenkephalin-A;	*Penk*	1,643	1,690	Locomotory behavior, behavioral fear response
Q9Z0F7	Gamma-synuclein ynuclein	*Sncg*	1,593	1,378	Regulation of dopamine secretion, negative regulation of neuronal death
P84089, G3UW85	Enhancer of rudimentary homolog	*Erh*	1,163	1,542	–
Q9ERT9	Protein phosphatase 1 regulatory subunit 1A	*Ppp1r1a*	1,143	2,028	Promotes memory and learning (15)
E9PV44, O35143	ATPase inhibitor, mitochondrial	*Atpif1*	1,050	2,153	Regulation of ATP metabolic process (16)
Downregulated proteins					
E9Q9C5, P63082, D3Z3B2	V-type proton ATPase 16 kDa Proteolipid subunit	*Atp6v0c*	–1,019	1,758	–
P61028	Ras-related protein Rab-8B	*Rab8b*	–1,139	2,144	–
Q62426	Cystatin-B	*Cstb*	–1,185	1,598	Locomotory behavior, frameshift mutation leads to neurodegeneration (17)
P26041	Moesin	*Msn*	–1,419	1,562	Long-term memory (18)
P35235	Membrane-associated phosphatidylinositol transfer protein 1	*Pitpnm1*	–1,448	1,316	Brain development
E9PU87, F6U8X4, F6U6U5	Serine/threonine-protein kinase SIK3	*Sik3*	–2,043	1,373	–
P35235	Tyrosine-protein phosphatase non-receptor type 11	*Ptpn11*	–2,203	2,271	Axon guidance, brain development, cerebellar cortex formation
Q8BJ05	Zinc finger CCCH domain-containing protein 14	*Zc3h14*	–2,233	4,239	Knockdown reduces Tau aggregation (19)
Q9D8B7	Junctional adhesion molecule C	*Jam3*	–2,828	1,881	Axon regulation, myelination, blood-brain-barrier disruption (20)
F8WI62, Q8VI16	UDP-GlcNAc:betaGal beta-1,3-N-acetylglucosaminyltransferase 9	*B3gnt9*	–3,829	3,153	–

*Up- and down-regulated proteins in striatal corticospinal tract samples ipsilateral to the CCAo. The proteins are sorted by their expression change indicated by the difference of the LFQ log2 ratio between IL-6 animals and controls. Significance is indicated by a log10 p-value.

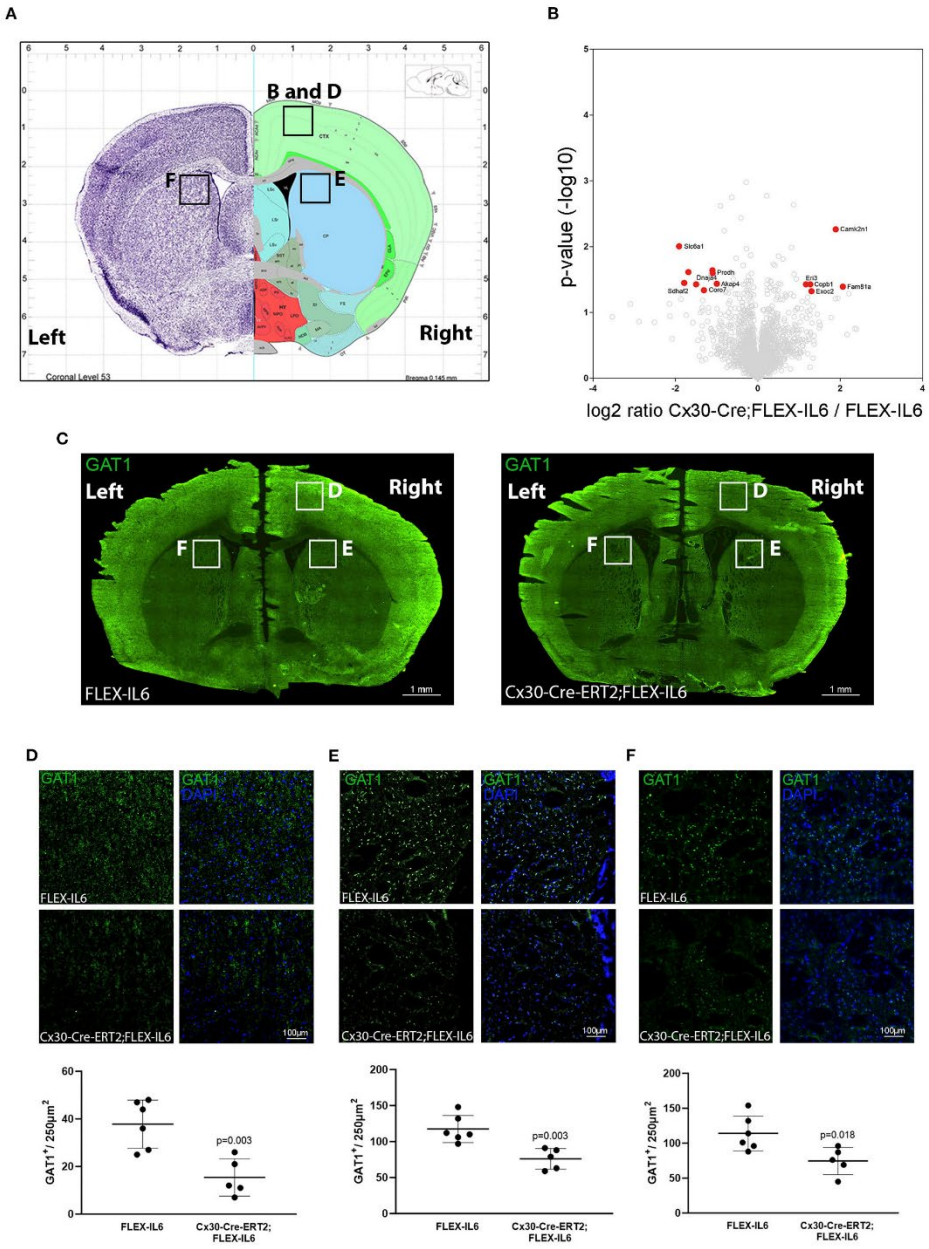

FIGURE 5 | Paracrine IL−6 induces changes of the proteome in the contralateral motor cortex. **(A)** Location of the dissected tissue and histological analysis (Allen mouse Brain Atlas). A part of the motor cortex was isolated on the contralateral hemisphere and the proteome changes were analyzed. **(B)** The volcano plot shows

(Continued)

FIGURE 5 | log ratio and *p*-value distribution of all quantified proteins. Proteins with significantly ($p < 0.05$, fold change >/<2) altered expression are labeled in red. We identified 13 differentially regulated proteins listed in **Table 2**. **(C)** Representative multiple image alignment of Gat1 staining. **(D)** Gat1 staining and quantification in the contralateral motor cortex shows besides focal staining a diffuse signal. The number of focal Gat1 spots is reduced in Cx30-Cre-ERT2;FLEX-IL6 (FLEX-IL6 $n = 6$, Cx30-Cre-ERT2;FLEX-IL6 $n = 5$). In the contralateral **(E)** and ipsilateral **(F)** caudate putamen, Gat1 is strongly expressed with reduction of expression in Cx30-Cre-ERT2;FLEX-IL6 mice. Graphs show scatter dot plots of data from individual mice ± standard deviations. Two-tailed unpaired Student's *t*-test.

connections. Paracrine IL-6 production induced a significant change in connectivity in the context of CCA occlusion (**Figures 3A,B**). At a significance threshold of $p < 0.001$, 17 connections were significantly altered. The physiological feasibility of the connections was verified by cross-checking in the Allen brain connectivity atlas and Janelia Neuron Browser. In total, 3 out of 17 connections could not be verified and were therefore excluded. There was a gain in connectivity between 4 inter-hemispheric connections. In the hypoperfused hemisphere, 3 connections were strengthened, and in the contralateral hemisphere 2 connections. All 4 connections with lowered connectivity were intrahemispheric, with 2 connections reduced on each side. Qualitative assessment of connectivity hints at an overall gain in inter-hemispheric connectivity and, thus, a potential compensation by the contralateral non-affected hemisphere, though unilateral CCA occlusion was functionally asymptomatic.

In the brainstem, the ipsilateral periaqueductal gray showed increased connectivity to several other nuclei of the ipsi- and contralateral brainstem. We identified increased connectivity of the periaqueductal gray to the ipsilateral caudal part of the pontine reticular nucleus, the pedunculopontine nucleus, and the contralateral substantia nigra, and the contralateral periaqueductal gray. The ipsilateral pallidum, part of the basal ganglia, had strengthened connectivity to the ipsilateral reticular nucleus of the thalamus and the contralateral secondary motor area. The connectivity between the ipsi- and the contralateral ventral group of the dorsal thalamus—the relay between the basal ganglia and the primary motor cortex—increased. There was a decrease in connection strength to the ipsilateral reticular substantia nigra. Notably, we identified mainly changes in connections related to motor functions.

Paracrine IL-6 Induces Changes in Protein Composition Within the Striatum

To evaluate the molecular adaptive mechanisms of paracrine cerebral IL-6 after CCA occlusion, we analyzed the effect on protein composition within the ipsilateral striatum. This anatomical region is subject to reduced perfusion. As particularly white matter is damaged in chronic cerebral hypoperfusion, we chose to analyze the striatal fiber tracts, including the capsula interna and the corticospinal tract. To isolate those regions, we used laser capture microdissection (LCM). In our experiment, we assessed proteome changes in the ipsilateral fiber tracts within the hypoperfused striatum on day 5 after occlusion of the CCA for early-stage effects (**Figures 4A,B**). In total, we identified 2,075 proteins in the striatal samples with a 1% FDR threshold. Within these, 16 proteins showed IL-6 dependent differential abundance (**Figure 4C**; **Table 1**). Surprisingly, IL-6 induced no angiogenesis-related proteins in this anatomical region. Mostly proteins related to neuronal functions and stress response such as Synuclein gamma (Sncg), Proenkephalin (Penk), ATP Synthase Inhibitory Factor Subunit 1 (Atpif1), Protein Phosphatase 1 Regulatory Inhibitor Subunit 1A (PP1R1a), and Caprin-1 were induced. STRING GO term analysis of downregulated proteins revealed that most downregulated proteins are membrane-bound organelle and Golgi apparatus related (Cstb, Atp6v0c, Jam3, Rab8b, Pitpnm1, Ptpn11, Zc3h14, Msn, Sik3, B3gnt9). We exemplarily confirmed the induction of Caprin-1 in the paracrine IL-6 expressing mice with immunofluorescence staining (**Figures 4D–F**). Caprin-1 was found in neurons of the striatum, and not in astrocytes (**Figure 4G**).

Paracrine IL-6 Induces Changes in Protein Composition Within the Contralateral Motor Cortex

Analyzing the effects of paracrine IL-6 on the connectivity after CCA occlusion we identified increased connectivity of the contralateral motor cortex to the ipsilateral hypoperfused basal ganglia. We therefore evaluated the molecular changes in the contralateral motor cortex via LCM and subsequent proteome analysis (**Figure 5A**). We identified 2,578 proteins and 13 proteins in the cortical samples that showed differential abundance due to paracrine IL-6 (**Figure 5B**; **Table 2**). Here, STRING GO term analysis of altered proteins showed that high abundance proteins are almost all linked to the plasma membrane system or endomembrane system. Low abundance proteins are mostly part of protein complexes and membrane components (Coa3, Coro7, Dnaja4, Sdhaf2, Slc6a1, Vamp3) including Vamp3—a component of the SNARE complex—or mitochondrial proteins (Coa3, Dnaja4, Prodh, Sdhaf2). Amongst these, we exemplarily analyzed Slc6a1 (also known as Gat1) in histological stainings in a different set of mice than used for LCM-proteomics (**Figure 5C**). We confirmed Gat1 suppression in the contralateral motor cortex (**Figure 5D**). There was widespread suppression of Gat1 in the brain with a noticeable reduction of Gat1 in the caudate putamen in both hemispheres (**Figures 5E,F**).

DISCUSSION

In this study, we show for the first time that paracrine cerebral IL-6 induces cerebral remodeling at an early stage after asymptomatic unilateral carotid occlusion within the first 3 weeks leading to increased inter-hemispheric connectivity and changes in motor system connectivity. By studying the molecular mechanisms induced by paracrine IL-6 early after CCA occlusion, we identified proteins that might serve as targets

TABLE 2 | IL-6 dependent protein regulations in the contralateral motor cortex*.

UNIPROT ID	Protein names	Gene symbol	Difference LFQ log2 ratio IL-6/ controls	*p*-value (–log 10)	Biological process relevant to cerebral functions (AmiGO 2 or Reference)
Upregulated proteins					
Q3UXZ6	Protein FAM81A	*Fam81a*	2,061	1,390	Postsynaptic density (21)
Q6QWF9, Q78WH7	Calcium/calmodulin-dependent protein kinase II inhibitor 1;	*Camk2n1*	1,890	2,266	Prevents long-term memory loss (22), impairs motor learning and LTP (23)
Q9D4H1	Exocyst complex component 2	*Exoc2*	1,301	1,319	Mutations cause brain developmental defects (24)
Q9JIF7, Q8C460	Coatomer subunit beta	*Copb1*	1,262	1,428	Part of COPI complex, reduces amyloid plaques (25)
Downregulated proteins					
A0A0R4J1R9, Q8C460	ERI1 exoribonuclease 3	*Eri3*	1,185	1,424	–
Q60662	A-kinase anchor protein 4	*Akap4*	–0,990	1,433	–
E9Q6W2, Q9D2R6	Cytochrome c oxidase assembly factor 3 homolog, mitochondrial	*Coa3*	–1,092	1,641	Mitochondrial cytochrome c oxidase assembly
A0A0R4J1T9, Q9WU79	Proline dehydrogenase 1, mitochondrial	*Prodh*	–1,136	1,606	Reduced activity causes cognitive impairment (26)
G3X9L5, Q9D2V7	Coronin; Coronin-7	*Coro7*	–1,334	1,343	Actin filament organization
Q9JMC3	Protein FAM81A	*Dnaja4*	–1,459	1,430	–
P63024	Vesicle-associated membrane protein 3	*Vamp3*	–1,695	1,615	SNARE complex, inhibition reduces microglia activation (27)
Q8C6I2	Succinate dehydrogenase assembly factor 2, mitochondrial	*Sdhaf2*	–1,815	1,449	Mitochondrial electron transport, succinate to ubiquinone
P31648	Sodium- and chloride-dependent GABA transporter 1	*Slc6a1*	–1,918	2,004	Gamma-aminobutyric acid import

*Up- and down-regulated proteins in the motor cortex contralateral to the CCAo. The proteins are sorted by their expression change indicated by the difference of the LFQ log2 ratio between IL-6 animals and controls. Significance is indicated by a log10 p-value.

for potential treatment strategies aimed at cerebral remodeling to improve long-term functional outcome after carotid occlusion while avoiding adverse effects.

We showed that paracrine IL-6 induces restructuring mechanisms of neuronal connectivity after unilateral CCA occlusion. The main alterations were seen in strengthened interhemispheric connections between the thalamus and a strengthened connection between the contralateral motor area to the ipsilateral pallidum and the thalamic reticular nucleus. Moreover, there were increases in several connections linked to the periaqueductal gray and the hindbrain in general. The periaqueductal gray is a component of motor systems as an interface between the forebrain and the lower brainstem (28). We assume that this finding represents a general strengthening of downstream motor signaling toward the spinal cord.

Proteome analysis of the hypoperfused striatal fiber tracts showed mainly regulations in proteins related to neuronal functions. The results were ambivalent regarding functional and cognitive effects. On the one hand, we observed protein regulations that would have unfavorable effects: upregulation of Sncg is associated with neurodegenerative diseases (29), and high circulating levels of Penk have been established as a marker for vascular dementia (30). We observed a reduction of Cstb, Jam3, Zc3h14, and Msn, which can cause neuroinflammation and epilepsy (Cstb) (31), blood-brain-barrier disruption (Jam3) (20), impairment of synaptic function (Zc3h14) (32) and long-term memory (Msn) (18). On the other hand, the observed increase in Atpif1 could rescue cells under hypoxic conditions (16). Induced Ppp1r1a can promote long-term potentiation by inhibiting protein phosphatase 1 (PP1), fostering memory and learning (15). Caprin-1 upregulation was verified by immunohistochemistry. This cell-proliferation regulating protein has an additional role in neurons (33). In the brain, Caprin-1—also known as RNG105—is linked to the formation of cytoplasmic stress granules (34). More importantly, it regulates mRNA localization in dendrites and is essential for long-term memory formation via homeostatic AMPA-receptor scaling (35). Interestingly, a recent preprint described STAT-1 and STAT-3—downstream targets of IL-6—as interacting proteins with Caprin-1 detected by immunoprecipitation and proteomics (36).

In the contralateral cortex, we observed ambivalent effects of protein regulations as well. Upregulated proteins almost exclusively have a link to the plasma membrane system or endomembrane system. Camk2n1 can prevent long-term memory loss (22). However, Camk2n1 is an inhibitor of CaMKII, which is necessary for motor learning and long-term potentiation (23). Interestingly, paracrine IL-6 upregulates Copb1 as part of the COPI complex. Bettayeb et al. showed that the COPI complex

could significantly reduce amyloid plaques in Alzheimer's disease, which might prevent cognitive decline (25). Downregulated proteins were part of membrane complexes. Reduced activity of Prodh causes cognitive impairment (26). Albeit, Vamp3, and Gat1 were decreased by paracrine IL-6. Inhibition of Vamp3 reduces activation of microglia, potentially preventing cognitive impairments after surgery (27). Gat1 is a GABA transporter localized in axons, nerve terminals, and astrocytes, removing GABA from the synaptic cleft (37). We observed a widespread reduction of Gat1. Therefore, reduction of Gat1 would lead to induced GABAergic transmission. Gat1 heterozygous mice with reduced Gat1 expression showed enhanced learning (38), whereas Gat knockout mice had learning deficits and an ADHS like phenotype (39). This indicates that there is a dosing effect of Gat1 on cognitive functions. Treatment with the anti-epileptic drug tiagabine, a specific Gat1 inhibitor, does not lead to cognitive impairments in therapeutic dosages (40). Indeed, Gat1 inhibition improved cognitive functions in patients who have epilepsy (41). In the setting of cerebral ischemia, Gat1 inhibition was neuroprotective (42–44). and preserved hippocampal neurons (45).

In summary, paracrine IL-6 promotes cerebral remodeling in the early stage after asymptomatic CCA occlusion on a structural level with increased connectivity in motor systems. Changes in the proteome of the hypoperfused striatum and contralateral motor cortex showed ambivalent results. In terms of cognitive functions, some protein regulations we observed might be unfavorable. These regulations might explain the adverse effects of long-term elevated IL-6 on cognition. However, we identified protein targets that have been shown to reduce cognitive impairments in other pathological settings such as epilepsy or Alzheimer's disease or might improve neuronal resilience to hypoperfusion.

The major limitation of this study lies in its exploratory design. Further studies are needed to confirm the effects of the identified targets on the motor function and cognitive outcomes after CCA occlusion. We modeled the effect of paracrine IL-6 in early stages in a mouse model mimicking asymptomatic carotid artery stenosis. Cognitive decline or flexibility in learning tasks months after the onset of CCA occlusion was not investigated since our focus was exploring cerebral remodeling in the short term. Moreover, the effects should be confirmed in aged mice.

Focusing on the targets identified in our study—either by selectively inhibiting adverse regulations or by enhancing beneficial regulations—might establish a novel treatment strategy to improve long-term outcome in the setting of asymptomatic CCA occlusion by fostering cerebral remodeling. Preventing downregulations of for instance Jam3 or induction of Atpif1 might be challenging. More promising would be the development of a Vamp3 inhibitor. However, most promising would beGat1 inhibition using the FDA-proven anti-epileptic drug tiagabine, which should be evaluated in further studies.

DATA AVAILABILITY STATEMENT

The mass spectrometry proteomics data have been deposited to the ProteomeXchange Consortium via the PRIDE [1] partner repository with the dataset identifier PXD029737.

ETHICS STATEMENT

The animal study was reviewed and approved by Landesamt für Gesundheit und Soziales Berlin.

AUTHOR CONTRIBUTIONS

MTCK, ME, UD, CH, and CJH designed this project and wrote the manuscript. MTCK, SPC, MK, SM, JL, JA, and PB-S performed the experiments and analyzed the results. PM contributed essential experimental advice to mass spectrometry. All authors reviewed and approved the final manuscript.

FUNDING

This work was supported by the Deutsche Forschungsgemeinschaft (DFG, German Research Foundation) to CJH (HO5277/3-1) and CH (HA5741/5-1) and Project-ID 424778381 –TRR 295 to CH and ME; Einstein Centre of Regenerative Therapies (Einstein Kickbox starting grant to CJH); and German Federal Ministry of Education and Research (BMBF CSB 01EO1301) to CH and ME. CJH was a participant in the Charité Clinical Scientist Program funded by the Charité-Universitätsmedizin Berlin and the Berlin Institute of Health. MKu received funding from the Graduate School 203 of the DFG Excellence Initiative, Berlin-Brandenburg School for Regenerative Therapies. ME received funding from DFG under Germany's Excellence Strategy – EXC-2049 – 390688087, BMBF, DZNE, DZHK, EU, Corona Foundation, and Fondation Leducq. Funding to SM, SK, and PB-S was provided by the BMBF under the ERA-NET NEURON scheme (01EW1811) and the DFG (BO 4484/2-1). Noninvasive MRI measurements allowed a longitudinal study design and were supported by Charité 3R, Replace – Reduce – Refine.

ACKNOWLEDGMENTS

Expert technical assistance by Monica Dopatka and Marco Foddis is greatly acknowledged. MRI experiments were supported by Charité 3^R | Replace-Reduce-Refine. The graphical abstract was created with BioRender.com.

SUPPLEMENTARY MATERIAL

The Supplementary Material for this article can be found online at: https://www.frontiersin.org/articles/10.3389/fcvm.2021.805095/full#supplementary-material

REFERENCES

1. Song P, Fang Z, Wang H, Cai Y, Rahimi K, Zhu Y, et al. Global and regional prevalence, burden, and risk factors for carotid atherosclerosis: a systematic review, meta-analysis, and modelling study. *Lancet Glob Health.* (2020) 8:e721–9. doi: 10.1016/S2214-109X(20)30117-0
2. Howard DPJ, Gaziano L, Rothwell PM, Oxford Vascular S. Risk of stroke in relation to degree of asymptomatic carotid stenosis: a population-based cohort study, systematic review, and meta-analysis. *Lancet Neurol.* (2021) 20:193–202. doi: 10.1016/S1474-4422(20)30484-1
3. Lal BK, Dux MC, Sikdar S, Goldstein C, Khan AA, Yokemick J, et al. Asymptomatic carotid stenosis is associated with cognitive impairment. *J Vasc Surg.* (2017) 66:1083–92. doi: 10.1016/j.jvs.2017.04.038
4. Gertz K, Kronenberg G, Kalin RE, Baldinger T, Werner C, Balkaya M, et al. Essential role of interleukin-6 in post-stroke angiogenesis. *Brain.* (2012) 135:1964–80. doi: 10.1093/brain/aws075
5. Hoffmann CJ, Harms U, Rex A, Szulzewsky F, Wolf SA, Grittner U, et al. Vascular signal transducer and activator of transcription-3 promotes angiogenesis and neuroplasticity long-term after stroke. *Circulation.* (2015) 131:1772–82. doi: 10.1161/CIRCULATIONAHA.114.013003
6. Kossmann T, Hans V, Imhof HG, Trentz O, Morganti-Kossmann MC. Interleukin-6 released in human cerebrospinal fluid following traumatic brain injury may trigger nerve growth factor production in astrocytes. *Brain Res.* (1996) 713:143–52. doi: 10.1016/0006-8993(95)01501-9
7. Wright CB, Sacco RL, Rundek T, Delman J, Rabbani L, Elkind M. Interleukin-6 is associated with cognitive function: the Northern Manhattan Study. *J Stroke Cerebrovasc Dis.* (2006) 15:34–8. doi: 10.1016/j.jstrokecerebrovasdis.2005.08.009
8. Yoshizaki K, Adachi K, Kataoka S, Watanabe A, Tabira T, Takahashi K, et al. Chronic cerebral hypoperfusion induced by right unilateral common carotid artery occlusion causes delayed white matter lesions and cognitive impairment in adult mice. *Exp Neurol.* (2008) 210:585–91. doi: 10.1016/j.expneurol.2007.12.005
9. Nishino A, Tajima Y, Takuwa H, Masamoto K, Taniguchi J, Wakizaka H, et al. Long-term effects of cerebral hypoperfusion on neural density and function using misery perfusion animal model. *Sci Rep.* (2016) 6:25072. doi: 10.1038/srep25072
10. Campbell IL, Abraham CR, Masliah E, Kemper P, Inglis JD, Oldstone MB, et al. Neurologic disease induced in transgenic mice by cerebral overexpression of interleukin 6. *Proc Natl Acad Sci USA.* (1993) 90:10061–5. doi: 10.1073/pnas.90.21.10061
11. Gyengesi E, Rangel A, Ullah F, Liang H, Niedermayer G, Asgarov R, et al. Chronic microglial activation in the GFAP-IL6 mouse contributes to age-dependent cerebellar volume loss and impairment in motor function. *Front Neurosci.* (2019) 13:303. doi: 10.3389/fnins.2019.00303
12. Chesworth R, Gamage R, Ullah F, Sonego S, Millington C, Fernandez A, et al. Spatial memory and microglia activation in a mouse model of chronic neuroinflammation and the anti-inflammatory effects of apigenin. *Front Neurosci.* (2021) 15:699329. doi: 10.3389/fnins.2021.699329
13. Emmrich JV, Neher JJ, Boehm-Sturm P, Endres M, Dirnagl U, Harms C. Stage 1 registered report: effect of deficient phagocytosis on neuronal survival and neurological outcome after temporary middle cerebral artery occlusion (tMCAo). *F1000Res.* (2017) 6:1827. doi: 10.12688/f1000research.12537.2
14. Jochner MCE, An J, Lattig-Tunnemann G, Kirchner M, Dagane A, Dittmar G, et al. Unique properties of PTEN-L contribute to neuroprotection in response to ischemic-like stress. *Sci Rep.* (2019) 9:3183. doi: 10.1038/s41598-019-39438-1
15. Munton RP, Vizi S, Mansuy IM. The role of protein phosphatase-1 in the modulation of synaptic and structural plasticity. *FEBS Lett.* (2004) 567:121–8. doi: 10.1016/j.febslet.2004.03.121
16. Garcia-Bermudez J, Cuezva JM. The ATPase Inhibitory Factor 1 (IF1): A master regulator of energy metabolism and of cell survival. *Biochim Biophys Acta.* (2016) 1857:1167–82. doi: 10.1016/j.bbabio.2016.02.004
17. O'Brien A, Marshall CR, Blaser S, Ray PN, Yoon G. Severe neurodegeneration, progressive cerebral volume loss and diffuse hypomyelination associated with a homozygous frameshift mutation in CSTB. *Eur J Hum Genet.* (2017) 25:775–8. doi: 10.1038/ejhg.2017.39
18. Freymuth PS, Fitzsimons HL. The ERM protein Moesin is essential for neuronal morphogenesis and long-term memory in Drosophila. *Mol Brain.* (2017) 10:41. doi: 10.1186/s13041-017-0322-y
19. Guthrie CR, Greenup L, Leverenz JB, Kraemer BC. MSUT2 is a determinant of susceptibility to tau neurotoxicity. *Hum Mol Genet.* (2011) 20:1989–99. doi: 10.1093/hmg/ddr079
20. Mochida GH, Ganesh VS, Felie JM, Gleason D, Hill RS, Clapham KR, et al. A homozygous mutation in the tight-junction protein JAM3 causes hemorrhagic destruction of the brain, subependymal calcification, and congenital cataracts. *Am J Hum Genet.* (2010) 87:882–9. doi: 10.1016/j.ajhg.2010.10.026
21. Dosemeci A, Loo HK, Toy D, Winters CA, Reese TS, Tao-Cheng JH. FAM81A protein, a novel component of the postsynaptic density in adult brain. *Neurosci Lett.* (2019) 699:122–6. doi: 10.1016/j.neulet.2019.02.003
22. Vigil FA, Mizuno K, Lucchesi W, Valls-Comamala V, Giese KP. Prevention of long-term memory loss after retrieval by an endogenous CaMKII inhibitor. *Sci Rep.* (2017) 7:4040. doi: 10.1038/s41598-017-04355-8
23. Wang Q, Yin P, Yu B, Zhao Z, Richter-Levin G, Yu L, et al. Down-regulation of dorsal striatal alphaCaMKII causes striatum-related cognitive and synaptic disorders. *Exp Neurol.* (2017) 298:112–21. doi: 10.1016/j.expneurol.2017.09.004
24. Van Bergen NJ, Ahmed SM, Collins F, Cowley M, Vetro A, Dale RC, et al. Mutations in the exocyst component EXOC2 cause severe defects in human brain development. *J Exp Med.* (2020) 217:e20192040. doi: 10.1084/jem.20192040
25. Bettayeb K, Hooli BV, Parrado AR, Randolph L, Varotsis D, Aryal S, et al. Relevance of the COPI complex for Alzheimer's disease progression in vivo. *Proc Natl Acad Sci USA.* (2016) 113:5418–23. doi: 10.1073/pnas.1604176113
26. Raux G, Bumsel E, Hecketsweiler B, van Amelsvoort T, Zinkstok J, Manouvrier-Hanu S, et al. Involvement of hyperprolinemia in cognitive and psychiatric features of the 22q11 deletion syndrome. *Hum Mol Genet.* (2007) 16:83–91. doi: 10.1093/hmg/ddl443
27. Chen Y, Sun JX, Chen WK, Wu GC, Wang YQ, Zhu KY, et al. miR-124/VAMP3 is a novel therapeutic target for mitigation of surgical trauma-induced microglial activation. *Signal Transduct Target Ther.* (2019) 4:27. doi: 10.1038/s41392-019-0061-x
28. Benarroch EE. Periaqueductal gray: an interface for behavioral control. *Neurology.* (2012) 78:210–7. doi: 10.1212/WNL.0b013e31823fcdee
29. Bras J, Gibbons E, Guerreiro R. Genetics of synucleins in neurodegenerative diseases. *Acta Neuropathol.* (2021) 141:471–90. doi: 10.1007/s00401-020-02202-1
30. Holm H, Nagga K, Nilsson ED, Ricci F, Melander O, Hansson O, et al. High circulating levels of midregional proenkephalin A predict vascular dementia: a population-based prospective study. *Sci Rep.* (2020) 10:8027. doi: 10.1038/s41598-020-64998-y
31. Okuneva O, Li Z, Korber I, Tegelberg S, Joensuu T, Tian L, et al. Brain inflammation is accompanied by peripheral inflammation in Cstb (-/-) mice, a model for progressive myoclonus epilepsy. *J Neuroinflammation.* (2016) 13:298. doi: 10.1186/s12974-016-0764-7
32. Rha J, Jones SK, Fidler J, Banerjee A, Leung SW, Morris KJ, et al. The RNA-binding protein, ZC3H14, is required for proper poly(A) tail length control, expression of synaptic proteins, and brain function in mice. *Hum Mol Genet.* (2017) 26:3663–81. doi: 10.1093/hmg/ddx248
33. Wang B, David MD, Schrader JW. Absence of caprin-1 results in defects in cellular proliferation. *J Immunol.* (2005) 175:4274–82. doi: 10.4049/jimmunol.175.7.4274
34. Solomon S, Xu Y, Wang B, David MD, Schubert P, Kennedy D, et al. Distinct structural features of caprin-1 mediate its interaction with G3BP-1 and its induction of phosphorylation of eukaryotic translation initiation factor 2alpha, entry to cytoplasmic stress granules, and selective interaction with a subset of mRNAs. *Mol Cell Biol.* (2007) 27:2324–42. doi: 10.1128/MCB.02300-06
35. Nakayama K, Ohashi R, Shinoda Y, Yamazaki M, Abe M, Fujikawa A, et al. RNG105/caprin1, an RNA granule protein for dendritic mRNA localization, is essential for long-term memory formation. *Elife.* (2017) 6:e29677. doi: 10.7554/eLife.29677
36. Vu L, Ghosh A, Tran C, Tebung WA, Sidibe H, Garcia-Mansfield K, et al. Defining the caprin-1 interactome in unstressed and stressed conditions. *J Proteome Res.* (2021) 20:3165–78. doi: 10.1021/acs.jproteome.1c00016

37. Borden LA. GABA transporter heterogeneity: pharmacology and cellular localization. *Neurochem Int.* (1996) 29:335–56. doi: 10.1016/0197-0186(95)00158-1
38. Shi J, Cai Y, Liu G, Gong N, Liu Z, Xu T, et al. Enhanced learning and memory in GAT1 heterozygous mice. *Acta Biochim Biophys Sin.* (2012) 44:359–66. doi: 10.1093/abbs/gms005
39. Yang P, Cai G, Cai Y, Fei J, Liu G. Gamma aminobutyric acid transporter subtype 1 gene knockout mice: a new model for attention deficit/hyperactivity disorder. *Acta Biochim Biophys Sin.* (2013) 45:578–85. doi: 10.1093/abbs/gmt043
40. Aikia M, Jutila L, Salmenpera T, Mervaala E, Kalviainen R. Comparison of the cognitive effects of tiagabine and carbamazepine as monotherapy in newly diagnosed adult patients with partial epilepsy: pooled analysis of two long-term, randomized, follow-up studies. *Epilepsia.* (2006) 47:1121–7. doi: 10.1111/j.1528-1167.2006.00545.x
41. Dodrill CB, Arnett JL, Shu V, Pixton GC, Lenz GT, Sommerville KW. Effects of tiagabine monotherapy on abilities, adjustment, and mood. *Epilepsia.* (1998) 39:33–42. doi: 10.1111/j.1528-1157.1998.tb01271.x
42. Chen Xu W, Yi Y, Qiu L, Shuaib A. Neuroprotective activity of tiagabine in a focal embolic model of cerebral ischemia. *Brain Res.* (2000) 874:75–7. doi: 10.1016/S0006-8993(00)02554-3
43. Yang Y, Li Q, Wang CX, Jeerakathil T, Shuaib A. Dose-dependent neuroprotection with tiagabine in a focal cerebral ischemia model in rat. *Neuroreport.* (2000) 11:2307–11. doi: 10.1097/00001756-200007140-00048
44. Lie ME, Gowing EK, Clausen RP, Wellendorph P, Clarkson AN. Inhibition of GABA transporters fails to afford significant protection following focal cerebral ischemia. *J Cereb Blood Flow Metab.* (2018) 38:166–73. doi: 10.1177/0271678X17743669
45. Inglefield JR, Perry JM, Schwartz RD. Postischemic inhibition of GABA reuptake by tiagabine slows neuronal death in the gerbil hippocampus. *Hippocampus.* (1995) 5:460–8. doi: 10.1002/hipo.450050508

Conflict of Interest: The authors declare that the research was conducted in the absence of any commercial or financial relationships that could be construed as a potential conflict of interest.

Publisher's Note: All claims expressed in this article are solely those of the authors and do not necessarily represent those of their affiliated organizations, or those of the publisher, the editors and the reviewers. Any product that may be evaluated in this article, or claim that may be made by its manufacturer, is not guaranteed or endorsed by the publisher.

Received: 6 August 2019 | Revised: 17 December 2019 | Accepted: 19 December 2019

DOI: 10.1002/glia.23778

GLIA

WILEY

RESEARCH ARTICLE

SorCS2 facilitates release of endostatin from astrocytes and controls post-stroke angiogenesis

Anna R. Malik[1,2] | Janet Lips[3,4,5] | Malgorzata Gorniak-Walas[1] | Diede W. M. Broekaart[6] | Antonino Asaro[1] | Melanie T. C. Kuffner[3,4] | Christian J. Hoffmann[3,4] | Majed Kikhia[3,4,7] | Monika Dopatka[3,4] | Philipp Boehm-Sturm[3,4,8] | Susanne Mueller[3,4,8] | Ulrich Dirnagl[3,4,5,7,9] | Eleonora Aronica[6,10] | Christoph Harms[3,4,5,7] | Thomas E. Willnow[1]

[1]Max-Delbrueck-Center for Molecular Medicine, Berlin, Germany

[2]Nencki Institute of Experimental Biology, Polish Academy of Sciences, Warsaw, Poland

[3]Department of Experimental Neurology, Charité—Universitätsmedizin Berlin and Berlin Institute of Health, Neurocure Cluster of Excellence, Berlin, Germany

[4]Charité—Universitätsmedizin Berlin, Center for Stroke Research Berlin, Berlin, Germany

[5]Berlin Institute of Health, QUEST Centre for Transforming Biomedical Research, Berlin, Germany

[6]Amsterdam UMC, University of Amsterdam, Department of (Neuro) Pathology, Amsterdam Neuroscience, Amsterdam, the Netherlands

[7]Charité—Universitätsmedizin Berlin, Einstein Center for Neurosciences Berlin, Berlin, Germany

[8]Charité—Universitätsmedizin Berlin, Charité Core Facility 7T Experimental MRIs, Berlin, Germany

[9]German Centre for Neurodegenerative Diseases, Berlin, Germany

[10]Stichting Epilepsie Instellingen Nederland (SEIN), Heemstede, The Netherlands

Correspondence
Anna R. Malik, Nencki Institute of Experimental Biology, Pasteura-Str. 3, 02-093 Warsaw, Poland.
Email: a.malik@nencki.edu.pl

Thomas E. Willnow, Max-Delbrueck-Center for Molecular Medicine, Robert-Roessle-Str. 10, 13125 Berlin, Germany.
Email: willnow@mdc-berlin.de

Funding information
Berlin Institute of Health, Grant/Award Number: TRG7; Deutsche Forschungsgemeinschaft, Grant/Award Numbers: EXC-2049 - 390688087, HA5741/5-1, HO5177/3-1, GSC 203; Fundacja na rzecz Nauki Polskiej, Grant/Award Number: 5CEF/18-00; German Federal Ministry of Education and Research, Grant/Award Numbers: 01EO1301, 01EW1811; H2020 European Research Council, Grant/Award Number: 335692

Abstract

SorCS2 is an intracellular sorting receptor of the VPS10P domain receptor gene family recently implicated in oxidative stress response. Here, we interrogated the relevance of stress-related activities of SorCS2 in the brain by exploring its role in ischemic stroke in mouse models and in patients. Although primarily seen in neurons in the healthy brain, expression of SorCS2 was massively induced in astrocytes surrounding the ischemic core in mice following stroke. Post-stroke induction was likely a result of increased levels of transforming growth factor β1 in damaged brain tissue, inducing *Sorcs2* gene transcription in astrocytes but not neurons. Induced astrocytic expression of SorCS2 was also seen in stroke patients, substantiating the clinical relevance of this observation. In astrocytes in vitro and in the mouse brain in vivo, SorCS2 specifically controlled release of endostatin, a factor linked to post-stroke angiogenesis. The ability of astrocytes to release endostatin acutely after stroke was lost in mice deficient for SorCS2, resulting in a blunted endostatin response which coincided with impaired vascularization of the ischemic brain. Our findings identified activated astrocytes as a source for endostatin in modulation of post-stroke

Christoph Harms and Thomas E. Willnow contributed equally to this study.

angiogenesis, and the importance of the sorting receptor SorCS2 in this brain stress response.

KEYWORDS

cytokine, glial scar, ischemia, protein sorting, VPS10P domain receptors

1 | INTRODUCTION

SorCS2 is a member of the VPS10P domain receptors gene family, a unique class of sorting receptors expressed in neurons of the mammalian nervous system (Willnow, Petersen, & Nykjaer, 2008). VPS10P domain receptors are best recognized for their ability to shuttle target proteins between intracellular compartments and the neuronal cell surface. By doing so, they regulate the surface exposure of neuronal receptors or activity-dependent secretion of signaling molecules, as shown for neurotrophin receptors or brain-derived neurotrophic factor, respectively (Z.-Y. Chen et al., 2005; Vaegter et al., 2011). The relevance of neuronal protein sorting by VPS10P domain receptors is underscored by their causal involvement in psychiatric and neurodegenerative diseases, including Huntington's disease, Alzheimer's disease, and frontotemporal dementia (Reitz, 2015; Willnow et al., 2008).

Recently, we documented that SorCS2 is unique among the various VPS10P domain receptors as its expression is up-regulated in response to oxidative stress and epilepsy in neurons (Malik et al., 2019). Under these conditions, SorCS2 promotes cell surface sorting of the neuronal amino acid transporter EAAT3, facilitating EAAT3-mediated uptake of cysteine for production of the reactive oxygen species scavenger glutathione (Malik et al., 2019). Ultimately, induced expression of SorCS2 enables neurons to cope with oxidative stress and protects them from seizure-induced cell death.

To explore a global role for SorCS2 as a stress-induced protein in multiple brain injuries, we here assessed its significance in stroke, a pathological condition linked to severe oxidative stress. Surprisingly, while up-regulation of SorCS2 expression was observed in an experimental mouse model of stroke, this induction was specific to astrocytes, a cell type that normally does not express this receptor. In activated astrocytes, SorCS2 controlled secretion of endostatin and promoted post-stroke angiogenesis. Our findings corroborated a role for SorCS2 as a stress-induced factor and uncovered its cell type-specific actions in protection from brain injuries, such as ischemic stroke.

2 | MATERIALS AND METHODS

2.1 | Mouse models

Mice with a targeted disruption of murine *Sorcs2* (KO) have been described (Glerup et al., 2014). KO males and wild-type littermate controls (WT) used for in vivo studies were 8–14 weeks of age, generated by heterozygous breedings on an inbred C57BL/6N background. Animals were kept under 12 hr/12 hr light/dark cycle with free access to food and water. Newborn mice for astrocytic and neuronal cultures were obtained by homozygous breeding of the respective WT or KO strains. Animal experimentation was performed following approval by local committees of the State of Berlin (X9012/12, X9007/17, G 0157/17).

2.2 | Human tissue samples

Brain tissue samples used in this study for immunostainings were obtained from the archives of the department of Neuropathology of the Amsterdam UMC (University of Amsterdam, the Netherlands). Three acute stroke cases (injury-death interval <2 weeks) and four autopsy controls without any history of neurologic diseases were included. Supporting Information Table S1 summarizes the clinical characteristics of patients and controls. The age and gender did not differ between stroke patients and autopsy controls ($p > .05$, Mann Whitney *U* test). Material for primary astrocyte cultures was collected after a written informed consent for the use of the material for research purposes had been obtained by the Bloemenhove clinic from all donors. All human specimens were obtained and used in accordance with the Declaration of Helsinki and the Amsterdam UMC Research Code provided by the Medical Ethics Committee of the AMC. Local ethical committees of the participating centers gave permission to undertake the study.

2.3 | Middle cerebral artery occlusion

Filamentous occlusion of the middle cerebral artery was performed as described (Dirnagl & Members of the MCAO-SOP Group, 2012). Mice were anaesthetized using 2.5% (vol/vol) isoflurane for induction and 1.5% (vol/vol) isoflurane for maintaining anesthesia in a mixture with 25% O_2 and 75% N_2O. Cerebral ischemia was induced by introducing a 8–0 silicon-rubber coated suture (Doccol Corp., Sharon, MA) into the left internal carotid artery and by advancing it to the anterior cerebral artery, thereby occluding the middle cerebral artery. The filament was withdrawn after an occlusion time of 45 min. Body temperature was maintained at 37.0 ± 0.5°C throughout the experiment using a feed-back controlled heating pad and a rectal probe (Fine Science Tools GmbH, Heidelberg). During middle cerebral artery occlusion (MCAo) and for at least 2 hr after reperfusion, animals were allowed to recover in a heated cage (Peco Services, Cumbria, UK).

Mice were randomized and blinded for concealment of genetic group allocation and the order of surgery. In the short-term studies

(1 and 3 days), no mortality was observed and no mice were excluded from analysis. In the long-term study (21 days) 4 WT (21%) and 4 KO (20%) died within 1 week after MCAo and mice with no stroke (technical failure; 2 WT and 2 KO) or stroke volume approximately <3 mm^3 (3 WT and 3 KO) were excluded from analysis.

2.4 | Brain vasculature labeling

Mice were anesthetized with Ketamine/Xylazine and a solution of DyLight488-labeled *Lycopersicon esculentum* lectin (#DL-1174 Vectorlab) was injected intravenously (1 mg/ml; 4 μl per gram bodyweight). After 180 s, mice were transcardially perfused with 4% paraformaldehyde (PFA)/phosphate-buffered saline (PBS). Brains were isolated and incubated in 4% PFA in PBS (overnight) and in 30% sucrose/PBS (72 hr), and frozen in −40°C isopentane prior to sectioning. A total of 3 WT mice and 1 KO mouse were excluded from the vessels analysis because of technical failures of lectin staining (heart arrest during injection or bad circulation).

2.5 | Cell culture experiments

Cultures enriched in astrocytes were prepared from newborn mice according to published protocols (Parnis et al., 2013). In brief, blood vessels and meninges were removed from cortical tissue which was next trypsinized and dissociated in presence of DNAse. Cells were plated on poly-L-lysine-coated flasks and cultured in Dulbecco's Modified Eagle's Medium (DMEM) with 10% FBS and penicillin/streptomycin. After 2 days, cells were washed to remove cellular debris. After 7 days in vitro, cultures were shaken extensively to remove microglia and the astrocytes were plated for experiments.

Cells were treated with 10 ng/ml transforming growth factor β (TGF-β1; R&D Biosystems, 7666-MB) in serum-free DMEM for 3, 6, 24, or 48 hr. Control cells were incubated in DMEM for 24 hr. For cytokines measurements, astrocytes were stimulated with 100 nM Phorbol 12-myristate 13-acetate (PMA) and 2.5 μM ionomycin for 3 hr or left untreated (control). For endostatin measurements, astrocytes were washed and incubated in serum-free DMEM for 24 hr.

Neuronal cultures were prepared from hippocampi and cortices of newborn mice as described earlier (Malik et al., 2019). In brief, cultures were prepared using enzymatic digestion with papain and plated at the density of 83,000 cells/cm^2. After 10 days in culture, the cells were treated with 10 ng/ml TGF-β1 for 6, 24 or 48 hr or left untreated.

Human primary fetal astrocyte-enriched cultures were obtained from human fetal brain tissue (14–19 weeks of gestation) obtained from medically-induced abortions. Cells isolation was performed as described (Aronica, Gorter, Rozemuller, Yankaya, & Troost, 2005). Briefly, the tissue was digested with trypsin, mechanically disrupted, and the cell suspension was plated in DMEM/Ham's F10 (1:1) medium supplemented with penicillin/streptomycin and 10% fetal calf serum. Cultures reached confluence after 2–3 weeks. Secondary astrocyte cultures for experimental manipulation were used at passage 2–5. Cells plated on poly-L-lysine-coated plates were stimulated with human recombinant TGF-β1 (Peprotech, 10 ng/ml) for 24 hr.

2.6 | ELISA measurements

Sample preparation is described in Supporting Information. Following enzyme-linked immunosorbent assay (ELISA) kits were used: TGF-β1 (Abcam, ab119557), GFAP (Millipore, NS830), endostatin (Boster, EK1376), U-Plex Biomarker Group 1 assay (Meso Scale Diagnostics, K15083K). For technical reasons, not all the samples were included in GFAP and TGF-β1 ELISA measurements. Brain and blood plasma samples used for endostatin measurements were selected based on the results of tissue sections stainings and GFAP ELISA measurements to include mice with similar lesion area and localization and comparable GFAP levels.

2.7 | Protein array

Proteome Profiler Mouse Angiogenesis Array Kit (R&D Systems, ARY015) was used according to manufacturer's instructions. Used tissue samples were selected based on the results of tissue sections stainings and GFAP ELISA measurements to include mice with similar lesion area and localization and comparable GFAP levels. Tissue lysates were prepared as for ELISA, diluted in Array Buffer 6 and the total amount of 350 μg protein was loaded on the membrane. Signal intensities were measured with use of LI-COR Imaging System and quantified with Image Studio Lite software. In one experiment, four samples (WT ipsi, WT contra, KO ipsi, KO contra; ipsi and contra samples from the same mouse brain) were processed and analyzed in parallel. Signal intensities were normalized to the mean value obtained for a given protein in contralateral samples (WT and KO) in the same experiment. In total, the experiment was repeated 3 times on different pairs (WT and KO) of mice and the results were combined.

2.8 | Immunostaining

Following antibodies were used: anti-SorCS2 (R&D Systems, AF4237, 1:100, for mouse tissue and cells; rabbit anti-SorCS2, Lifespan Biosciences, LS-C501334, 1:450, for human tissue), Cy3-labeled anti-GFAP (Sigma, C9205, 1:1,000, for mouse tissue and cells), anti-GFAP (monoclonal mouse, Sigma, 1:4,000, for human tissue), biotinylated anti-NeuN (Millipore, MAB377B, 1:100, for murine tissue), mouse anti-NeuN (Millipore, MAB377 (clone A60), 1:2,000, for human tissue). Details on samples preparation and staining protocols are given in Supporting Information.

2.9 | Western blot

Tissue and cell lysates were analyzed by western blot using the following antibodies: anti-SorCS2 (R&D Systems, AF4237, 1:1,000),

anti-p-ERK (Cell Signaling, 4370, 1:2,000), anti-actin (Abcam, ab8227, 1:2,000), anti-GFAP (Millipore, MAB360, 1:1,000). Signal was registered with digital LI-COR imaging system and quantified using the Image Studio Lite software.

2.10 | Quantitative RT-PCR

RNA was extracted using TRIzol reagent and purified with RNeasy Mini Kit (QIAGEN). Reversely transcribed cDNA was subjected to quantitative real-time polymerase chain reaction (qRT-PCR) analysis. For murine samples, following Taqman Gene Expression Assays were used: Actb (actin, Mm02619580), GAPDH (Mm99999915), Col18a1 (collagen XVIII, Mm00487131), and SORCS2 (Mm00473050). Col18a1 and SorCS2 transcript levels were shown relative to Actb or GAPDH as specified in the respective figure legends. For human samples, SYBR Green method was used with the following PCR primers: *SORCS2* (forward: GTTTGTCATCGGGCTCTTCG, reverse: GTCCTGCCTGGCCGTTTC) and *EF1a* (forward: ATCCACCTTTGGGTCGCTTT, reverse: CCGCAACTGT CTGTCTCATATCAC). *SORCS2* transcript levels were given relative to EF1α as described (Ramakers, Ruijter, Deprez, & Moorman, 2003; Ruijter et al., 2009).

2.11 | Image analysis

Stroke lesion size was analyzed with use of ImageJ software. Lesions and whole brain sections were marked manually based on the images of NeuN, GFAP and DAPI stainings and their areas were measured. For 1 KO mouse, measuring lesion size was not possible due to technical problems with sectioning. Areas covered by blood vessels were analyzed automatically with use of Cell Profiler software. Vessels length was analyzed manually with use of ImageJ software with NeuronJ plugin. For comparison between the two hemispheres of individual mouse brains, data were normalized to the mean value obtained for the contralateral side. For comparison between the two genotypes, data were normalized to the mean value obtained for WT mice analyzed in the same set.

2.12 | Statistical analysis

For in vivo experiments, an indicated number n is the number of mice per group, and for astrocytic and neuronal culture experiments n is the number of independent preparations (biological replicates) used. The study was powered according to the ARRIVE guidelines to detect differences in cytokine levels using two-way analysis of variance (ANOVA) for side and genotype interactions with α error probe of 0.05 and Power of 0.8 and 0.7 effect size based on F tests with critical $F = 3.5$ for a minimum number of $n = 6$ per sample size (G*Power 3.1.9.2). Statistical analyses were performed using GraphPad Prism software. For comparison between two experimental groups, a two-tailed unpaired t test was used with the exception of direct comparison of TGF-β1 levels in the two hemispheres of the same mouse brain where paired t test was used. For data with three or more groups and one independent variable, one-way ANOVA with Dunnett's multiple comparisons test was used. For data with two independent variables, two-way ANOVA with Tukey's multiple comparisons test was applied. For ELISA and western blot quantifications, outlier analysis was performed using Grubb's and ROUT tests and individual datapoints were excluded accordingly. The details of statistical analysis are specified in the figure legends.

3 | RESULTS

3.1 | SorCS2 is induced in astrocytes surrounding the ischemic core

To query the significance of SorCS2 for ischemic stroke, we subjected mice either wild-type (WT) or genetically deficient for *Sorcs2* (KO) to 45 min of transient MCAo, an experimental model commonly used in mice (Dirnagl & Members of the MCAO-SOP Group, 2012). In WT brains 3 days after MCAo, immunostaining for neuronal (NeuN) and astrocytic (GFAP) markers revealed severe neuronal cell loss and astrogliosis in the ipsilateral hemisphere (Figure 1a). SorCS2 expression in these brains was massively induced in reactive astrocytes within the glial scar surrounding the ischemic core (region 1, Figure 1b,c) and to a lesser extent also in other regions adjacent to the lesion (regions 2 and 4, Figure 1b,c). Little to no SorCS2 expression was seen in astrocytes in the contralateral hemisphere (regions 3 and 5, Figure 1b,c). Induced expression in activated astrocytes was surprising as SorCS2 expression in the normal murine brain is predominantly seen in neuronal cell types (Glerup et al., 2014), particularly in neurons of the hippocampal CA2 region, in pyramidal neurons of the cerebral cortex, and in striatal neurons (Supporting Information Figure S1). Post-stroke induction of SorCS2 expression was restricted to astrocytes as no overt increase in neuronal SorCS2 immunoreactivity was seen 1 (Supporting Information Figure S2) or 3 days after ischemic stroke (Figure 1b,c and Supporting Information Figure S3). Similar to the situation in mouse models, SorCS2 expression in the healthy human brain was primarily visible in neurons and only occasionally in astrocytes (Supporting Information Figure S4). However, SorCS2 expression was up-regulated in astrocytes following ischemia in stroke patients, corroborating the clinical relevance of our observations (Figure 1d).

Ischemic stroke triggers release of multiple cytokines and growth factors that promote tissue regeneration. Of note, increased levels of TGF-β were reported in the plasma of stroke patients (Yan, Greer, & McCombe, 2012) and its expression was induced in the murine brain following ischemia (Zhang et al., 2018). TGF-β has been implicated in processes of post-stroke recovery, including glial scaring and angiogenesis (Meng et al., 2016; Pardali, Goumans, & ten Dijke, 2010; Zhu et al., 2017). In line with these findings, we detected increased levels of TGF-β1 in the ipsilateral hemispheres of the WT brains 3 days after MCAo (Figure 2a). Application of TGF-β1 induced levels of SorCS2 transcript (Figure 2b) and protein (Figure 2c,d) in primary murine astrocytes.

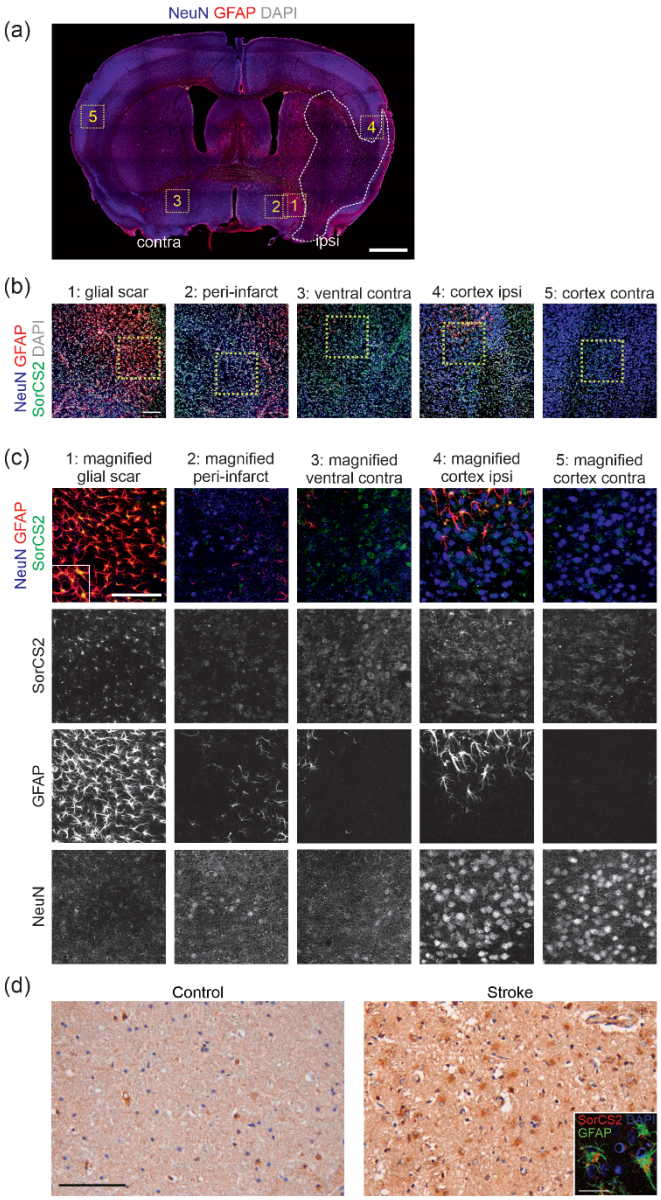

FIGURE 1 SorCS2 expression is induced in astrocytes after ischemic stroke. (a) Coronal brain section of a wild-type mouse 3 days after 45 min MCAo. Sections were immunostained for GFAP (red; astrocytes) and NeuN (blue; neurons), and counterstained with DAPI (grayscale). Scale bar, 1 mm. Ipsilateral (ipsi) and contralateral (contra) hemispheres are indicated. The ischemic core is indicated by white dashed line. Numbered yellow dashed boxes highlight regions shown in (b). (b) Representative images of brain sections stained for GFAP (red; astrocytes), NeuN (blue; neurons), SorCS2 (green), and counterstained with DAPI (grayscale) as marked in (a). Yellow dashed boxes indicate regions shown as higher magnification images in (c). Maximum intensity projections of confocal *z*-sections are shown. Scale bar, 50 μm. (c) Higher magnification of regions indicated in (b). The upper row of panels shows merged images for GFAP (red, astrocytes), NeuN (blue, neurons), and SorCS2 (green) immunosignals. Panels below show the separated channels in grayscale. Robust SorCS2 expression in GFAP-positive cells in the glial scar region is visible. By contrast, no increase in neuronal SorCS2 signal intensities is seen in any of the analyzed regions of the ipsilateral as compared to the contralateral side. The inset in the image of the glial scar region shows a higher magnification of SorCS2-positive astrocytes. Maximum intensity projections of confocal *z*-sections are shown. Scale bar, 50 μm. (d) SorCS2 immunostaining (brown) in the human control brain and in the brain of a patient after stroke. The inset in the right panel shows cells immunofluorescently stained for SorCS2 (red) and astrocyte marker GFAP (green) in post-stroke brain tissue. Scale bars: overview, 100 μm; inset, 25 μm

Similarly, SorCS2 mRNA levels were also increased in cultured human fetal astrocytes by TGF-β1 treatment (Figure 2e). By contrast, induction was not observed in primary neurons treated with TGF-β1 (Figure 2f), providing a possible molecular explanation for the astrocyte-specific induction of SorCS2 expression following ischemic stroke.

3.2 | SorCS2-deficient mice show normal post-stroke astrocyte activation and cytokines levels

To elaborate on the role of SorCS2 in activated astrocytes, we performed a comparative analysis of stroke-driven astrogliosis in WT

animals and in mice lacking this receptor (KO). Three days after MCAo, the size of the ischemic lesion was similar in both genotypes (Figure 3a,b). Also, the extent of astrocyte activation in the ipsilateral hemisphere was comparable as shown by immunodetection of GFAP on histological sections (Figure 3a) and in brain lysates (Figure 3c,d).

Activated astrocytes drive inflammatory responses through release of cytokines. To investigate the consequence of SorCS2 deficiency on this response, we performed cytokine profiling of ipsi- and contralateral hemispheres of WT and KO mice 3 days after MCAo. Among the tested cytokines, IL-1β, IL-5, IL-10, IL-13, IL-16, IL-17A, IL-17C, IL-21, IL-22, IL-23, and IFNγ showed no differences in levels between ipsi- and contralateral hemispheres (Supporting Information - Figure S5). GM-CSF, TNFα, KC/GRO, IL-2, MCP-1, MIP-1α, MIP-2, IP-10, EPO, MIP-1β, MIP-3α, and IL-12p70 were up-, while VEGF-A was down-regulated in ipsilateral as compared to contralateral hemispheres (Figure 3e and Supporting Information Figure S5). However, this response was seen in WT and KO mice to a similar extent.

3.3 | SorCS2-deficient mice fail to induce endostatin expression after stroke

To identify factors secreted from astrocytes in a SorCS2-dependent manner, we assayed the levels of proteins relevant for post-injury regeneration using protein arrays. Three days after MCAo, levels of coagulation factor III and FGF1 did not differ remarkably between ipsi- and contralateral hemispheres (Figure 4a and Supporting Information Figure S6). Osteopontin, CXCL4, CCN3, serpin E1, and IGFBP2 increased in the ipsilateral hemisphere regardless of *Sorcs2* genotype (Figure 4a and Supporting Information Figure S6). However, increases in levels of IGFBP3 and endostatin in the ipsilateral hemisphere were seen in WT but not KO brains, suggesting SorCS2 dependency (Figure 4a–c).

The association of plasma IGFBP3 levels with *SORCS2* in humans had been reported (Kaplan et al., 2011), validating our screening approach for identifying SorCS2 targets in the ischemic brain. Here, we focused on endostatin, a potent anti-angiogenic factor produced from collagen XVIII by proteolysis (Sasaki et al., 1998). Prior studies had implicated endostatin in post-stroke recovery (Gertz et al., 2006; Navarro-Sobrino et al., 2011). We confirmed the impact of SorCS2 on endostatin levels by showing that endostatin levels increased twofold in the ipsilateral as compared to the contralateral hemisphere of WT brains at 3 days after MCAo. This effect was lost in KO mice (Figure 4d). The rise in endostatin levels in the ipsilateral WT hemisphere correlated with the lesion size (Figure 4e) and was specific to

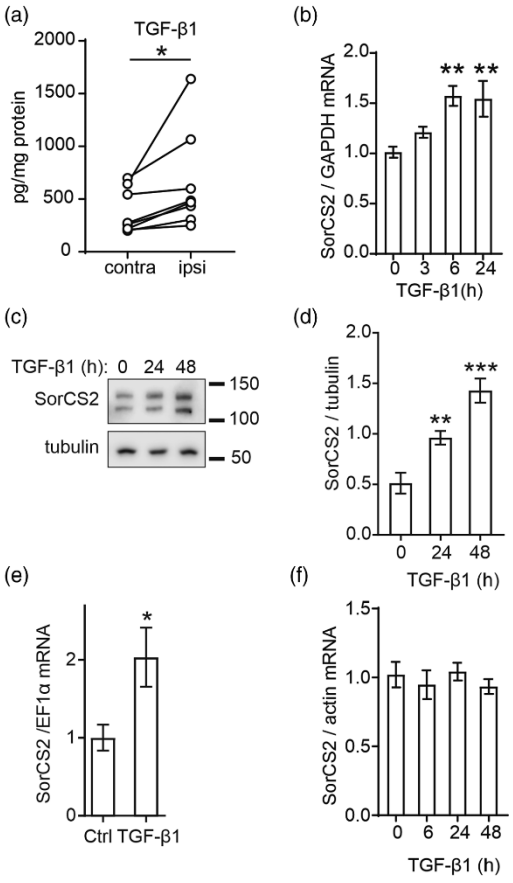

FIGURE 2 TGF-β1 increases after ischemic stroke and induces SorCS2 expression in primary astrocytes. (a) TGF-β1 levels in contralateral (contra) and ipsilateral (ipsi) hemispheres of WT brains at 3 days after MCAo were determined by ELISA and normalized to total protein content. Values obtained for individual mice are presented as connected dots. $n = 7$ mice. *, $p < .05$ in paired t test. (b) Transcript levels of SorCS2 in primary murine astrocytes treated with TGF-β1 (10 ng/ml) for the indicated times were measured by qRT-PCR and given relative to transcript levels of GAPDH. Fold change relative to untreated cells (time = 0, set to 1) is shown. Mean ± *SEM* is indicated. $n = 10$ independent astrocytic preparations. **, $p < .01$ when compared to time = 0 by one-way ANOVA with Dunett's multiple comparisons test. (c) Western blot analysis of SorCS2 levels in primary murine astrocytes treated with TGF-β1 (10 ng/ml) for the indicated times in hours (h). Detection of tubulin serves as a loading control. (d) Quantification of SorCS2 levels normalized to tubulin signal as depicted in (c). $n = 7$ independent astrocytic preparations. **, $p < .01$, ***, $p < .001$ when compared to time = 0 by one-way ANOVA with Dunett's multiple comparisons test. (e) Transcript levels of SorCS2 in cultured human fetal astrocytes treated with TGF-β1 (10 ng/ml) for 24 hr as measured by qRT-PCR and given relative to transcript levels of EF1α. Fold change relative to untreated cells (Ctrl, set to 1) is shown. Mean ± *SEM* is indicated. $n = 6$ samples derived from three donors (two replicates per donor). *, $p < .05$ by unpaired t test. (f) Transcript levels of SorCS2 in primary murine neurons treated with TGF-β1 (10 ng/ml) for the indicated times as measured by qRT-PCR and given relative to transcript levels of actin. Fold change relative to untreated cells (time = 0, set to 1) is shown. Mean ± *SEM* is indicated. $n = 6$ independent neuronal preparations

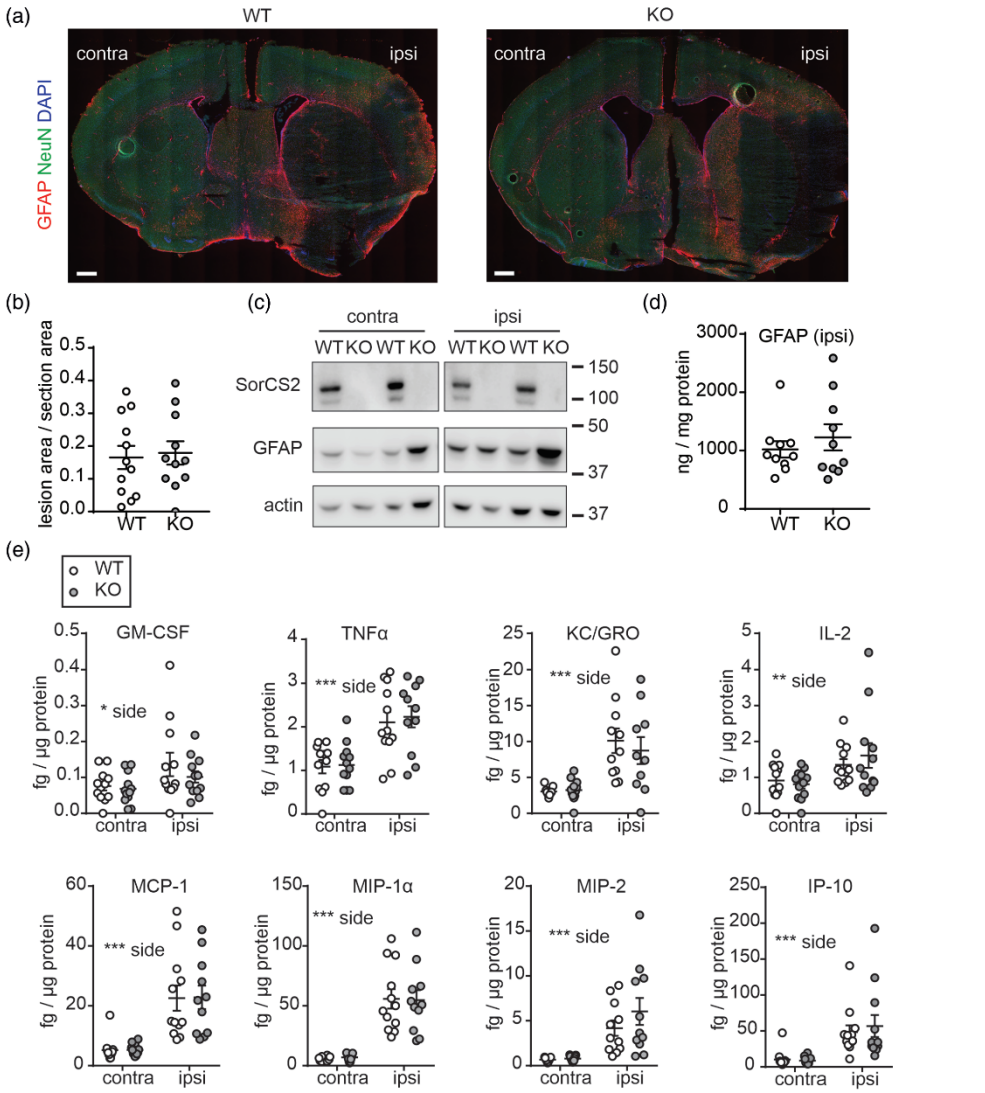

FIGURE 3 Normal glia activation and neuroinflammation in the post-stroke brain of KO mice. (a) Representative images of coronal brain sections of WT and KO mice at 3 days after MCAo. Sections were immunostained for GFAP (red) and NeuN (green), and counterstained with DAPI (blue). The extent of activation of GFAP-labeled astrocytes and the loss of NeuN-positive neurons in the ipsilateral (ipsi) as compared to the contralateral (contra) side is similar in both genotypes. Scale bars, 500 µm. (b) Quantification of the stroke lesion areas on histological sections of WT and KO brains as exemplified in (a). n = 11–12 mice per genotype. Mean ± *SEM* is given. (c) Western blot analysis of GFAP levels in lysates prepared from ipsilateral (ipsi) and contralateral (contra) hemispheres of 2 WT and 2 KO mice 3 days after MCAo. Detection of SorCS2 and actin was used as controls. (d) Levels of GFAP in ipsilateral hemispheres of WT and KO brains 3 days after MCAo were determined by ELISA. GFAP levels were normalized to total protein content. Mean ± *SEM* is indicated. n = 10 mice per genotype. (e) Results of ELISA measurements of cytokines levels in tissue lysates from ipsilateral (ipsi) and contralateral (contra) hemispheres of WT and KO brains 3 days after MCAo. Cytokines levels were normalized to total protein content. n = 12 mice per genotype. Mean ± *SEM* is indicated. *, $p < .05$; **, $p < .01$; ***, $p < .001$ by two-way ANOVA. See Supporting Information Figure S5 for the measurements of additional cytokines in these tissue extracts. GM-CSF, granulocyte-macrophage colony-stimulating factor; TNFα, tumor necrosis factor alpha; KC/GRO, growth-regulated alpha protein; IL-2, interleukin 2; MCP-1, monocyte chemoattractant protein 1; MIP-1α, macrophage inflammatory protein 1-alpha; MIP-2, macrophage inflammatory protein 2; IP-10, interferon gamma-induced protein 10

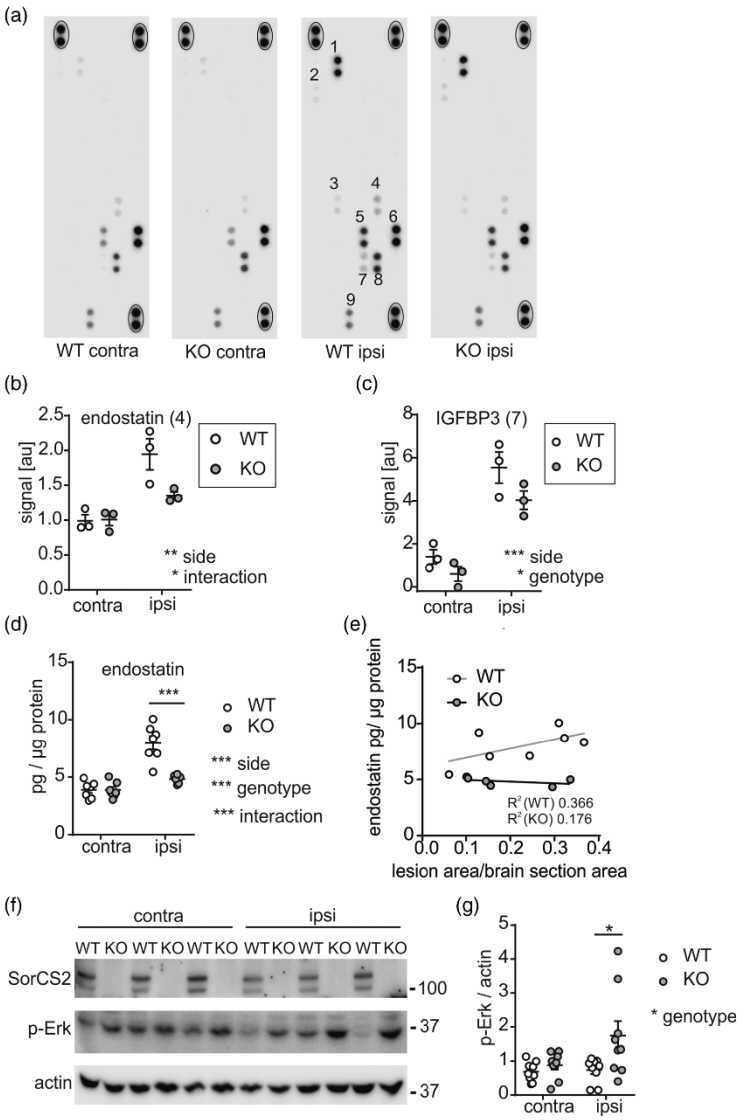

FIGURE 4 Endostatin levels are up-regulated after MCAo in a SorCS2-dependent manner. (a) Representative results of a proteome profiling array performed on ipsilateral (ipsi) and contralateral (contra) brain samples from WT and KO mice 3 days after MCAo. Each protein is detected in duplicate dots. Encircled dots represent positive controls. Selected protein spots are labeled by numbers. 1—osteopontin, 2—serpin E1, 3—CXCL4 (C-X-C motif chemokine 4), 4—endostatin, 5—IGFBP2 (insulin-like growth factor-binding protein 2), 6—coagulation factor III, 7—IGFBP3 (insulin-like growth factor-binding protein 3), 8—FGF1 (fibroblast growth factor 1), 9—CCN3 (CCN family member 3). (b and c) Quantification of signal intensities for endostatin (b; spot 4 in panel (a)) and IGFBP3 (c; spot 7 in panel (a)) obtained in proteome profiling array as depicted in (a). $n = 3$ mice per genotype. Mean ± *SEM* is indicated. *, $p < .05$; **, $p < .01$; ***, $p < .001$ by two-way ANOVA. See Supporting Information Figure S6 for quantifications of signal intensities for additional proteins. (d) Endostatin levels in tissue samples from ipsilateral and contralateral hemispheres of WT and KO mice 3 days after MCAo. Endostatin levels were measured by ELISA and normalized to total protein content in the tissue samples. $n = 6–7$ mice per genotype. Mean ± *SEM* is indicated. ***, $p < .001$ by two-way ANOVA with Tukey's multiple comparisons test. (e) Endostatin levels in the ipsilateral hemispheres in WT and KO mice 3 days after MCAo plotted against the respective stroke lesion sizes. R^2 indicates the goodness of fit for the linear regression. $n = 6–7$ mice per genotype. (f) Representative western blot analysis of p-Erk levels in ipsilateral and contralateral hemispheres of WT and KO mice 3 days after MCAo. Detection of SorCS2 and actin is shown as controls. (g) Quantification of p-Erk levels normalized to actin signal intensities in ipsilateral and contralateral hemispheres of WT and KO brains as depicted in (f). $n = 9$ mice per genotype. Mean ± *SEM* is indicated. *, $p < .05$ by two-way ANOVA with Tukey's multiple comparisons test

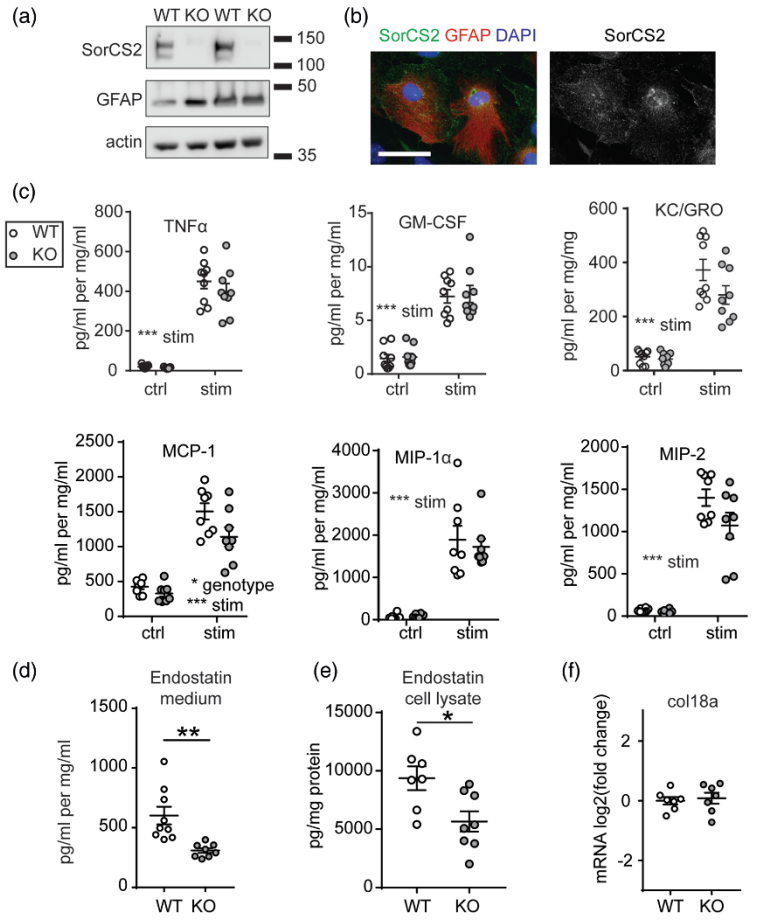

FIGURE 5 SorCS2 controls endostatin release from primary astrocytes. (a) SorCS2 expression in cultured primary astrocytes from WT and KO mice as determined by western blotting. Each lane represents an independent astrocyte preparation. Detection of GFAP and actin was used as loading control. (b) Representative image of immunostaining for SorCS2 (green) in primary cultured astrocytes from WT mice. Cells were co-stained for GFAP (red) and counterstained with DAPI (blue). Combined signals (left) and SorCS2 staining in grayscale (right) are shown. Scale bar, 50 μm. (c) Cytokines levels as determined by ELISA in cell culture medium from primary WT and KO astrocytes either untreated (ctrl) or treated with PMA/ionomycin (stim). Cytokines levels were normalized to the protein content in the respective cell lysates. $n = 9$ independent astrocyte preparations per group. Mean ± *SEM* is indicated. *, $p < .05$; ***, $p < .001$ by two-way ANOVA. See Supporting Information Figure S8 for the measurement of additional cytokines in these samples. TNFα, tumor necrosis factor alpha; GM-CSF, granulocyte-macrophage colony-stimulating factor; KC/GRO, growth-regulated alpha protein; MCP-1, monocyte chemoattractant protein 1; MIP-1α, macrophage inflammatory protein 1-alpha; MIP-2, macrophage inflammatory protein 2. (d) Endostatin levels in cell medium from primary WT or KO astrocyte cultures conditioned for 24 hr. Endostatin levels were quantified by ELISA and normalized to the protein content in the respective cell lysates. $n = 9$ independent astrocyte preparations per genotype. Mean ± *SEM* is indicated. **, $p < .01$ by unpaired *t* test. (e) Endostatin levels in cell lysates from primary WT or KO astrocyte cultures were measured by ELISA and normalized to the protein content. $n = 8$ independent astrocyte preparations per genotype. Mean ± *SEM* is indicated. *, $p < .05$ by unpaired *t* test. (f) Transcript levels of the endostatin precursor collagen 18a in astrocyte cell lysates as measured by qRT-PCR and given relative to transcript levels of actin. Log_2(fold change) relative to WT is shown. Mean ± *SEM* is indicated. $n = 7$ independent astrocyte preparations per genotype

the brain, as no changes in plasma endostatin levels were seen in affected WT animals (Supporting Information Figure S7). Endostatin acts on target cells through interference with signaling pathways, including the mitogen-activated protein kinase pathway (N. Chen, Gao, Yuan, & Zhao, 2016; Sudhakar et al., 2003). Consistent with this fact, increased endostatin levels in the ipsilateral hemispheres of WTs

corresponded with lower p-Erk levels as compared with the ipsilateral hemispheres of KOs (Figure 4f,g).

To further corroborate the role of astrocytic SorCS2 in endostatin release, we used primary astroglial cultures that express SorCS2 when kept in serum-supplemented medium (Figure 5a,b). Substantiating our findings from the MCAo experiments, SorCS2-deficient astrocytes were able to normally secret multiple cytokines after PMA/ionomycin stimulation when compared with WT cells (Figure 5c and Supporting Information Figure S8). However, their ability to release endostatin was significantly impaired (Figure 5d). Endostatin levels were also lower in cell lysates from KO as compared with WT astrocytes (Figure 5e). In conclusion, astrocytes were able to produce and release endostatin in a process that depended on SorCS2. Transcript levels of the endostatin precursor collagen XVIII were not different between

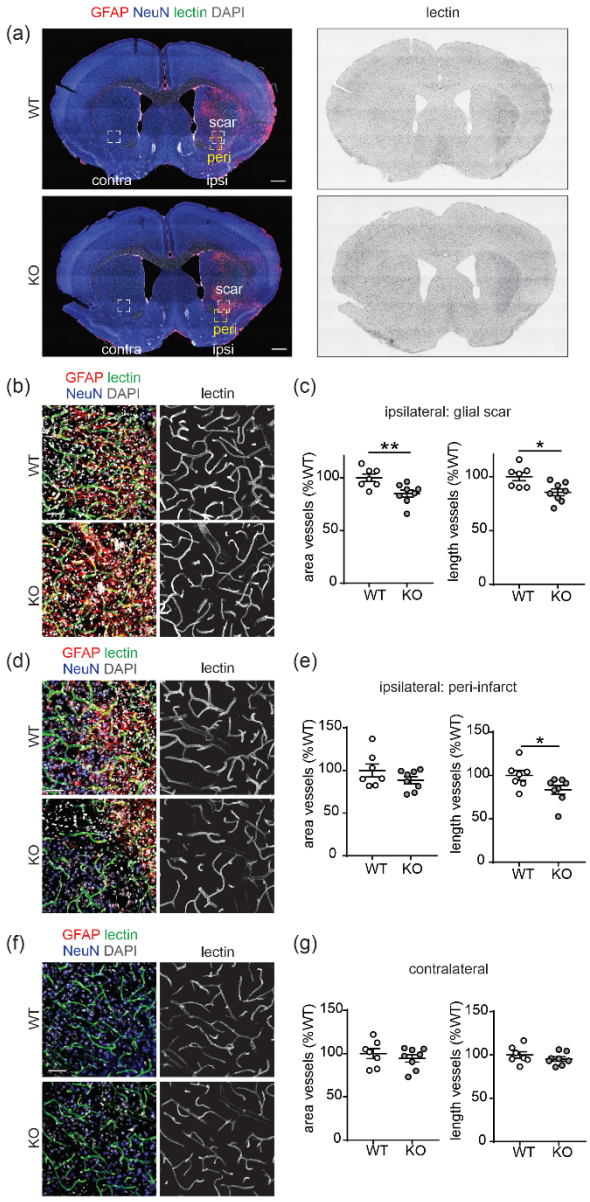

FIGURE 6 SorCS2 deficiency impairs post-stroke angiogenesis. (a) Representative images of coronal brain sections of WT and KO mice 21 days after MCAo. Mice were injected with DyLight488-lectin (green) to visualize blood vessels. In addition, the sections were immunostained for GFAP (red; astrocytes) and NeuN (blue; neurons) and counterstained with DAPI (grayscale). Left panels show combined signals for all channels, while right panels show DyLight488-lectin signal in grayscale. Dashed lines indicate regions analyzed in (b–g); scar, glial scar region; peri, peri-infarct region. Scale bars, 500 µm. (b) Representative images of glial scar regions in ipsilateral hemispheres of WT and KO mice brains as indicated in (a). Maximum intensity projections of confocal *z*-sections are shown. Scale bar, 50 µm. (c) Quantification of brain areas covered by vessels and vessels length in the glial scar region of WT and KO brains 21 days after MCAo (as depicted in (b)). $n = 7–8$ mice per genotype. Mean ± *SEM* is indicated. *, $p < .05$; **, $p < .01$ by unpaired *t* test. (d) Representative images of peri-infarct regions in ipsilateral hemispheres of WT and KO mice brains as indicated in (a). Maximum intensity projections of confocal *z*-sections are shown. Scale bar, 50 µm. (e) Quantification of brain areas covered by vessels and vessels length in the peri-infarct regions of WT and KO brains 21 days after MCAo (as depicted in (d)). $n = 7–8$ mice per genotype. Mean ± *SEM* is indicated. *, $p < .05$ by unpaired *t* test. (f) Representative images of contralateral hemispheres of WT and KO mouse brains as indicated in (a). Maximum intensity projections of confocal *z*-sections are shown. Scale bar, 50 µm. (g) Quantification of brain areas covered by vessels and vessels length in contralateral hemispheres of WT and KO brains 21 days after MCAo (as depicted in (f)). $n = 7–8$ mice per genotype. Mean ± *SEM* is indicated

the genotypes, suggesting a post-transcriptional mechanism of SorCS2-controlled endostatin release from astrocytes (Figure 5f).

3.4 | SorCS2-dependent release of endostatin promotes post-stroke angiogenesis

Next, we explored the consequence of SorCS2-induced production of endostatin for post-stroke angiogenesis. To do so, we injected WT and KO mice at 21 days after MCAo with DyLight 488-labeled lectin to mark functional vessels (Figure 6a). This time point is commonly used to study revascularization of the post-stroke murine brain (J.-Y. Chen et al., 2017; Rust et al., 2019).

Ischemic stroke triggers angiogenesis in areas adjacent to the lesion (Hayashi, Noshita, Sugawara, & Chan, 2003; Krupinski, Kaluza, Kumar, Kumar, & Wang, 1994). In line with this concept, blood vessels length was increased in the glial scar region in the WT brains, as compared with the contralateral side (Supporting Information Figure S9). However, this response was not seen in KO brains (Supporting Information Figure S9). More detailed analysis revealed that the length of the vessels but also the overall area covered by vessels were significantly reduced in the glial scar area in KO mice as compared with WTs (Figure 6b,c). A statistically significant decrease in vessel length in KO as compared with WT brains was also seen in the peri-infarct area (Figure 6d,e). No differences in vessel length and coverage were seen comparing the contralateral hemispheres of WT and KO mice (Figure 6f,g), strongly arguing that SorCS2 deficiency does not influence blood vessels formation during ontogeny but only during post-stroke angiogenesis. In summary, we uncovered a link between SorCS2 activity, endostatin release, and angiogenesis in the post-ischemic brain.

4 | DISCUSSION

Astrocytes are crucial players in stroke pathogenesis (reviewed in Pekny et al., 2016). We now show that activated astrocytes surrounding the ischemic core induce expression of SorCS2, a remarkable finding considering that expression of this sorting receptor in the brain has so far only been reported in neurons. Possibly, induction of SorCS2 expression in astrocytes is a pathophysiological response to increased levels of TGF-β1 in the post-stroke brain, which induces receptor gene transcription in astrocytes but not in neurons. While activated astrocytes define both infarct size and post-lesion recovery in stroke, SorCS2 deficiency had no impact on the ischemic lesion size. Instead, SorCS2 appears to have a specialized role in promoting post-stroke tissue regeneration, in particular in angiogenesis. While we cannot rule out with certainty that neuronal activities of SorCS2 may contribute to post-stroke phenotypes, all of our findings strongly argue that its role in recovery after ischemic insult depends on astrocytic expression of the receptor.

Given the prominent role of astrocytes in the inflammatory brain response, an impact of SorCS2 on their ability to release cytokines may have been anticipated. Such a function had been shown for the related VPS10P domain receptor sortilin in T-cells (Herda et al., 2012). However, cytokine profiling in mouse brains and in activated primary astrocytes failed to document any SorCS2-dependent alterations. Rather, our studies uncovered the ability of SorCS2 to facilitate production and/or release of endostatin from this cell type. Endostatin is cleaved from its precursor collagen XVIII by various proteases, including cathepsins and metalloproteinases (Felbor et al., 2000; Ferreras, Felbor, Lenhard, Olsen, & Delaissé, 2000; Ma et al., 2007). To date, it is not clear which protease plays the major role in generating endostatin in vivo and whether processing takes place intracellularly or in the extracellular space. Thus, we can only speculate by what mechanism SorCS2 promotes endostatin production. Other VPS10P domain receptors sort cathepsins (Canuel, Korkidakis, Konnyu, & Morales, 2008), and SorCS2 may have a similar function in astrocytes to control proteolysis of collagen XVIII by these proteases.

Because of the decisive role of endostatin in formation of new blood vessels, it is tempting to speculate that impaired post-stroke angiogenesis in SorCS2-deficient mice may be causally linked to altered endostatin release from astrocytes in these mice. Endostatin blocks extracellular matrix-dependent motility and morphogenesis in numerous cell types (Kuo et al., 2001). Its anti-proliferative and anti-migratory effects on endothelial cells profoundly inhibit angiogenesis in tumor models (O'Reilly et al., 1997). Long-term treatment with endostatin abolishes the pro-angiogenic effects of physical activity in post-stroke mice (Gertz et al., 2006). In humans, high plasma levels of endostatin after stroke predict a worse long-term functional outcome (Navarro-Sobrino et al., 2011). We now show an increase in endogenous endostatin levels in the ischemic brain as a physiological response acutely after stroke (Figure 4). A similar surge in endostatin levels after stroke has been observed by others in rats (Hou et al., 2010) and rabbits (Tian, Chen, Cui, Xu, & Zhou, 2007). Increased post-stroke release of endostatin seems counterintuitive given the need of the injured brain to grow new vessels. However, previous studies indicated that the levels of both pro- and anti-angiogenic factors are induced after stroke and that these factors show dynamically regulated expression profiles (Hayashi et al., 2003). For example, levels of the angiogenesis inhibitor thrombospondin-1 transiently decrease 1 day after stroke to increase at 3 days post-ischemia. These findings highlight important temporal aspects of orchestrating post-stroke angiogenesis, and suggest crucial roles for anti-angiogenic factors, such as endostatin and thrombospondin-1, in assuring proper angiogenesis. Although the exact role of anti-angiogenic factors in recovery from ischemia still needs further clarification, this hypothesis receives strong support from our findings that revascularization is reduced in SorCS2 mutant brains.

ACKNOWLEDGMENTS

We are indebted to Andra Eisenmann, Kristin Kampf, and Maria Kahlow for expert technical assistance. Funding was provided by the European Research Council (BeyOND No. 335692) to T.E.W., by the Deutsche Forschungsgemeinschaft to C.J.H. (HO5177/3-1), C.H. (HA5741/5-1) and to M.T.C.K. (Berlin-Brandenburg School for

Regenerative Therapies GSC 203), by the Berlin Institute of Health (TRG7), and by the German Federal Ministry of Education and Research (BMBF CSB 01EO1301) to C.H., S.M., P.B.S., U.D., by the BMBF under ERA-NET NEURON scheme (01EW1811) to P.B.S., by the Foundation for Polish Science co-financed by the European Union under the European Regional Development Fund (Homing program, POIR.04.04.00 00 5CEF/18 00) to A.R.M., and by the Deutsche Forschungsgemeinschaft under Germany's Excellence Strategy—EXC-2049—390688087. C.J.H. is a participant in the Charité Clinical Scientist Program.

CONFLICT OF INTEREST

The authors declare no conflicts of interest.

DATA AVAILABILITY STATEMENT

The authors confirm that the data supporting the findings of this study are available within the article and its Supporting Information.

ORCID

Anna R. Malik https://orcid.org/0000-0001-7732-0756

REFERENCES

Aronica, E., Gorter, J. A., Rozemuller, A. J., Yankaya, B., & Troost, D. (2005). Interleukin-1 beta down-regulates the expression of metabotropic glutamate receptor 5 in cultured human astrocytes. *Journal of Neuroimmunology*, *160*(1–2), 188–194. https://doi.org/10.1016/j.jneuroim.2004.11.015

Canuel, M., Korkidakis, A., Konnyu, K., & Morales, C. R. (2008). Sortilin mediates the lysosomal targeting of cathepsins D and H. *Biochemical and Biophysical Research Communications*, *373*(2), 292–297. https://doi.org/10.1016/j.bbrc.2008.06.021

Chen, J.-Y., Yu, Y., Yuan, Y., Zhang, Y.-J., Fan, X.-P., Yuan, S.-Y., … Yao, S.-L. (2017). Enriched housing promotes post-stroke functional recovery through astrocytic HMGB1-IL-6-mediated angiogenesis. *Cell Death Discovery*, *3*, 17054. https://doi.org/10.1038/cddiscovery.2017.54

Chen, N., Gao, R.-F., Yuan, F.-L., & Zhao, M.-D. (2016). Recombinant human endostatin suppresses mouse osteoclast formation by inhibiting the NF-κB and MAPKs signaling pathways. *Frontiers in Pharmacology*, *7*, 145. https://doi.org/10.3389/fphar.2016.00145

Chen, Z.-Y., Ieraci, A., Teng, H., Dall, H., Meng, C.-X., Herrera, D. G., … Lee, F. S. (2005). Sortilin controls intracellular sorting of brain-derived neurotrophic factor to the regulated secretory pathway. *The Journal of Neuroscience: The Official Journal of the Society for Neuroscience*, *25*(26), 6156–6166. https://doi.org/10.1523/JNEUROSCI.1017-05.2005

Dirnagl, U., & Members of the MCAO-SOP Group. (2012). Standard operating procedures (SOP) in experimental stroke research: SOP for middle cerebral artery occlusion in the mouse. *Nature Precedings*. https://doi.org/10.1038/npre.2012.3492.3

Felbor, U., Dreier, L., Bryant, R. A., Ploegh, H. L., Olsen, B. R., & Mothes, W. (2000). Secreted cathepsin L generates endostatin from collagen XVIII. *The EMBO Journal*, *19*(6), 1187–1194. https://doi.org/10.1093/emboj/19.6.1187

Ferreras, M., Felbor, U., Lenhard, T., Olsen, B. R., & Delaissé, J.-M. (2000). Generation and degradation of human endostatin proteins by various proteinases. *FEBS Letters*, *486*(3), 247–251. https://doi.org/10.1016/S0014-5793(00)02249-3

Gertz, K., Priller, J., Kronenberg, G., Fink, K. B., Winter, B., Schröck, H., … Endres, M. (2006). Physical activity improves long-term stroke outcome via endothelial nitric oxide synthase-dependent augmentation of neovascularization and cerebral blood flow. *Circulation Research*, *99*(10), 1132–1140. https://doi.org/10.1161/01.RES.0000250175.14861.77

Glerup, S., Olsen, D., Vaegter, C. B., Gustafsen, C., Sjoegaard, S. S., Hermey, G., … Nykjaer, A. (2014). SorCS2 regulates dopaminergic wiring and is processed into an apoptotic two-chain receptor in peripheral glia. *Neuron*, *82*(5), 1074–1087. https://doi.org/10.1016/j.neuron.2014.04.022

Hayashi, T., Noshita, N., Sugawara, T., & Chan, P. H. (2003). Temporal profile of angiogenesis and expression of related genes in the brain after ischemia. *Journal of Cerebral Blood Flow & Metabolism*, *23*(2), 166–180. https://doi.org/10.1097/01.WCB.0000041283.53351.CB

Herda, S., Raczkowski, F., Mittrücker, H.-W., Willimsky, G., Gerlach, K., Kühl, A. A., … Rehm, A. (2012). The sorting receptor Sortilin exhibits a dual function in exocytic trafficking of interferon-γ and granzyme A in T cells. *Immunity*, *37*(5), 854–866. https://doi.org/10.1016/j.immuni.2012.07.012

Hou, Q., Ling, L., Wang, F., Xing, S., Pei, Z., & Zeng, J. (2010). Endostatin expression in neurons during the early stage of cerebral ischemia is associated with neuronal apoptotic cell death in adult hypertensive rat model of stroke. *Brain Research*, *1311*, 182–188. https://doi.org/10.1016/j.brainres.2009.11.033

Kaplan, R. C., Petersen, A.-K., Chen, M.-H., Teumer, A., Glazer, N. L., Döring, A., … Wallaschofski, H. (2011). A genome-wide association study identifies novel loci associated with circulating IGF-I and IGFBP-3. *Human Molecular Genetics*, *20*(6), 1241–1251. https://doi.org/10.1093/hmg/ddq560

Krupinski, J., Kaluza, J., Kumar, P., Kumar, S., & Wang, J. M. (1994). Role of angiogenesis in patients with cerebral ischemic stroke. *Stroke*, *25*(9), 1794–1798. https://doi.org/10.1161/01.str.25.9.1794

Kuo, C. J., LaMontagne, K. R., Garcia-Cardeña, G., Ackley, B. D., Kalman, D., Park, S., … Javaherian, K. (2001). Oligomerization-dependent regulation of motility and morphogenesis by the collagen XVIII Nc1/endostatin domain. *The Journal of Cell Biology*, *152*(6), 1233–1246. https://doi.org/10.1083/jcb.152.6.1233

Ma, D. H.-K., Yao, J.-Y., Kuo, M.-T., See, L.-C., Lin, K.-Y., Chen, S.-C., … Lin, K.-K. (2007). Generation of endostatin by matrix metalloproteinase and cathepsin from human limbocorneal epithelial cells cultivated on amniotic membrane. *Investigative Ophthalmology & Visual Science*, *48*(2), 644–651. https://doi.org/10.1167/iovs.06-0884

Malik, A. R., Szydlowska, K., Nizinska, K., Asaro, A., van Vliet, E. A., Popp, O., … Willnow, T. E. (2019). SorCS2 controls functional expression of amino acid transporter EAAT3 and protects neurons from oxidative stress and epilepsy-induced pathology. *Cell Reports*, *26*(10), 2792–2804.e6. https://doi.org/10.1016/j.celrep.2019.02.027

Meng, H., Song, Y., Zhu, J., Liu, Q., Lu, P., Ye, N., … Wu, H. (2016). LRG1 promotes angiogenesis through upregulating the TGF-β1 pathway in ischemic rat brain. *Molecular Medicine Reports*, *14*(6), 5535–5543. https://doi.org/10.3892/mmr.2016.5925

Navarro-Sobrino, M., Rosell, A., Hernández-Guillamon, M., Penalba, A., Boada, C., Domingues-Montanari, S., … Montaner, J. (2011). A large screening of angiogenesis biomarkers and their association with neurological outcome after ischemic stroke. *Atherosclerosis*, *216*(1), 205–211. https://doi.org/10.1016/j.atherosclerosis.2011.01.030

O'Reilly, M. S., Boehm, T., Shing, Y., Fukai, N., Vasios, G., Lane, W. S., … Folkman, J. (1997). Endostatin: An endogenous inhibitor of angiogenesis and tumor growth. *Cell*, *88*(2), 277–285. https://doi.org/10.1016/S0092-8674(00)81848-6

Pardali, E., Goumans, M.-J., & ten Dijke, P. (2010). Signaling by members of the TGF-β family in vascular morphogenesis and disease. *Trends in Cell Biology*, *20*(9), 556–567. https://doi.org/10.1016/j.tcb.2010.06.006

Parnis, J., Montana, V., Delgado-Martinez, I., Matyash, V., Parpura, V., Kettenmann, H., … Nolte, C. (2013). Mitochondrial exchanger NCLX plays a major role in the intracellular Ca2+ signaling, gliotransmission,

and proliferation of astrocytes. *Journal of Neuroscience*, *33*(17), 7206–7219. https://doi.org/10.1523/JNEUROSCI.5721-12.2013

Pekny, M., Pekna, M., Messing, A., Steinhäuser, C., Lee, J.-M., Parpura, V., … Verkhratsky, A. (2016). Astrocytes: A central element in neurological diseases. *Acta Neuropathologica*, *131*(3), 323–345. https://doi.org/10.1007/s00401-015-1513-1

Ramakers, C., Ruijter, J. M., Deprez, R. H. L., & Moorman, A. F. M. (2003). Assumption-free analysis of quantitative real-time polymerase chain reaction (PCR) data. *Neuroscience Letters*, *339*(1), 62–66. https://doi.org/10.1016/s0304-3940(02)01423-4

Reitz, C. (2015). The role of the retromer complex in aging-related neurodegeneration: A molecular and genomic review. *Molecular Genetics and Genomics: MGG*, *290*(2), 413–427. https://doi.org/10.1007/s00438-014-0939-9

Ruijter, J. M., Ramakers, C., Hoogaars, W. M. H., Karlen, Y., Bakker, O., van den Hoff, M. J. B., & Moorman, A. F. M. (2009). Amplification efficiency: Linking baseline and bias in the analysis of quantitative PCR data. *Nucleic Acids Research*, *37*(6), e45. https://doi.org/10.1093/nar/gkp045

Rust, R., Grönnert, L., Gantner, C., Enzler, A., Mulders, G., Weber, R. Z., … Schwab, M. E. (2019). Nogo-A targeted therapy promotes vascular repair and functional recovery following stroke. *Proceedings of the National Academy of Sciences of the United States of America*, *116*(28), 14270–14279. https://doi.org/10.1073/pnas.1905309116

Sasaki, T., Fukai, N., Mann, K., Göhring, W., Olsen, B. R., & Timpl, R. (1998). Structure, function and tissue forms of the C-terminal globular domain of collagen XVIII containing the angiogenesis inhibitor endostatin. *The EMBO Journal*, *17*(15), 4249–4256. https://doi.org/10.1093/emboj/17.15.4249

Sudhakar, A., Sugimoto, H., Yang, C., Lively, J., Zeisberg, M., & Kalluri, R. (2003). Human tumstatin and human endostatin exhibit distinct antiangiogenic activities mediated by alpha v beta 3 and alpha 5 beta 1 integrins. *Proceedings of the National Academy of Sciences of the United States of America*, *100*(8), 4766–4771. https://doi.org/10.1073/pnas.0730882100

Tian, H.-L., Chen, H., Cui, Y.-H., Xu, T., & Zhou, L.-F. (2007). Increased protein and mRNA expression of endostatin in the ischemic brain tissue of rabbits after middle cerebral artery occlusion. *Neuroscience Bulletin*, *23*(1), 35–40. https://doi.org/10.1007/s12264-007-0005-2

Vaegter, C. B., Jansen, P., Fjorback, A. W., Glerup, S., Skeldal, S., Kjolby, M., … Nykjaer, A. (2011). Sortilin associates with Trk receptors to enhance anterograde transport and neurotrophin signaling. *Nature Neuroscience*, *14*(1), 54–61. https://doi.org/10.1038/nn.2689

Willnow, T. E., Petersen, C. M., & Nykjaer, A. (2008). VPS10P-domain receptors—Regulators of neuronal viability and function. *Nature Reviews. Neuroscience*, *9*(12), 899–909. https://doi.org/10.1038/nrn2516

Yan, J., Greer, J. M., & McCombe, P. A. (2012). Prolonged elevation of cytokine levels after human acute ischaemic stroke with evidence of individual variability. *Journal of Neuroimmunology*, *246*(1), 78–84. https://doi.org/10.1016/j.jneuroim.2012.02.013

Zhang, C., Zhu, Y., Wang, S., Zachory Wei, Z., Jiang, M. Q., Zhang, Y., … Wei, L. (2018). Temporal gene expression profiles after focal cerebral ischemia in mice. *Aging and Disease*, *9*(2), 249–261. https://doi.org/10.14336/AD.2017.0424

Zhu, H., Gui, Q., Hui, X., Wang, X., Jiang, J., Ding, L., … Chen, H. (2017). TGF-β1/Smad3 signaling pathway suppresses cell apoptosis in cerebral ischemic stroke rats. *Medical Science Monitor*, *23*, 366–376. https://doi.org/10.12659/MSM.899195

SUPPORTING INFORMATION

Additional supporting information may be found online in the Supporting Information section at the end of this article.

How to cite this article: Malik AR, Lips J, Gorniak-Walas M, et al. SorCS2 facilitates release of endostatin from astrocytes and controls post-stroke angiogenesis. *Glia*. 2020;68:1304–1316. https://doi.org/10.1002/glia.23778

Research Article

Refining Humane Endpoints in Mouse Models of Disease by Systematic Review and Machine Learning-Based Endpoint Definition

Jie Mei[1], *Stefanie Banneke*[2], *Janet Lips*[1,3,4], *Melanie T. C. Kuffner*[1,4,5], *Christian J. Hoffmann*[1,4,6], *Ulrich Dirnagl*[1,3,4,7,8], *Matthias Endres*[1,4,6,7,8], *Christoph Harms*[1,3,4,6] *and Julius V. Emmrich*[1,2,6]

[1]Department of Neurology and Department of Experimental Neurology, Neurocure Cluster of Excellence, Charité – Universitätsmedizin Berlin, corporate member of Freie Universität Berlin, Humboldt Universität zu Berlin, and Berlin Institute of Health, Berlin, Germany; [2]German Federal Institute for Risk Assessment, German Center for the Protection of Laboratory Animals (Bf3R), Berlin, Germany; [3]QUEST – Center for Transforming Biomedical Research, Berlin Institute of Health (BIH); [4]Center for Stroke Research, Charité – Universitätsmedizin Berlin, Berlin, Germany; [5]Berlin-Brandenburg School for Regenerative Therapies (BSRT), Berlin, Germany; [6]Berlin Institute of Health (BIH), Berlin, Germany; [7]German Center for Neurodegenerative Diseases (DZNE), Berlin, Germany; [8]German Center for Cardiovascular Research (DZHK), Berlin, Germany

Abstract

Ideally, humane endpoints allow early termination of experiments by minimizing an animal's discomfort, distress and pain while ensuring that scientific objectives are reached. Yet, lack of commonly agreed methodology and heterogeneity of cut-off values published in the literature remain a challenge to the accurate determination and application of humane endpoints.

With the aim to synthesize and appraise existing humane endpoint definitions for commonly used physiological parameters, we conducted a systematic review of mouse studies of acute and chronic disease models that used body weight, temperature and/or sickness scores for endpoint definition. We searched for studies in two electronic databases (MEDLINE/Pubmed and Embase). Out of 110 retrieved full-text manuscripts, 34 studies were included. We found large intra- and inter-model variance in humane endpoint determination and application due to varying animal models, lack of standardized experimental protocols, and heterogeneity of performance metrics (part 1).

We then used previously published and unpublished data on weight, temperature, and sickness scores from mouse models of sepsis and stroke and applied machine learning models to assess the usefulness of this method for parameter selection and endpoint definition across models. Machine learning models trained with physiological data and sickness severity score or modified DeSimoni neuroscore identified animals with a high risk of death at an early time point in both mouse models of stroke (male: 93.2% at 72 h post-treatment; female: 93.0% at 48 h post-treatment) and sepsis (96.2% at 24 h post-treatment), thus demonstrating generalizability of endpoint determination across models (part 2).

1 Introduction

In experimental mouse studies an important challenge for researchers is to identify an endpoint by which the experiment shall be terminated in order to minimize unnecessary suffering of animals without compromising the quality of the experimental data. To systematically address this challenge, the concept of humane endpoints was introduced almost 20 years ago in Europe (OECD, 2000). The application of humane endpoints describes the use of clear, predictable, and irreversible criteria, which can be used as a substitute for a more severe experimental outcome such as extreme suffering or death. Systematic implementation of humane endpoints can prevent or reduce pain and/or suffering whilst still meeting experimental objectives (Nemzek et al., 2004).

Thus, application of humane endpoints is a key component of refining studies to comply with 3R principles. In models of acute disease, death may occur within hours following an experimental intervention, which requires both intensive follow-up and consis-

Received December 23, 2018; Accepted April 10, 2019;
Epub April 18, 2019;

ALTEX 36(4), 555-571. doi:10.14573/altex.1812231

Correspondence: Julius Emmrich, Charité Universitätsmedizin Berlin, Department of Neurology and Department of Experimental Neurology, Charitéplatz 1, 10117 Berlin, Germany
(julius.emmrich@charite.de)
or Christoph Harms, Center for Stroke Research, Department of Experimental Neurology, Charitéplatz 1, 10117 Berlin, Germany
(christoph.harms@charite.de)

tency in endpoint determination. However, the varying nature of animal models and disease progression, lack of reporting these details in the literature, lack of standardized evaluation protocols, and heterogeneity of endpoints published in the literature make it difficult to accurately determine and apply humane endpoints (Franco et al., 2012).

So far, various approaches to humane endpoint evaluation have been proposed. These are based on physiological parameters such as body weight, temperature, or standardized sickness scores. Most commonly, analysis is conducted in a non-comprehensive manner, e.g., by arbitrary selection of a parameter and a cut-off value corresponding to the highest mortality rate or best separation between treated and sham-treated animals. However, these approaches often require manual, time-consuming computation and are prone to inter-observer bias. Machine learning, a technique used to identify underlying patterns from given datasets to produce reliable, repeatable predictions, has been applied in a number of different animal studies to classify individual/social behaviors (Kabra et al., 2013), automatize behavior analysis (Han et al., 2018), or to identify behavioral strategies and decision-making processes (Yamaguchi et al., 2018). To our knowledge, using machine learning methods for humane endpoint characterization has not yet been systematically assessed.

The aim of the present study therefore was twofold: first, to identify and appraise existing humane endpoint definitions in mouse models of acute and chronic disease by conducting a systematic review of studies using weight, body temperature, and/or sickness scores for humane endpoint refinement and evaluation, and second, to examine the potential usefulness and accuracy of using machine learning with an automated parameter search to automatically define humane endpoints. To maximize generalizability of results, we used previously published and unpublished data from two independent mouse models of acute disease, namely, a middle cerebral artery occlusion (MCAo) stroke model and a lipopolysaccharide (LPS)-induced systemic inflammation model, respectively (Donath et al., 2016; Mei et al., 2018).

We found great heterogeneity of published cut-off criteria and thresholds, illustrating a distinct difficulty in adopting humane endpoints from the literature. However, we show that machine learning can be used to accurately determine humane endpoint criteria and cut-off threshold values at early time points following stroke or systemic inflammation thus potentially reducing otherwise unnecessary suffering.

2 Animals, materials, and methods

2.1 Systematic review

2.1.1 Search strategy

Studies were identified, screened and extracted for relevant data following the PRISMA (Preferred Reporting Items for Systematic Reviews and Meta-Analyses) guidelines (http://www.prisma-statement.org). Literature search, title and abstract screening was conducted by JM. Full text screening was conducted by JM and JVE. A search was conducted on the MEDLINE/PubMed databases for all research articles from 1946 to Feb 07, 2018 using the following Boolean string with Medical Subject Headings (MeSH): (("Mice"[Mesh]) AND ("Endpoint Determination"[Mesh] OR "Animal Use Alternatives"[Mesh] OR humane endpoint* OR humane end point* OR surrogate endpoint* OR surrogate end point* OR thermometry OR thermometer OR telemetry OR refinement OR welfare) AND ("Body Weight"[Mesh] OR "Body Temperature"[Mesh] OR body temperature OR weight NOT fetal NOT fetus OR score* OR scoring)), and on the Embase database for all research articles from 1947 to Feb 07, 2018 using EMBASE Thesaurus (EMTREE) with Boolean string: (exp mice) and (exp Body Temperature or exp Body Weight or (score$ or scoring) or body temperature or (weight not fetal not fetus)) and (humane end point$ or humane endpoint$ or surrogate end point$ or surrogate endpoint$ or (thermometry or thermometer or telemetry) or (welfare or refinement)).

2.1.2 Exclusion and inclusion criteria

Studies that fulfilled the following inclusion criteria were included in the systematic review: (a) original research articles on mouse models of acute and/or chronic disease, (b) physiological parameters such as body temperature, body weight, or sickness severity scores were used individually or in combination to identify and/or evaluate humane endpoints, and (c) studies that applied pre-defined humane endpoints determined from body temperature, body weight, or sickness severity scores.

Irrelevant studies were excluded if: (a) subjects used were other than mice, (b) article was a conference abstract, experimental protocol, or review, (c) article was written in a language other than English, (d) parameters used to determine humane endpoints were other than body temperature, body weight, or sickness severity scores, and (e) no humane endpoints were applied in the course of experiments or if the study was unrelated to humane endpoint determination.

2.1.3 Extraction of relevant data

Relevant data was extracted and compared through a data extraction sheet. Extraction procedure was conducted by JM. Extracted data included (a) disease model, (b) sample size, (c) time course of the experiment, (d) frequency of evaluation/measurement, (e) humane endpoint(s) used/proposed, (f) cut-off criteria for euthanasia, (g) metrics for evaluating the humane endpoint(s), and (h) performance of the humane endpoint(s). When multiple endpoints were applied together in one study, all available descriptions were included. Missing data entries were marked with N/A (not applicable).

2.2 Animal models of stroke and sepsis

2.2.1 Animals

No animals were used for this study. Rather, all data analyzed in this study were sourced from the authors' previously published and unpublished results using a middle cerebral artery occlusion (MCAo) stroke model and a lipopolysaccharide (LPS)-induced systemic inflammation model, respectively (Hoffmann et al., 2015; Donath et al., 2016; Koch et al., 2017; Emmrich et al.,

Tab. 1: Strain and origin of animals used for automated parameter search to define humane endpoints for (A) middle cerebral artery occlusion (MCAo) stroke model, and (B) lipopolysaccharide (LPS)-induced sepsis model
m, male; f, female

A

Strain	n	Origin
C57BL/6NCrl	74 (m: 74)	Charles River Laboratories
Tg(Gjb6-cre/ERT2)53-33Fwp [MGI:4420273] x custom-made Tg(ROSA26-FLEX IL6)1Ch	166 (m: 85; f: 81)	F. Pfrieger; Charité Universitätsmedizin Berlin; Research Institutes for Experimental Medicine
C57BL/6N-Zfp580$^{tm1a(EUCOMM)Hmgu}$/BayMmucd	158 (m: 84; f: 74)	Charité Universitätsmedizin Berlin; Research Institutes for Experimental Medicine
Tg(Cdh5-cre/ERT2)1Rha x custom-made Tg(ROSA26-FLEX IL6)1Ch	33 (m: 16; f: 17)	R. Adams; Charité Universitätsmedizin Berlin; Research Institutes for Experimental Medicine
Sorcs2tm1Anyk [MGI:5649357]	56 (m: 56)	

B

Strain	n	Origin
C57BL/6J	55 (f)	Charles River Laboratories
Mertk (*B6;129-Mertk^{tm1Grl}/J*)	126 (f)	The Jackson Laboratory
Cd11b (B6;129-Mertk^{tm1Grl}/J, B6.129S4-Itgam^{tm1Myd}/J)	126 (f)	Hertie Institute for Clinical Brain Research
Mfge8	128 (f)	C. Théry, INSERM 932, France

2017; Mei et al., 2018). For the original studies, all experimental procedures were approved by the ethical review committee of *Landesamt für Gesundheit und Soziales* (LaGeSo), Berlin (Reg G0385/08, G0188/11, G0354/11, G0197/12, G005/16, G0057/16, G0119/16, GG254/16, G0157/17, stroke; Reg G239/15, sepsis) and were conducted in accordance with the German animal protection law and local animal welfare guidelines. Reporting of results based on the authors' own historical data complies with the ARRIVE guidelines (Kilkenny et al., 2010) and with the guidelines for genetically modified organisms (441/06). Data from 922 animals were included in this study. All inspections and measurements were performed in the same facility where animals were housed.

For the stroke model, adult male and female mice were used (total: n = 487; Tab. 1a; Slezak et al., 2007; Skarnes et al., 2011; Benedito et al., 2009; Glerup et al., 2014). Seven mice were not assigned to any treatment group (male: 5; female: 2) as they died of natural causes or reached a humane endpoint prior to the start of the experiment. Therefore, 480 out of 487 mice were randomly assigned to a 30 min MCAo (n = 73; male: 53; female: 20), a 45 min MCAo (n = 331; male: 213, female: 118) or a sham procedure (n = 76; male: 44; female: 32), at the age of 8-12 weeks. Mice were housed in groups of up to 12 animals per cage at 22 ±2°C, humidity of 55 ±10%, and a 12-hour light/dark cycle (12:12 h, lights on: 7:00 h, lights off: 19:00 h). Aspen woodchips were used as bedding.

For the sepsis model, female homozygous knockout mice and their homozygous wildtype littermates were used in experiments at the age of 8-10 weeks (total: n = 435; Tab. 1b). Mice were housed in groups of up to 12 animals per cage at 23 ± 1°C, humidity of 60 ± 5%, and a 12-hour light/dark cycle (12:12 h light/dark cycle, lights on: 20:00, lights off: 8:00) and were exposed to white noise at moderate intensity (65dB) during the dark phase (Dohm Sleepmate, Marpac Sound Machines, Wilmington, USA). During acute illness and recovery, mice were housed individually. Wood shavings were used as bedding.

2.2.2 Treatments

Stroke model: Mice were subjected to 30 or 45 minutes temporary filamentous middle cerebral artery occlusion (MCAo) or sham procedure. The filamentous MCAo model was performed as described in Dirnagl et al. (2012). For sham animals, the filament was advanced to the MCA and withdrawn immediately.

Sepsis model: Lipopolysaccharide (LPS) or physiological phosphate-buffered saline solution (PBS) were administered intraperitoneally for the induction of a systemic inflammatory response or control, respectively. The injection was performed as previously described (Mei et al., 2018).

Animals were randomized to treatment groups using the GraphPad calculator tool[1] or Research Randomizer tool[2] for the stroke and sepsis model, respectively. To minimize experimenter bias, randomization was conducted by a researcher who was not

[1] http://www.graphpad.com/quickcalcs/randomize1.cfm
[2] https://www.randomizer.org

involved in injections, treatments, data acquisition or analysis. Information on strain, genotype and treatment group assignment was concealed from experimenters until the end of the study.

2.2.3 Physiological parameters and scoring

In the stroke model, body weight and a modified version of the DeSimoni neuroscore, a composite score of general behavioral alterations and focal motor, sensory, reflex, and balance deficits to evaluate neurological outcome following cerebral ischemia in mice, were obtained as previously described (Donath et al., 2016). Core body temperature was quantified non-invasively using subcutaneous radio-frequency identification (RFID) transponders as described (Donath et al., 2016).

In the sepsis model, a sickness score adapted from the murine sepsis score was obtained based on general activity and response to stimuli as previously described (Mei et al., 2018). Surface body temperature was quantified using two non-contact infrared thermometer models as described previously (Mei et al., 2018). For body weight acquisition, a bench scale (PCB 1000-1, KERN & SOHN GmbH, Balingen, Germany) was used. Animals were weighed once their body and tail were in a plastic box placed on the top of the scale.

In both disease models, the duration of manual handling was minimized to reduce stress and discomfort when examining signs of sickness of experimental animals. Low anxiety handling methods including cupping the animal between both hands and using a handling box were applied. In addition, and only if necessary, animals were lifted by the base of the tail for no longer than 2-3 seconds.

2.2.4 Timeline of physiological monitoring

In the stroke model, baseline body weight and temperature were measured at 7:00-8:00 on the day of MCAo, followed by 2 inspections on the day of surgery and consequent daily inspection for qualitative humane endpoint criteria at 7:00-9:00 until day 28. The modified DeSimoni score for individual animals was assessed on the day of MCAo and on the 1st, 2nd, 7th, 14th, and 21st day post-MCAo as previously described (Donath et al., 2016).

In the sepsis model, baseline temperature and weight were measured at 8:00 on the day of the first injection. Body temperature and sickness score were obtained eight times daily (8:00 to 20:00, every 90 min) on the two consecutive injection days, then three times daily (8:00 to 20:00, every 6 h) for two days after the second injection, and once a day (8:00) from post-injection day 3 until day 30 after the second injection. Body weight was obtained three times daily (8:00 to 20:00, every 6 h) during the two injection days and the first two days following the second injection, then once per day at 8:00 until day 30 after the second injection (Mei et al., 2018). To avoid stress-induced fluctuations in body temperature, animals were weighed after body temperature acquisition.

Body temperature, body weight, and sickness score were assessed for 21 or 30 days post-MCAo or LPS/PBS injection, respectively. In accordance with the aim of the study, data from time points later than that of the death of the last animal in each experiment was not included.

2.2.5 Humane endpoint criteria

In the stroke model, animals were euthanized by cervical dislocation upon reaching a score of 2 of the 2nd criteria, or a score of 3 or 4 of the 3rd-12th criteria in the modified DeSimoni neuroscore (Donath et al., 2016). In addition to the score-based criteria, animals were euthanized when a loss of more than 20% baseline body weight occurred or the following qualitative humane endpoint criteria were observed during inspection: complete paralysis with absence of spontaneous movement, severe ataxia or loss of postural reflexes, severe epileptic seizures, severe reduction of general health status with reduced grooming or refusal of food intake.

In the sepsis model, upon reaching a sickness score greater than 4 once or a score of 4 twice within 2 hours, animals were immediately removed from the cage and euthanized by cervical dislocation (Mei et al., 2018).

2.2.6 Exclusion criteria

In the stroke model, animals that were (a) attacked by littermates before or during the experiment (n = 8); (b) failed to learn the behavioral task prior to MCAo (n = 9); (c) died during or within the first hour after anesthesia as a result of surgical complications (n = 12); (d) euthanized on the day of surgery (n = 1); (e) euthanized after the 30th day post-MCAo (n = 7); and (f) of a baseline temperature < 32°C (n = 4), were not included in subsequent analysis, leading to exclusion of 41 out of 487 animals (8.4%).

In the sepsis model, no animal was excluded.

2.2.7 Data analysis and statistics

Results are expressed as mean (SD) unless otherwise specified. Data processing and statistical analysis was performed using SPSS version 24 (SPSS Inc., Chicago, IL, USA) and Python 2.7.10 (Python Software Foundation, Beaverton, OR, USA). Risk of death as an outcome event was evaluated with the scikit-learn toolkit (sklearn; Pedregosa et al., 2011) for physiological parameters including core body temperature, surface body temperature, body weight and modified DeSimoni neuroscore or sickness severity score.

A primary aim of this study was to identify physiological parameters that can be used to separate animals that are at a higher risk of death from animals that would reach the planned experimental endpoint. Therefore, apart from assessing the prediction accuracy of various models, we also identified the predictive power of physiological parameters, individually or in combination. To assess and identify (a) general performance of machine learning models, (b) usability of physiological parameters obtained at different time points in death prediction, and (c) model hyperparameters, grid search with stratified 3-fold cross-validation was applied. Core temperature (stroke model), surface temperature (sepsis model), body weight (both models), sickness score (sepsis model) or modified DeSimoni neuroscore (stroke model), and the absolute change of these parameters per timepoint (calculated by subtracting the baseline value from the measured value at a given timepoint) were used individually or in combination to train machine learning models. Models used for this study included logistic regression, Gaussian Naïve Bayes, decision tree (of max_depth = 1, 2, 3, or 4), support vector machine (with linear or radial basis function (RBF) kernels; C = 1,

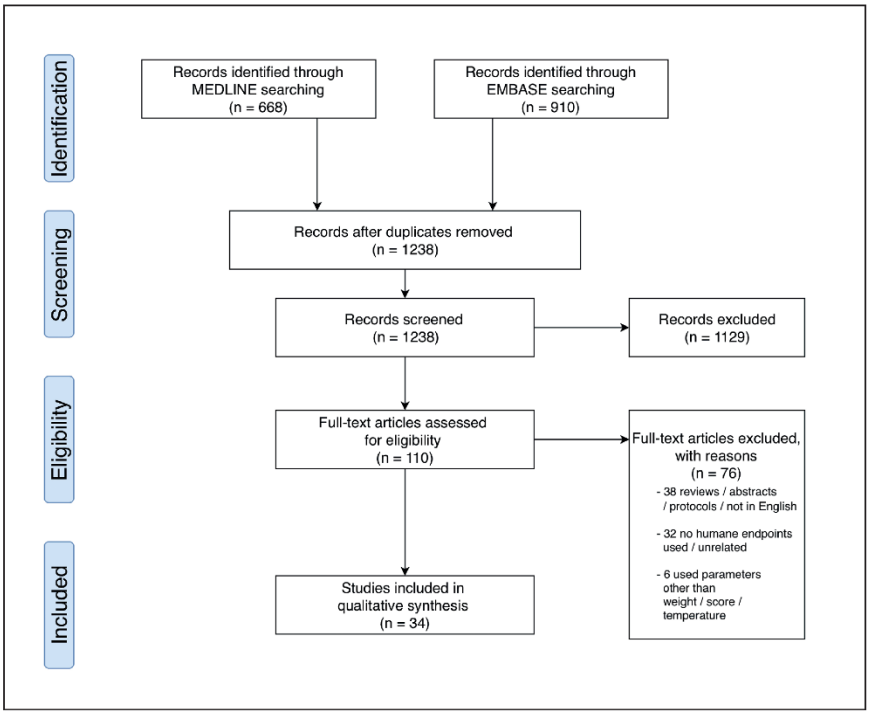

Fig. 1: Flow diagram showing the number of studies identified, screened, extracted and included in this systematic review

10, or 100; gamma = 0.01, 0.001, or 0.0001), and random forest classifier (with n_estimators = 2, 4, or 8).

Available data from all time points before the average time of death of non-survivor animals was included in the analysis. First, to reduce complexity of the analysis and enhance the applicability of the method, measurements obtained at the same time point were used to train the predictive models. For example, temperature readings obtained at 24 hours after stroke/sepsis could be combined with sickness scores obtained at the same time point, but not sickness scores obtained at other time points. Second, an expanded parameter search with combinations of physiological parameters obtained at different time points was conducted. When training support vector machines, input features were scaled to a zero mean and unit variance.

2.2.8 Data availability

Two datasets including (1) core body temperature, body weight, and modified DeSimoni neuroscore of animals of the stroke model[3] and (2) surface body temperature, body weight and sickness severity score of animals of the sepsis model[4] are available as open data on Figshare Repository in raw data format.

3 Results

3.1 Systematic review

1,578 search results were retrieved (Medline: 668; Embase: 910) and 1,238 were included in title and abstract screening after duplicates were removed. Overall, 110 full text articles were screened and a total of 34 studies were included for subsequent data extraction (Fig. 1; Tab. 2). Included studies represented a wide range of acute and chronic mouse models including infection/inflammation (n = 14; Nemzek et al., 2004; Huet et al., 2013; Bast et al., 2004; Adamson et al., 2013; Kort et al., 1998; Hankenson et al., 2013; Warn et al., 2003; Arranz-Solis et al., 2015; Dellavalle et al., 2014; Molins et al., 2012; Wright and Phillpotts, 1998; Sand et al., 2015; Miller et al., 2013; Trammell and Toth, 2011), toxin/poisoning (n = 3; Vlach et al., 2000; Beyer et al., 2009; Cates et al., 2014), cancer/tumor (n = 5; Husmann et al., 2015; Aldred et al., 2002; Miller et al., 2016; Paster et al., 2009; Hunter et al., 2014), and others (n = 12; Solomon et al., 2011; Stoica et al., 2016; Leon et al., 2005; Takayama-Ito et al., 2017; Passman et al., 2015; Chappell et al., 2011, Faller et al., 2015; Weismann et al., 2015; Koch et al., 2016; Nunamaker et al., 2013a,b; Ray et al., 2010).

[3] doi:10.6084/m9.figshare.7479965
[4] doi:10.6084/m9.figshare.7480016

Tab. 2: List of studies included in the review (n = 34) summarized by type of experiment, sample size, time course of the experiment, type of humane endpoints, frequency of inspection/measurement, and cut-off threshold used/proposed for euthanasia

N/A, not found/not available; sur, survived

Experiment	Sample size	Time course	Type of humane endpoint	Frequency of measurement	Cut-off threshold	Reference
Intranasal invasive pulmonary aspergillosis	n = 122; n(sur) = 45	< 8 days	weight, surface temperature	once daily (weight); ≤ 3 times/ day (surface temperature)	> 20% weight loss; surface temperature < 28.8°C	Adamson et al., 2013
Leukemia	n = 20	≤ 14 days	score, clinical signs	every 12 h (first 2 days); every 6 h (day 3 and thereafter)	score ≤ 3; clinical signs on two consecutive examinations	Aldred et al., 2002
Neospora caninum infection	n = 118; n(sur) = 93	≤ 30 days	score	twice daily	score ≥ 3	Arranz-Solis et al., 2015
Pneumonia	n = 31; n(sur) = 10	≤ 96 hours	surface temperature	twice daily	surface temperature ≤ 30°C	Bast et al., 2004
Ricin poisoning	n = 66	≤ 100 hours	core temperature, clinical signs	every 30 min	two consecutive temperature measurements < 32°C; clinical signs	Beyer et al., 2009
Rattlesnake venom	n = 30; n(sur) = 19	≤ 8 hours	core temperature	every 10-30 min (first 2 h post-injection); every 1-2 h (thereafter)	core temperature < 33.2°C	Cates et al., 2014
Postsurgical recovery	n = 45	≤ 14 days	score	daily	score ≥ 4	Chappell et al., 2011
Plasmodium infection	n = 40; n(sur) = 27	≤ 15 days	surface temperature	once daily (until symptoms were present); 3 times/day (thereafter)	surface temperature < 30°C	Dellavalle et al., 2014
Myocardial infarction	n = 60	≤ 8 weeks	weight, clinical signs	at 24 h and 30 min after application of analgesia	weight loss (unspecified); clinical signs	Faller et al., 2015
Ocular herpes simplex virus infection	n = 120; n(sur) = 38	≤ 60 days	core temperature, weight, score	once daily (until day 4; day 15-30); twice daily (day 5 -day 15)	core temperature < 34.5°C; > 0.05g/ day weight loss, combination of temperature and weight loss; score = 3 for 24 h	Hankenson et al., 2013
Pneumonia (septic shock)	n = 118; n(sur) = 104	≤ 5 days	score	twice daily (score 1); 3 times/day (score 2); 4-6 times/day (score 3); hourly (score 4)	score = 4	Huet et al., 2013
Lymphoma	n = 36	≤ 5 weeks	weight, clinical signs	5-7 times/week	> 20% weight loss or > 15% weight loss for 72 h; clinical signs	Hunter et al., 2014
Bone cancer	n = 30	≤ 26 or 34 days	weight, clinical signs	once a week; twice daily after application of analgesia	> 15% weight loss; clinical signs	Husmann et al., 2015
Total-body irradiation	n = 132; n(sur) = 77	≤ 30 days	score	twice daily (noncritical period); ≤ 4 times/day (critical period)	score = 12	Koch et al., 2016

Experiment	Sample size	Time course	Type of humane endpoint	Frequency of measurement	Cut-off threshold	Reference
Pneumonia	n = 10	≤ 24 hours	core temperature	twice daily	core temperature < 36°C	Kort et al., 1998
Heat stress	n = 78	< 44 hours	core temperature	continuous (every 60 sec)	no recovery from hypothermia by 765 min	Leon et al., 2005
Influenza A infection	n = 16	≤ 7 days	weight, score	daily	> 25% weight loss; score ≥ 4	Miller et al., 2013
Bladder cancer	n = 80	≤ 50 days	size of tumor, weight, clinical signs	daily	tumor > 10 mm (12mm), > 15% weight loss, or if either coincided with clinical signs	Miller et al., 2016
Francisella tularensis infection	n = 56	< 264 hours	core temperature	every 1 to 2 hours	N/A	Molins et al., 2012
Septic shock	n = 36; n(sur) = 10	≤ 14 days	weight, surface temperature	once daily	surface temperature ≤ 30°C; initial weight gain	Nemzek et al., 2004
Total-body irradiation	n = 240; n(sur) = 57	≤ 30 days	score	once daily (days 1-6 and 23-30); twice daily (days 7-22)	score ≥ 7	Nunamaker et al., 2013a
Total-body irradiation	n = 175; n(sur) = 66	≤ 30 days	score	once daily (days 1-6; 19-30; twice daily (days 7-18)	score > 6	Nunamaker et al., 2013b
Choline-deficient, ethionine-supplemented diet	n = 34; n(sur) = 23	< 3 weeks	weight, score	twice daily until partial recovery; daily thereafter	≥ 20% weight loss; score = 3	Passman et al., 2015
Abdominal tumor	n = 40	≤ 46 days	score, clinical signs	daily	score = 1 with clinical signs; score = 3	Paster et al., 2009
Longevity and aging	n = 110	≤ 40 months	core temperature, weight, temperature x weight	at least once every 4 weeks	≥ 15% weight loss; core temperature < 25°C;	Ray et al., 2010
Septic shock	n = 15	≤ 21 days	score	once after 24 h; irregular monitoring (in between)	score = 5	Sand et al., 2015
Amyotrophic lateral sclerosis	n = 162	≤ 150 days of age	score	N/A	score = 4	Solomon et al., 2011
Amyotrophic lateral sclerosis	n = 42	≤ 260 days of age	weight, clinical signs	once every week	≥ 15% weight loss; clinical signs	Stoica et al., 2016
Rabies virus infection	n = 359	≤ 11 days	score, weight	daily	score = 2 combined with a weight loss of ≥ 15%	Takayama-Ito et al., 2017
Influenza virus infection	n = 118	≤ 5-21 days after injection, depending on the type of infection	core temperature, weight, core temperature x weight (T x BW)	daily (temperature); weight (3 times/ week)	temperature < 35°C or T x BW < 60% of baseline values on day 7 after infection; T x BW < 90% of baseline value on day 2 or day 5 after infection; T x BW < 85% of baseline value on day 1 after infection	Trammell and Toth, 2011

Experiment	Sample size	Time course	Type of humane endpoint	Frequency of measurement	Cut-off threshold	Reference
Septic shock	n = 48; n(sur) = 22	≤ 25 days	core temperature	every 15 minutes	core temperature < 23.4°C	Vlach et al., 2000
Fungal infection	n = 160; n(sur) = 100	≤ 11 days	core temperature	≤ 4 times daily, maximum of 10 h between observations	core temperature < 33.3°C	Warn et al., 2003
GM1 gangliosidosis	n = 122	≤ 576 days	weight, clinical signs	19 times at irregular intervals	≥ 15% weight loss from maximum weight; clinical signs	Weismann et al., 2015
Venezuelan encephalomyelitis virus infection	n = 20	≤ 14 days	score	at least twice daily	score = 2	Wright and Phillpotts, 1998

3.1.1 Time course of the study and frequency of monitoring

Time courses of experiments ranged from 8 hours to 40 months. Among the 34 studies, duration of experiments was shorter than or equal to 24 hours in 2 studies (Kort et al., 1998; Cates et al., 2014), between a day and a week in 5 studies (Leon et al., 2005; Beyer et al., 2009; Miller et al., 2013; Bast et al., 2004; Huet et al., 2013), between a week and one month in 17 studies (Molins et al., 2012; Takayama-Ito et al., 2017; Passman et al., 2015; Wright and Phillpotts, 1998; Sand et al., 2015; Chappell et al., 2011; Adamson et al., 2013; Koch et al., 2016; Trammell and Toth, 2011; Nunamaker et al., 2013a,b; Nemzek et al., 2004; Dellavalle et al., 2014; Aldred et al., 2002; Warn et al., 2003; Vlach et al., 2000; Arranz-Solis et al., 2015), between one month and 3 months in 6 studies (Miller et al., 2016; Faller et al., 2015; Hankenson et al., 2013; Paster et al., 2009; Husmann et al., 2015; Hunter et al., 2014), and longer than 3 months in 4 studies (Weismann et al., 2015; Solomon et al., 2011; Stoica et al., 2016; Ray et al., 2010).

A great variance was observed in the frequency of evaluation intervals, with the most frequent data collection occurring once per minute using an automated system (Leon et al., 2005), while the longest interval between inspections was once or at least once every 4 weeks (Ray et al., 2010; Weismann et al., 2015). Some authors used an inspection frequency of once per day (Miller, D. S. et al., 2013; Miller, A. et al., 2016; Chappell et al., 2011; Paster et al., 2009; Nemzek et al., 2004), while others used varying interval frequencies such as once per 15 minutes (Vlach et al., 2000), once per 30 minutes (Beyer et al., 2009), twice per day (Cates et al., 2014; Kort et al., 1998; Arranz-Solis et al., 2015), at least twice per day (Wright and Phillpotts, 1998), at least 4 times per day (Warn et al., 2003), once per week (Stoica et al., 2016), 5-7 times per week (Hunter et al., 2014). As expected, in studies with faster disease progression, authors adjusted the evaluation schedule accordingly by increasing the frequency of monitoring for animals in severe distress or animals requiring additional care (Molins et al., 2012; Passman et al., 2015; Hankenson et al., 2013; Huet et al., 2013; Koch et al., 2016; Trammell and Toth, 2011; Cates et al., 2014; Nunamaker et al., 2013a,b; Dellavalle et al., 2014; Aldred et al., 2002; Husmann et al., 2015). In two studies (Adamson et al., 2013; Trammell and Toth, 2011), individual physiological parameters were assessed at different time points. In three studies, animals were inspected only once after treatment (Takayama-Ito et al., 2017; Sand et al., 2015; Faller et al., 2015).

3.1.2 Body temperature

Among the 34 studies, 14 demonstrated that both core body temperature (n = 10; Molins et al., 2012; Leon et al., 2005; Beyer et al., 2009; Cates et al., 2014; Hankenson et al., 2013; Trammell and Toth, 2011; Warn et al., 2003; Kort et al., 1998; Vlach et al., 2000; Ray et al., 2010) and surface body temperature (n = 4; Adamson et al., 2013; Bast et al., 2004; Nemzek et al., 2004; Dellavalle et al., 2014) could be used to refine the humane endpoint. In 6 of the 14 studies, other physiological parameters were used in combination or independently as humane endpoint criteria, including clinical signs (Beyer et al., 2009), weight (Hankenson et al., 2013; Adamson et al., 2013; Nemzek et al., 2004), and the product of body temperature and weight (Trammell and Toth, 2011; Ray et al., 2010). Cut-off values for euthanasia ranged from 23.4 to 36°C (31.55 (4.7) °C) for endpoints determined from core temperature and from 28.8 to 30°C (29.7 (0.6) °C) for endpoints determined from surface temperature. In addition, recovery from hypothermia (Leon et al., 2005) or a temperature drop below the baseline mean temperature (Molins et al., 2012) were used as humane endpoints. While in most studies, animals were humanely killed upon reaching the cut-off criterion at one single time point, Beyer et al. (2009) euthanized animals when the body temperature was lower than 32°C in two consecutive inspections.

3.1.3 Body weight

In 14 out of the 34 studies, body weight was used to determine the humane endpoint (Takayama-Ito et al., 2017; Passman et al., 2015; Miller, D. S. et al., 2013; Miller, A. et al., 2016; Faller et al., 2015; Weismann et al., 2015; Adamson et al., 2013; Hankenson et al., 2013; Trammell and Toth, 2011; Nemzek et al., 2004; Stoica et al., 2016; Husmann et al., 2015; Ray et al., 2010; Hunter et al., 2014). All of these 14 studies included additional hu-

mane endpoints such as clinical signs of distress and disease progression (Miller et al., 2016; Faller et al., 2015; Weismann et al., 2015; Stoica et al., 2016; Husmann et al., 2015; Hunter et al., 2014), sickness severity scores (Passman et al., 2015; Miller et al., 2013; Takayama-Ito et al., 2017), body temperature (Hankenson et al., 2013; Adamson et al., 2013; Nemzek et al., 2004), and the product of body temperature and weight (Trammell and Toth, 2011; Ray et al., 2010). Although a weight loss of more than 20% compared to baseline is widely regarded as a common humane endpoint, it was only reported in 3 studies (Passman et al., 2015; Adamson et al., 2013; Ray et al., 2010). Other authors used a weight loss of more than 15% (Takayama-Ito et al., 2017; Miller et al., 2016; Weismann et al., 2015; Stoica et al., 2016; Husmann et al., 2015) or 25% (Miller et al., 2013). One study used an absolute weight loss of greater than 0.05 g per day as an indicator of a higher risk of death (Hankenson et al., 2013). In a mouse model of cecal ligation and puncture (CLP), initial weight gain was observed in 100% animals that died within the next 3 days and was therefore considered as an indicator of higher risk of death (Nemzek et al., 2004). One study did not define a cut-off threshold for a weight-based humane endpoint (Faller et al., 2015). Another used the product of body temperature and weight for humane endpoint definition (Trammell and Toth, 2011).

3.1.4 Sickness severity score

Among 15 studies that used sickness severity scores to determine the humane endpoint (Passman et al., 2015; Wright and Phillpotts, 1998; Sand et al., 2015; Miller et al., 2013; Chappell et al., 2011; Huet et al., 2013; Koch et al., 2016; Nunamaker et al., 2013a,b; Paster et al., 2009; Solomon et al., 2011; Arranz-Solis et al., 2015; Aldred et al., 2002; Hankenson et al., 2013; Takayama-Ito et al., 2017), 3 applied the score-based threshold with other criteria such as weight (Passman et al., 2015; Miller et al., 2013; Takayama-Ito et al., 2017) and clinical signs (Paster et al., 2009). There was great heterogeneity in score-based thresholds, reflecting the common use of model-specific scores. In 12 studies higher scores indicated more severe symptoms. In one study, a score of 0-1 was assigned to animals showing abnormal behavior and appearance, using a total score of 1 as the humane endpoint (Paster et al., 2009). In one study, a score sheet indicating clinical symptoms was used to determine sickness severity, however, the cut-off value for early euthanasia was not clearly described (Aldred et al., 2002).

3.1.5 Combining body weight, body temperature, and sickness severity scores in humane endpoint determination

In 16 studies, more than one physiological or behavioral parameter was used in determining the humane endpoint. Thus, the cut-off criterion was defined by fulfilling one or more physiological or behavioral criteria. Among the 15 studies, 3 studies involved a direct combination (e.g., the product of two parameters) of more than one physiological parameter to derive a surrogate indicator for a higher risk of death (Hankenson et al., 2013; Trammell and Toth, 2011; Ray et al., 2010). In studies using a product of more than one parameter, death could be predicted with higher accuracy. For example, the composite obtained by multiplying weight and body temperature yielded higher prediction accuracy than applying weight or body temperature cut-off criteria individually.

3.1.6 Evaluation of the humane endpoints

Twenty studies assessed the performance of humane endpoints. Predictability of death as an outcome event was evaluated by means of sensitivity (n = 6, min = 68%, max = 100%, mean (SD) = 89.7 (13.1)%; Adamson et al., 2013; Hankenson et al., 2013; Trammell and Toth, 2011; Dellavalle et al., 2014; Kort et al., 1998; Warn et al., 2003), specificity (n = 3, min = 90.9%, max = 100%, mean (SD) = 96.0 (4.6)%; Adamson et al., 2013; Hankenson et al., 2013; Warn et al., 2003), logistic regression (n = 2, $p < 0.0001$ and $p = 0.0077$; Cates et al., 2014; Vlach et al., 2000), prediction accuracy (n = 2, 92.7% and 2% underestimation; Koch et al., 2016; Ray et al., 2010), percentage/number of mice present with a particular criterion/sign (n = 5, min = 86%, max = 100%, mean (SD) = 95.3% (5.8); Molins et al., 2012; Takayama-Ito et al., 2017; Bast et al., 2004; Solomon et al., 2011; Aldred et al., 2002), relative number of predicted dead animals (n = 1, 96%; Vlach et al., 2000), physiological changes observed in different treatment groups (n = 2, significant difference observed; Paster et al., 2009; Leon et al., 2005), positive predictive value (n = 1, 55.5%; Nemzek et al., 2004), false positive rate (n = 1, 4-33%; Trammell and Toth, 2011), and corresponding mortality rate (n = 2, 86.2-100% and 78.6-100%; Nunamaker et al., 2013a,b) with some studies using multiple evaluation metrics. In one study, specificity was used to assess humane endpoint performance. However, it could not be appropriately assessed as none of the animals reached the pre-defined cut-off criterion (Dellavalle et al., 2014).

3.2 Death prediction in animal models of stroke and sepsis

To facilitate direct comparison, animals in both stroke and sepsis models were divided into three groups based on treatment and survival. Group 1 (control, n(stroke) = 66, n(sepsis) = 151) consisted of sham animals or animals treated with saline that reached the planned experimental endpoint, group 2 (survivor group, n(stroke) = 322, n(sepsis) = 254) consisted of animals treated with MCAo or LPS that reached the planned experimental endpoint and group 3 (non-survivor group, n(stroke) = 58, n(sepsis) = 30) consisted of animals that spontaneously died or were euthanized upon reaching the humane endpoint criteria.

3.2.1 Body temperature in survivor and non-survivor animals

In the stroke model, the temperature of the survivor and non-survivor groups decreased by an average of 1.1°C and 4.6°C from baseline (35.3 (2.1) °C and 31.6 (6.6) °C, respectively) during the first 5 days following MCAo (Tab. 3). The core body temperature of the control group remained unchanged during the experiment.

In the sepsis model, LPS-treated animals showed a pronounced decrease in surface body temperature during the two consecutive injection days, regardless of survival status. Lowest surface temperature of survivor animals was observed 10.5 hours following

Tab. 3: Comparison of physiological measures among control, survivor and non-survivor groups
(A) Middle cerebral artery occlusion (MCAo) stroke model, from the day animals underwent the MCAo procedure up to the 5th day post stroke; (B) lipopolysaccharide (LPS)-induced sepsis model, from the first injection up to 192 h after the first injection. Baseline measurements were conducted before the MCAo/sham treatment or the first LPS/saline injection. Baseline values were measured on the day of treatment. Monitoring period was defined as the 1st to 5th day post-stroke and the 1st to 8th day post-sepsis.

A

	Control (n = 66)	Survivor (n = 322)	Non-survivor (n = 58)
Baseline core temperature (°C) min, max, mean (SD)	35.7, 38.9 37.0 (0.8)	34.1, 38.9 36.4 (1.0)	28.0, 38.3 36.2 (1.9)
Core temperature during monitoring (°C) min, max, mean (SD)	33.7, 38.4 36.6 (0.9)	20.8, 38.4 35.7 (1.6)	17.8, 37.8 33.5 (3.7)
Baseline body weight (g) min, max, mean (SD)	16.0, 32.6 24.8 (3.2)	16.7, 34.9 25.4 (3.3)	14.5, 33.9 26.9 (3.7)
Body weight during monitoring (g) min, max, mean (SD)	16.1, 30.1 22.4 (2.4)	13.9, 31.0 21.4 (3.0)	14.3, 29.6 21.0 (3.1)
Baseline Neuroscore min, max, mean (SD)	0, 3 0.9 (1.0)	0, 4 0.33 (0.8)	0, 2 0.4 (0.9)
Neuroscore during monitoring min, max, mean (SD)	0, 17.0 4.9 (4.9)	0, 35 9.1 (5.5)	0, 41 15.4 (9.5)

B

	Control (n = 151)	Survivor (n = 254)	Non-survivor (n = 30)
Baseline surface temperature (°C) min, max, mean (SD)	27.0, 33.7 30.8 (1.1)	26.3, 33.8 30.5 (1.6)	27.5, 33.3 30.6 (1.4)
Surface temperature during monitoring (°C) min, max, mean (SD)	23.9, 36.5 30.6 (1.4)	20.3, 34.6 29.1 (2.0)	19.0, 31.7 25.7 (2.7)
Baseline body weight (g) min, max, mean (SD)	17.5, 26.9 21.5 (1.7)	14.9, 28.7 21.5 (1.8)	17.6, 24.3 21.4 (2.0)
Body weight during monitoring (g) min, max, mean (SD)	16.4, 27.6 21.9 (1.5)	13.2, 27.7 19.7 (2.1)	12.5, 23.3 18.8 (2.6)
Sickness score during monitoring min, max, mean (SD)	0, 2 0 (0.1)	0, 4 0.7 (0.8)	0, 4.5 2.1 (1.1)

both the first and second injections (27.4 (1.7) °C and 28.1 (1.6) °C, respectively). The surface body temperature of the survivor group returned to baseline within 96 hours following the second LPS injection. Surface temperature of non-survivor animals was the lowest 10.5 hours following the first injection (25.4 (1.8) °C) and 9 hours following the second injection (23.4 (1.2) °C), respectively. No significant decrease in core and surface temperatures from baseline was observed in control animals.

3.2.2 Body weight in survivor and non-survivor animals

In the stroke model, a decrease in body weight was observed in control animals, survivors and non-survivors (Tab. 3). In the control group, body weight was 24.8 (3.2) g at baseline decreasing to a minimum of 22.3 (2.5) g on the 2nd day post-treatment.

The lowest weight of survivor animals 21.0 (2.8) g was measured on the 2nd day following MCAo. The non-survivor group had the most profound decrease of 8.0 g from baseline (26.9 (3.7) g). The lowest mean body weight was 18.9 (2.6) g on the 4th day following MCAo. Once the minimum was reached, all groups subsequently recovered body weight until the end of the observation period.

In the sepsis model, no weight changes other than random fluctuations were observed in control animals. Body weight of the survivor group reached its minimum 54 hours following the first LPS injection (17.7 (1.5) g) and returned to baseline at 192 hours (21.7 (1.6) g, as compared to baseline weight = 21.5 (1.8) g). The lowest weight of non-survivor animals (baseline weight: 21.4 (2.0) g) was measured 96 hours after the first injection (14.4 (2.4) g).

3.2.3 Sickness severity score in survivor and non-survivor animals

In the stroke model, modified DeSimoni neuroscore of control animals was 0.9 (1.0) at baseline, peaked at 5.7 (4.3) on the 1st day after MCAo and subsequently decreased on the 2nd day after MCAo (Tab. 3). Non-survivors had a higher score on the 1st and 2nd day following MCAo than survivors (16.0 (9.6) and 14.8 (9.4) vs. 9.2 (5.2) and 9.1 (5.7), respectively).

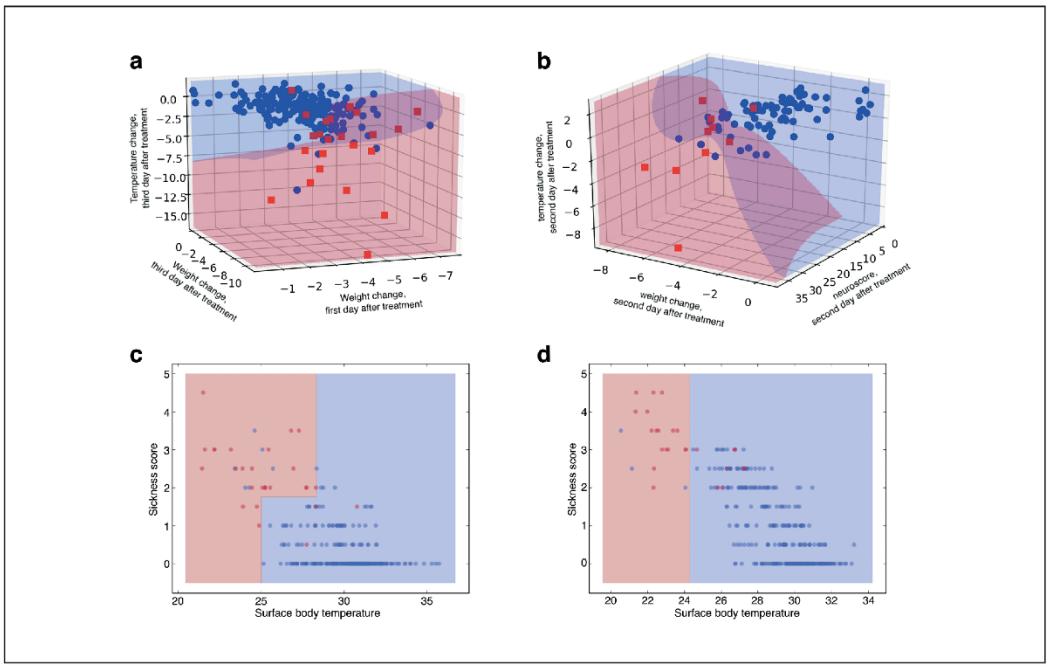

Fig. 2: Decision boundaries determined by the machine learning model
The earliest time points (2 and 3 days or 24 h post-treatment in the stroke or sepsis model, respectively) at which impending death could be predicted with acceptable accuracy were included. Data from 36 h post-injection in the sepsis model was plotted for comparison purposes. Parameter-model combinations leading to highest prediction accuracy were plotted. (a) Decision boundary obtained with body weight change on the 1st and 3rd day after treatment and core body temperature change on the 3rd day after treatment. (b) Decision boundary obtained with the modified DeSimoni neuroscore, body weight change and core body temperature change on the 2nd day after treatment. (c) Decision boundary obtained with surface temperature and sickness score 24 h after the first injection of LPS/saline. (d) Decision boundary obtained with surface temperature and sickness score 36 h after the first injection. Blue dot, survivor animal (control + survivor); red dot, animal euthanized upon reaching the pre-defined sickness score-based humane endpoint or died spontaneously (non-survivor); blue area, predicted survival; red area, predicted death. Gaussian Naïve Bayes (as in a and b), decision trees of depth 2 (as in c) and 1 (as in d) were used to determine the decision boundaries.

In the sepsis model, sickness scores of the survivor group peaked at 10.5 hours (1.2 (0.8)) and 12 hours (1.4 (0.9)) after the injection on day 1 and 2, respectively, then returned to baseline level within 96 hours following the first LPS injection. Sickness scores of non-survivors increased after injection day 1 and peaked at 10.5 hours after the second injection (3.3 (0.6)). The sickness scores among control animals remained unchanged (Tab. 3).

3.2.4 Prediction of death from physiological measures

To assess the performance of physiological and behavioral parameters such as body weight, temperature, and sickness severity score/modified DeSimoni neuroscore in death prediction, we developed an automated parameter search method to test the performance of machine learning models trained with different combinations of parameters. Apart from body weight, temperature, and sickness score/neuroscore, the absolute change per timepoint for these parameters was calculated by subtracting the baseline value from measured values at each timepoint, resulting in an additional parameter set. The two sets of parameters were used in model training.

Machine learning models were trained with individual parameters or combinations of physiological and behavioral parameters. Model performance was analyzed for time points prior to the average time of death (i.e., 3.9 (2.4) days in the stroke model and 60.5 (35.1) hours in the sepsis model, respectively). Animals in the stroke model displayed a significant gender-dependent difference in baseline body weight (male: 26.8 (2.8) g; female: 23.1 (2.9) g; $p < 0.001$, Mann-Whitney U test), thus death prediction was conducted separately for each gender.

Death as an outcome event could be predicted with considerable accuracy of 93.2% (male) or 93.0% (female) in the model of stroke and 96.2% in the model of sepsis (Tab. 4a,b), with weight change on the 1st and 3rd day after treatment, core temperature change on the 3rd day after treatment (male, stroke model), or with neuroscore, weight change, and core temperature change on the 2nd day after treatment (female, stroke model), and with surface temperature and sickness score at 24 hours after the first injection (sepsis model). Gaussian Naïve Bayes (male and female, stroke model), decision tree of a depth of 2 (with data from 24 hours after the first injection, sepsis model) and 1 (with data from 36 hours after the first injection, sepsis model) were used to identify decision boundaries shown in Figure 2.

In male mice of the stroke model, 13 out of 23 animals that died or reached predefined humane endpoint criteria at a later time point could have been euthanized earlier (t = 3 days after MCAo for euthanasia; average time of death of the 13 animals = 4.08 (1.07) days post-MCAo) while 3.3% (6 out of 181) survivors were falsely predicted to die. In female mice of the stroke model, 4 out of 10 animals that died or reached the predefined humane endpoint during the experiment could have been euthanized earlier (t = 2 days after MCAo for euthanasia; average time of death of the 4 animals = 4.25 (2.28) days post-MCAo). 3.9% (3 out of 77) animals that survived until the end of the experiment were falsely predicted to die (Fig. 2a,b).

In the sepsis model, 25 out of 28 animals could have been euthanized at an earlier time point (t = 24 hours post treatment for earlier euthanasia; average time of death of the 25 animals = 58.7 (35.0) hours post treatment) while 2.3% (6 out of 254) of LPS-treated animals that survived until the end of the experiment were falsely predicted to die (Fig. 2c,d).

Prediction of death as an outcome event at different post-treatment time points

By applying machine learning models trained with physiological parameters, death could be predicted within 2 or 3 days (stroke model) or 24 hours (sepsis model) after MCAo or LPS injection. In the stroke model, death could not be predicted at an acceptable level of accuracy until the 2nd (female mice) or 3rd (male mice) day post-MCAo (Tab. 4a). In the sepsis model, physiological measures obtained 12 hours after the first injection could not predict death as an outcome event due to the low general performance of the model at this time point (for details see Tab. 4b).

Prediction of death by using single or multiple physiological measurements

In the stroke model, adding additional physiological parameters in model training increased death prediction performance (Tab. 4a). In male mice, adding weight change on the 1st day after treatment and core temperature change on the 3rd day after treatment increased sensitivity from 0.34 (0.15) to 0.61 (0.088), precision from 0.64 (0.27) to 0.74 (0.070), and accuracy from 0.91 (0.03) to 0.93 (0.02). In female mice, using neuroscore and core temperature change on the 2nd day after treatment in addition to weight change improved sensitivity from 0.19 (0.14) to 0.69 (0.28), precision from 0.25 (0.20) to 0.83 (0.24) and accuracy from 0.86 (0.045) to 0.93 (0.030) of the trained model.

In the sepsis model, using both sickness score and surface temperature in model training improved accuracy and general performance of the prediction model (Tab. 4b). At 24 hours after treatment, using sickness score in addition to surface temperature in model training led to an increase in sensitivity from 0.65 (0.11) to 0.86 (0.12) and accuracy from 0.95 (0.01) to 0.96 (0.01), while model precision decreased slightly from 0.77 (0.17) to 0.75 (0.11).

Interaction between the use of multiple physiological measurements and time points

In the stroke model, due to the low performance of models trained with combinations of physiological parameters obtained on the same day, data from different post-treatment days were used in combination in model training. This approach precluded the assessment of an interaction between multiple parameters and individual time points.

In the sepsis model, using multiple physiological parameters to train the predictive model enhanced the accuracy of death prediction at individual time points. When the model was trained with data from 24 hours after the first LPS injection, using sickness score as an additional measure increased sensitivity and accuracy by 21.5% and 1.1%, respectively (Tab. 4b). No improvement in model performance was observed using data from 36 hours after the first LPS injection when sickness scores were included in model training (Tab. 4b).

4 Discussion

Our study revealed three main findings: Firstly, the systematic review demonstrated remarkable heterogeneity of humane endpoints even within the same animal model due to lack of systematic assessment, protocol standardization, and/or ambiguous or incomplete description of results. This illustrates a distinct challenge in adopting humane endpoints from the literature and highlights the need for researchers to tailor humane endpoints based on the currently available evidence. Secondly, using data from mouse models of stroke and sepsis, we found that machine learning by means of an automated search for predictive parameters, parameter combinations, and models and hyperparameters, can be used to accurately determine endpoint criteria and cut-off threshold values across models. Thirdly, when we applied these criteria retrospectively to the available derivation cohort datasets, we found that a large number of animals could have been euthanized at earlier time points in both stroke and sepsis models, thus potentially reducing otherwise unnecessary suffering.

4.1 Systematic review

In this study, we reviewed 34 mouse studies using humane endpoints based on body temperature, body weight and/or sickness severity score (Tab. 5). We found that temperature-based endpoints are commonly applied both in acute and chronic disease

Tab. 4: Death prediction with single or multiple parameters at different time points
(A) Middle cerebral artery occlusion (MCAo) stroke model. Prediction model, Gaussian Naïve Bayes. (B) Lipopolysaccharide (LPS)-induced sepsis model. Prediction model, decision tree with a depth = 2 (24 h) and a depth = 1 (36 h). Decision tree of depth 2 was not used for 36 h after the first injection due to overfitting. 3-fold stratified cross-validation was used to evaluate the performance of the trained model. Only performance of the most predictive parameters and model combinations is shown. Data shown are means (SD) of scores obtained from the 2- (stroke model) or 3- (sepsis model) fold cross-validation.

A

Gender	male (n = 204, n(dead) = 23)			female (n = 87, n(dead) = 10)		
Parameters	weight change on the 3rd day after treatment	weight change on the 1st day after treatment; weight change on the 2nd day after treatment; core temperature change on the 2nd day after treatment	weight change on the 1st day after treatment; weight change on the 3rd day after treatment; core temperature change on the 3rd day after treatment	weight change on the 2nd day after treatment	neuroscore on the 1st day after treatment; weight change on the 1st day after treatment; core temperature change on the 1st day after treatment	neuroscore on the 2nd day after treatment; weight change on the 2nd day after treatment; core temperature change on the 2nd day after treatment
Sensitivity (recall)	0.339 (0.148)	0.482 (0.081)	0.613 (0.088)	0.194 (0.142)	0.361 (0.307)	0.694 (0.275)
Precision	0.644 (0.274)	0.667 (0.272)	0.738 (0.070)	0.25 (0.204)	0.417 (0.312)	0.833 (0.236)
Accuracy	0.907 (0.026)	0.902 (0.046)	0.932 (0.018)	0.863 (0.045)	0.896 (0.029)	0.930 (0.030)
Averaged score	0.630	0.684	0.761	0.436	0.558	0.819

B

Time	t = 12 h post-treatment (n = 152, n(dead) = 14)		t = 24 h post-treatment (n = 345, n(dead) = 28)		t = 36 h post-treatment (n = 342, n(dead) = 25)	
Parameters	surface temperature	surface temperature, sickness score	surface temperature	surface temperature, sickness score	surface temperature	surface temperature, sickness score
Sensitivity (recall)	0	0	0.648 (0.114)	0.863 (0.124)	0.685 (0.092)	0.685 (0.092)
Precision	0	0	0.768 (0.165)	0.747 (0.106)	0.806 (0.142)	0.806 (0.142)
Accuracy	0.908 (0.009)	0.908 (0.009)	0.951 (0.004)	0.962 (0.011)	0.962 (0.004)	0.962 (0.004)
Averaged score	0.303	0.303	0.789	0.857	0.818	0.818

models due to their objectivity and ease of measurement. However, we found considerable variations in temperature cut-off values between studies even within the same animal model (Molins et al., 2012; Beyer et al., 2009; Adamson et al., 2013; Bast et al., 2004; Cates et al., 2014; Hankenson et al., 2013; Trammell and Toth, 2011; Nemzek et al., 2004; Dellavalle et al., 2014; Hunter et al., 2014; Warn et al., 2003; Kort et al., 1998; Vlach et al., 2000; Ray et al., 2010), which can at least partly be explained by variations in ambient temperature.

Ambient temperature is an important factor contributing to differences between an animal's core and surface temperature. The lower the ambient temperature, the lower an animal's surface temperature, while the animal's core temperature stays constant as long as thermoregulatory responses are intact (Kurz, 2008). In addition, measurement location and handling stress may contribute to differences in cut-off values between studies. Some authors used restraining devices for probe-based surface temperature acquisition. However, stress results in activation of the sympathetic nervous system, which in turn leads to increased thermogenesis and vasoconstriction of skin vessels, resulting in an increase in body temperature within seconds of being restrained (Vianna and Carrive, 2005). Therefore, body temperature measurements could be confounded by repeated handling (Cabanac and Briese, 1992).

Tab. 5: Summary of endpoint criteria, advantages and disadvantages of weight-, body temperature-, and severity score-based humane endpoints

Humane endpoint	Studies included	Endpoint	Advantages	Disadvantages
Weight-based	13	15-25% of baseline body weight	– easy administration – high objectivity	– poor performance in acute disease models – high handling stress
Core temperature-based	11	23.4-36°C, 31.55 (4.7) °C	– high objectivity – high accuracy – continuous monitoring – low handling stress	– high variance due to an animal's thermo-regulatory responses and handling stress
Surface temperature-based	4	28.8-30°C, 29.7 (0.6) °C	– high objectivity – high accuracy – low handling stress	– high variance due to an animal's thermo-regulatory responses and handling stress
Severity score-based	14	Multiple criteria	– easy administration – simplified classification of physiological states – systematic documentation	– requires familiarity – inter-observer variability – time-consuming – high handling stress

Humane endpoints based on rapid (over a few days) or gradual (over extended periods of time leading to emaciation) weight loss relative to baseline are easy to adopt and are widely applied. However, weight-based endpoints are suboptimal in highly acute models of disease (i.e., circulatory shock) due to an animal's rapid deterioration which may precede weight loss (Louie et al., 1997; Krarup et al., 1999; Nemzek et al., 2004). In addition, true weight loss may be masked by debilitating conditions such as ascites or tumor growth (Nemzek et al., 2004).

Sickness severity scores serve as a simplified classification of the physiological state of an animal, allowing systematic documentation of disease progression and humane endpoint evaluation. However, manual scoring suffers from subjectivity and is prone to high degrees of inter-observer bias (Morton, 2000).

Another factor contributing to high study heterogeneity is the lack of standardized schedules for animal inspection. Even for identical animal models, authors rarely used measurement schedules which were consistent with previously published data (Nunamaker et al., 2013a,b). Furthermore, only a minority of studies (9 out of 34) described the exact times relative to baseline and/or experimental intervention when temperature, body weight, and/or sickness score values were taken. Other variables potentially adding to study heterogeneity but only described by few studies include environmental factors such as the presence and type of bedding (described in 17 out of 34 studies) and number of cage mates (described in 22 out of 34 studies; Gordon, 2004; Gordon et al., 1998), as well as animal-specific factors such as strain, genotype, sex and developmental stage (described in all reviewed studies; Sanchez-Alavez et al., 2011; Trammell and Toth, 2011).

To counter the uncertainty in endpoint evaluation caused by variation of individual parameters, 15 of the reviewed studies used a combination of more than one humane endpoint criterion. Body weight was most commonly applied in combination with additional criteria (13 out of 13 studies used additional criteria) while sickness scores were mostly used independently (3 out of 13 studies used additional criteria). In 2 studies that evaluated the use of a composite score derived from other parameters (i.e., the product of weight x body temperature), a higher prediction accuracy was observed than when assessing parameters individually (Trammell and Toth, 2011; Ray et al., 2010). Authors used various metrics to assess the performance of humane endpoints, which often precludes direct between-study comparison. The three most common metrics were sensitivity (n = 7), specificity (n = 5), and percentage/number of mice exhibiting certain criteria/signs (n = 5). In 12 out of the 34 studies, humane endpoints were applied without being evaluated for reliability and/or performance or without endpoint evaluation being reported by the authors. Therefore, researchers may fail to appreciate the validity and/or reproducibility of humane endpoint criteria.

Taken together, traditional approaches in monitoring disease progression and predicting death suffer from high degrees of study heterogeneity, which confounds identification of cut-off values that can be applied to more than one study.

4.2 Machine learning-based death prediction

In an exploratory approach, we used machine learning as an alternative method for determining humane endpoints, which enabled us to identify case-specific cut-off values even across animal models without a fundamental change in methodology. Using body weight, sickness severity scores, and surface or core temperature data (for the sepsis or stroke model, respectively) from previously published studies and unpublished results, we trained a machine learning model for case-specific death prediction. First, we identified the parameter combinations that led to a high accuracy in detecting animals at higher risk of death. We then determined the cut-off values and assessed their performance using standardized metrics. We found that 17 out of 33 (stroke model) and 25 out of 28 (sepsis model) animals that were

euthanized or died at later timepoints during the experiments could have been euthanized 1.08 days (stroke model, male), 2.25 days (stroke model, female) or 1.45 days (sepsis model) earlier if endpoints determined by machine learning had been applied.

To our knowledge, this is the first study using a machine learning approach to systematically determine humane endpoints in mouse models of acute disease and there is no previous data to compare our results to.

Potential advantages of a machine learning-based approach for humane endpoint evaluation include improved standardization and comparability of results as identical metrics can be applied across studies. In addition, machine learning in this setting requires little expert knowledge and is relatively easy to apply. Once a model is trained with sufficient data, animal technicians and investigators can run the model with a simple command line tool to determine whether an animal has an increased risk of death, for example by visualizing decision boundaries (e.g., as shown in Fig. 2). Thus, machine learning may constitute a promising tool to improve the refinement of humane endpoints in animal studies of acute disease. However, the availability of data which can be used to train and/or validate machine learning models to evaluate and refine humane endpoints across disease models is limited as only very few authors choose to make their raw data available in open data repositories.

4.3 Limitations of the present study

In the systematic review, we excluded research articles in languages other than English and results published in the form of conference abstracts, posters and talks. This introduces a potential source of publication and result bias. A particular concern for the machine learning-based analysis was missing data and a small number of animals which reached a humane endpoint criterion. Nevertheless, for humane endpoint evaluation small datasets and missing data represent the real-world scenario. One solution is to increase the frequency of inspections during critical phases, not only to ensure that disease progression is properly monitored, but to obtain a larger dataset for training death prediction models. To this end, some authors suggest the use of biotelemetry systems with implanted transmitters, which allow continuous data acquisition (Leon et al., 2005). Lastly, we applied machine learning-derived endpoint criteria to the derivation cohort, which may introduce results bias. Although a stratified cross-validation was used to optimize generalizability, it would be beneficial for future studies to include an independent retrospective or prospective validation cohort to assess predictive model performance.

4.4 Conclusion

The degree of heterogeneity between studies using body temperature, weight and sickness scores to determine or evaluate humane endpoint criteria was high. This may preclude authors from adopting appropriate cut-off values from previously published studies and underscores the necessity for researchers to tailor the humane endpoints to the animal model and experimental design being used. In an approach aimed at enhancing the evaluation and application of humane endpoints using machine learning, we identified humane endpoints that would have allowed earlier euthanasia of animals, thus potentially reducing an animal's distress, suffering, and pain. Although the method still requires further validation, this exploratory study showed that machine learning-based humane endpoint criteria have the potential to be applied across various disease models. This may contribute to a more comprehensive approach in determining humane endpoints promoting the systematic application of 3R principles.

References

Adamson, T. W., Diaz-Arevalo, D., Gonzalez, T. M. et al. (2013). Hypothermic endpoint for an intranasal invasive pulmonary aspergillosis mouse model. *Comp Med 63*, 477-481.

Aldred, A. J., Cha, M. C. and Meckling-Gill, K. A. (2002). Determination of a humane endpoint in the L1210 model of murine leukemia. *Contemp Top Lab Anim Sci 41*, 24-27.

Arranz-Solis, D., Aguado-Martinez, A., Muller, J. et al. (2015). Dose-dependent effects of experimental infection with the virulent Neospora caninum Nc-Spain7 isolate in a pregnant mouse model. *Vet Parasitol 211*, 133-140. doi:10.1016/j.vetpar.2015.05.021

Bast, D. J., Yue, M., Chen, X. et al. (2004). Novel murine model of pneumococcal pneumonia: Use of temperature as a measure of disease severity to compare the efficacies of moxifloxacin and levofloxacin. *Antimicrob Agents Chemother 48*, 3343-3348. doi:10.1128/aac.48.9.3343-3348.2004

Benedito, R., Roca, C., Sörensen, I. et al. (2009). The notch ligands Dll4 and Jagged1 have opposing effects on angiogenesis. *Cell 137*, 1124-1135. doi:10.1016/j.cell.2009.03.025

Beyer, N. H., Kogutowska, E., Hansen, J. J. et al. (2009). A mouse model for ricin poisoning and for evaluating protective effects of antiricin antibodies. *Clin Toxicol (Phila) 47*, 219-225. doi:10.1080/15563650802716521

Cabanac, A. and Briese, E. (1992). Handling elevates the colonic temperature of mice. *Physiol Behav 51*, 95-98. doi:10.1016/0031-9384(92)90208-j

Cates, C. C., McCabe, J. G., Lawson, G. W. and Couto, M. A. (2014). Core body temperature as adjunct to endpoint determination in murine median lethal dose testing of rattlesnake venom. *Comp Med 64*, 440-447.

Chappell, M. G., Koeller, C. A. and Hall, S. I. (2011). Differences in postsurgical recovery of CF1 mice after intraperitoneal implantation of radiotelemetry devices through a midline or flank surgical approach. *J Am Assoc Lab Anim Sci 50*, 227-237.

Dellavalle, B., Kirchhoff, J., Maretty, L. et al. (2014). Implementation of minimally invasive and objective humane endpoints in the study of murine Plasmodium infections. *Parasitology 141*, 1621-1627. doi:10.1017/s0031182014000821

Dirnagl, U. and Members of the MCAO-SOP Group. (2012). Standard operating procedures (SOP) in experimental stroke research: SOP for middle cerebral artery occlusion in the mouse. *Nat Prec*. doi:10.1038/npre.2012.3492.3

Donath, S., An, J., Lee, S. L. L. et al. (2016). Interaction of ARC and Daxx: A novel endogenous target to preserve motor func-

tion and cell loss after focal brain ischemia in mice. *J Neurosci 36*, 8132-8148. doi:10.1523/jneurosci.4428-15.2016

Emmrich, J. V., Neher, J. J., Boehm-Sturm, P. et al. (2017). Stage 1 registered report: Effect of deficient phagocytosis on neuronal survival and neurological outcome after temporary middle cerebral artery occlusion (tMCAo). *F1000Res 6*, 1827. doi: 10.12688/f1000research.12537.1

Faller, K. M. E., McAndrew, D. J., Schneider, J. E. and Lygate, C. A. (2015). Refinement of analgesia following thoracotomy and experimental myocardial infarction using the mouse grimace scale. *Exp Physiol 100*, 164-172. doi:10.1113/expphysiol.2014.083139

Franco, N. H., Correia-Neves, M. and Olsson, I. A. S. (2012). How "humane" is your endpoint? – Refining the science-driven approach for termination of animal studies of chronic infection. *PLoS Pathog 8*, e1002399. doi:10.1371/journal.ppat.1002399

Glerup, S., Olsen, D., Vaegter, C. B. et al. (2014). SorCS2 regulates dopaminergic wiring and is processed into an apoptotic two-chain receptor in peripheral glia. *Neuron 82*, 1074-1087. doi:10.1016/j.neuron.2014.04.022

Gordon, C. J., Becker, P. and Ali, J. S. (1998). Behavioral thermoregulatory responses of single-and group-housed mice. *Physiol Behav 65*, 255-262. doi:10.1016/S0031-9384(98)00148-6

Gordon, C. J. (2004). Effect of cage bedding on temperature regulation and metabolism of group-housed female mice. *Comp Med 54*, 63-68.

Han, S., Taralova, E., Dupre, C. and Yuste, R. (2018). Comprehensive machine learning analysis of Hydra behavior reveals a stable basal behavioral repertoire. *eLIFE 7*, e32605. doi:10.7554/elife.32605

Hankenson, F. C., Ruskoski, N., Van Saun, M. et al. (2013). Weight loss and reduced body temperature determine humane endpoints in a mouse model of ocular herpesvirus infection. *J Am Assoc Lab Anim Sci 52*, 277-285.

Hoffmann, C. J., Harms, U., Rex, A. et al. (2015). Vascular signal transducer and activator of transcription-3 promotes angiogenesis and neuroplasticity long-term after stroke. *Circulation 131*, 1772-1782. doi:10.1161/circulationaha.114.013003

Huet, O., Ramsey, D., Miljavec, S. et al. (2013). Ensuring animal welfare while meeting scientific aims using a murine pneumonia model of septic shock. *Shock 39*, 488-494. doi:10.1097/shk.0b013e3182939831

Hunter, J. E., Butterworth, J., Perkins, N. D. et al. (2014). Using body temperature, food and water consumption as biomarkers of disease progression in mice with Eμ-myc lymphoma. *Br J Cancer 110*, 928-934. doi:10.1038/bjc.2013.818

Husmann, K., Arlt, M. J. E., Jirkof, P. et al. (2015). Primary tumour growth in an orthotopic osteosarcoma mouse model is not influenced by analgesic treatment with buprenorphine and meloxicam. *Lab Anim 49*, 284-293. doi:10.1177/0023677215570989

Kabra, M., Robie, A. A., Rivera-Alba, M. et al. (2013). JAABA: Interactive machine learning for automatic annotation of animal behavior. *Nat Methods 10*, 64-67. doi:10.1038/nmeth.2281

Kilkenny, C., Browne, W. J., Cuthill, I. C. et al. (2010). Improving bioscience research reporting: The ARRIVE guidelines for reporting animal research. *PLoS Biol 8*, e1000412. doi:10.1371/journal.pbio.1000412

Koch, A., Gulani, J., King, G. et al. (2016). Establishment of early endpoints in mouse total-body irradiation model. *PLoS One 11*, e0161079. doi:10.1371/journal.pone.0161079

Koch, S., Mueller, S., Foddis, M. et al. (2017). Atlas registration for edema-corrected MRI lesion volume in mouse stroke models. *J Cereb Blood Flow Metab 39*, 313-323. doi:10.1177/0271678x17726635

Kort, W. J., Hekking-Weijma, J. M., Tenkate, M. T. et al. (1998). A microchip implant system as a method to determine body temperature of terminally ill rats and mice. *Lab Anim 32*, 260-269. doi:10.1258/002367798780559329

Krarup, A., Chattopadhyay, P., Bhattacharjee, A. K. et al. (1999). Evaluation of surrogate markers of impending death in the galactosamine-sensitized murine model of bacterial endotoxemia. *Comp Med 49*, 545-550.

Kurz, A. (2008). Physiology of thermoregulation. *Best Pract Res Clin Anaesthesiol 22*, 627-644. doi:10.1016/j.bpa.2008.06.004

Leon, L. R., DuBose, D. A. and Mason, C. W. (2005). Heat stress induces a biphasic thermoregulatory response in mice. *Am J Physiol Regul Integr Comp Physiol 288*, R197-R204. doi:10.1152/ajpregu.00046.2004

Louie, A., Liu, W., Liu, Q.-F. et al. (1997). Predictive value of several signs of infection as surrogate markers for mortality in a neutropenic guinea pig model of Pseudomonas aeruginosa sepsis. *Lab Anim Sci 47*, 617-623.

Mei, J., Riedel, N., Grittner, U. et al. (2018). Body temperature measurement in mice during acute illness: Implantable temperature transponder versus surface infrared thermometry. *Sci Rep 8*, 3526. doi:10.1038/s41598-018-22020-6

Miller, A., Burson, H., Söling, A. and Roughan, J. (2016). Welfare assessment following heterotopic or orthotopic inoculation of bladder cancer in C57BL/6 mice. *PLoS One 11*, e0158390. doi:10.1371/journal.pone.0158390

Miller, D. S., Kok, T. and Li, P. (2013). The virus inoculum volume influences outcome of influenza A infection in mice. *Lab Anim 47*, 74-77. doi:10.1258/la.2012.011157

Molins, C. R., Delorey, M. J., Young, J. W. et al. (2012). Use of temperature for standardizing the progression of Francisella tularensis in mice. *PLoS One 7*, e45310.

Morton, D. B. (2000). A systematic approach for establishing humane endpoints. *ILAR J 41*, 80-86. doi:10.1093/ilar.41.2.80

Nemzek, J. A., Xiao, H. Y., Minard, A. E. et al. (2004). Humane endpoints in shock research. *Shock 21*, 17-25. doi:10.1097/01.shk.0000101667.49265.fd

Nunamaker, E. A., Anderson, R. J., Artwohl, J. E. et al. (2013a). Predictive observation-based endpoint criteria for mice receiving total body irradiation. *Comp Med 63*, 313-322.

Nunamaker, E. A., Artwohl, J. E., Anderson, R. and Fortman, J. D. (2013b). Endpoint refinement for total body irradiation of C57BL/6 mice. *Comp Med 63*, 22-28.

OECD (2000). Guidance Document on the Recognition, Assessment, and Use of Clinical Signs as Humane Endpoints for

Experimental Animals Used in Safety Evaluation. *Series on Testing and Assessment No. 19*. OECD Publishing, Paris. doi: 10.1787/9789264078376-en

Passman, A. M., Strauss, R. P., McSpadden, S. B. et al. (2015). A modified choline-deficient, ethionine-supplemented diet reduces morbidity and retains a liver progenitor cell response in mice. *Dis Model Mech 8*, 1635-1641. doi:10.1242/dmm.022020

Paster, E. V., Villines, K. A. and Hickman, D. L. (2009). Endpoints for mouse abdominal tumor models: Refinement of current criteria. *Comp Med 59*, 234-241.

Pedregosa, F., Varoquaux, G., Gramfort, A. et al. (2011). Scikit-learn: Machine learning in python. *J Mach Learn Res 12*, 2825-2830. doi:10.1002/9781119557500.ch5

Ray, M. A., Johnston, N. A., Verhulst, S. et al. (2010). Identification of markers for imminent death in mice used in longevity and aging research. *J Am Assoc Lab Anim Sci 49*, 282-288.

Sanchez-Alavez, M., Alboni, S. and Conti, B. (2011). Sex-and age-specific differences in core body temperature of C57BL/6 mice. *Age 33*, 89-99. doi:10.1007/s11357-010-9164-6

Sand, C. A., Starr, A., Nandi, M. and Grant, A. D. (2015). Blockade or deletion of transient receptor potential vanilloid 4 (TRPV4) is not protective in a murine model of sepsis. *F1000Res 4*, 93. doi:10.12688/f1000research.6298.1

Skarnes, W. C., Rosen, B., West, A. P. et al. (2011). A conditional knockout resource for the genome-wide study of mouse gene function. *Nature 474*, 337-342. doi:10.1038/nature10163

Slezak, M., Göritz, C., Niemiec, A. et al. (2007). Transgenic mice for conditional gene manipulation in astroglial cells. *Glia 55*, 1565-1576. doi:10.1002/glia.20570

Solomon, J. A., Tarnopolsky, M. A. and Hamadeh, M. J. (2011). One universal common endpoint in mouse models of amyotrophic lateral sclerosis. *PLoS One 6*, e20582. doi:10.1371/journal.pone.0020582

Stoica, L., Todeasa, S. H., Cabrera, G. T. et al. (2016). Adeno-associated virus-delivered artificial microRNA extends survival and delays paralysis in an amyotrophic lateral sclerosis mouse model. *Ann Neurol 79*, 687-700. doi:10.1002/ana.24618

Takayama-Ito, M., Lim, C. K., Nakamichi, K. et al. (2017). Reduction of animal suffering in rabies vaccine potency testing by introduction of humane endpoints. *Biologicals 46*, 38-45. doi:10.1016/j.biologicals.2016.12.007

Trammell, R. A. and Toth, L. A. (2011). Markers for predicting death as an outcome for mice used in infectious disease research. *Comp Med 61*, 492-498.

Vianna, D. M. and Carrive, P. (2005). Changes in cutaneous and body temperature during and after conditioned fear to context in the rat. *Eur J Neurosci 21*, 2505-2512. doi:10.1111/j.1460-9568.2005.04073.x

Vlach, K. D., Boles, J. W. and Stiles, B. G. (2000). Telemetric evaluation of body temperature and physical activity as predictors of mortality in a murine model of staphylococcal enterotoxic shock. *Comp Med 50*, 160-166.

Warn, P. A., Brampton, M. W., Sharp, A. et al. (2003). Infrared body temperature measurement of mice as an early predictor of death in experimental fungal infections. *Lab Anim 37*, 126-131. doi:10.1258/00236770360563769

Weismann, C. M., Ferreira, J., Keeler, A. M. et al. (2015). Systemic AAV9 gene transfer in adult GM1 gangliosidosis mice reduces lysosomal storage in CNS and extends lifespan. *Hum Mol Genet 24*, 4353-4364. doi:10.1093/hmg/ddv168

Wright, A. J. and Phillpotts, R. J. (1998). Humane endpoints are an objective measure of morbidity in Venezuelan encephalomyelitis virus infection of mice. *Arch Virol 143*, 1155-1162. doi:10.1007/s007050050363

Yamaguchi, S., Naoki, H., Ikeda, M. et al. (2018). Identification of animal behavioral strategies by inverse reinforcement learning. *PLoS Comput Biol 14*, e1006122. doi:10.1371/journal.pcbi.1006122

Conflict of interest

The authors declare that they have no conflicts of interest.

Acknowledgements

This work was supported by Berlin-Brandenburg School for Regenerative Therapies, Theracur Foundation, German Research Foundation (grant numbers: HO 5177/3-1, HA 5741/5-1, EM 252/2-1), German Federal Ministry of Education and Research, Berlin Institute of Health and Einstein Stiftung Berlin (grant number: 2014-223). Dr Hoffmann is a participant in the BIH Charité Clinician Scientist Program funded by the Charité – Universitätsmedizin Berlin and the Berlin Institute of Health.

Curriculum Vitae

Mein Lebenslauf wird aus datenschutzrechtlichen Gründen in der elektronischen Version meiner Arbeit nicht veröffentlicht.

Publication list

Original research articles

Year	Publication	Impact Factor (2020)
2022	**Kuffner MTC**, Koch SP, Kirchner M, Mueller S, Lips J, An J, Mertins P, Harms C, Dirnagl U, Endres M, Boehm-Sturm P, Hoffmann CJ. Paracrine Interleukin 6 induces cerebral remodeling at early stages after unilateral common carotid artery occlusion in mice, *Frontiers in Cardiovascular Medicine*, 2022	6.05
2022	Hoffmann CJ, **Kuffner MTC,** Lips J, Lorenz S, Endres M, Harms C. Zfp580 Regulates Paracrine and Endocrine Igf1 and Igfbp3 Differently in the Brain and Blood After a Murine Stroke. *Frontiers in Physiology* 2022;13 doi: 10.3389/fphys.2022.887180	4.57
2019	Kronenberg G, Gertz K, Uhlemann R, **Kuffner MTC**, Kirste I, An J, Jadavji NM, Schott BH, Scheffel T, Endres M, Hellweg R, Harms C. Reduced Hippocampal Neurogenesis in Mice Deficient in Apoptosis Repressor with Caspase Recruitment Domain (ARC). *Neuroscience.* 2019 Sep 15;416:20-29. doi: 10.1016/j.neuroscience.2019.07.032.	3.59
2020	Malik AR, Lips J, Gorniak-Walas M, Broekaart DWM, Asaro A, **Kuffner MTC**, Hoffmann CJ, Kikhia M, Dopatka M, Boehm-Sturm P, Mueller S, Dirnagl U, Aronica E, Harms C, Willnow TE. SorCS2 facilitates release of endostatin from astrocytes and controls post-stroke angiogenesis. *Glia*. 2020 Jun;68(6):1304-1316. doi: 10.1002/glia.23778.	7.45
2019	Mei J, Banneke S, Lips J, **Kuffner MTC**, Hoffmann CJ, Dirnagl U, Endres M, Harms C, Emmrich JV. Refining humane endpoints in mouse models of disease by systematic review and machine learning-based endpoint definition. *ALTEX*. 2019;36(4):555-571. doi: 10.14573/altex.1812231.	6.43

Conference presentations

Year	Conference presentation	Place
2019	**Kuffner MTC**, Hoffmann CJ, Lips J, Harms C (2019). IL-6 as a driving force of post-stroke regeneration. BSRT Symposium 2018 (poster)	Berlin, Deutschland
2019	**Kuffner MTC**, Hoffmann CJ., Lips J, Kirchner M, Koch SP, Foddis M, Mueller S, Endres M, Dirnagl U, Harms C (2019). Paracrine IL-6 as a driving force of post-stroke regeneration. BRAIN/PET conference 2019 (talk)	Yokohama, Japan

Acknowledgments

This thesis was made possible by the support of many people.

Firstly, I want to thank my advisor, Prof. Christoph Harms, for his expert advice, guidance, support, and scientific enthusiasm during the PhD and the possibility of becoming an independent researcher.

I would also like to thank Ulrich Dirnagl for providing the research environment and inspiration for improving and critically questioning research.

I am grateful to Christian Hoffmann for the determination and the unshakable belief in this project, the advice, and continuous support.

I want to express my gratitude to my colleagues. A big thank you to Janet Lips for teaching me how to handle mice without getting bitten, the early and late hours with behavioral studies, and the help with all those small and big things. To Dr. Gisela Lättig-Tünnemann, Dr. Magdalena Jochner, Dr. Mariana Cerdeira, Moritz Eggers, Philipp Hirsch, and all other past and present members of the AG Harms: Thank you for your inspiration, support, and fun times in the office.

I would also like to acknowledge the great work of Philipp Böhm-Sturm, Monika Dopatka, Marco Foddis, Paul Koch, Lara Mosch, and Susanne Müller.

I am thankful for the financial support from the Berlin-Brandenburg School for Regenerative Therapies and Sabine Bartosch for the excellent organization.

Finally, I want to thank my family and friends. George Kotsaris, Lorenz Gerbeth, and Dr. Ana García-Durán: thank you for making this journey together. My deepest gratitude goes to Dr. Jonas Traub, Maivi, and Lijan for their support and all the time I could invest in this thesis. Without you, this would have been so much harder. To Sabine Kuffner, Bernhard Kuffner, and Roland Schnittka: thank you for being there and giving me the chance to get this far.